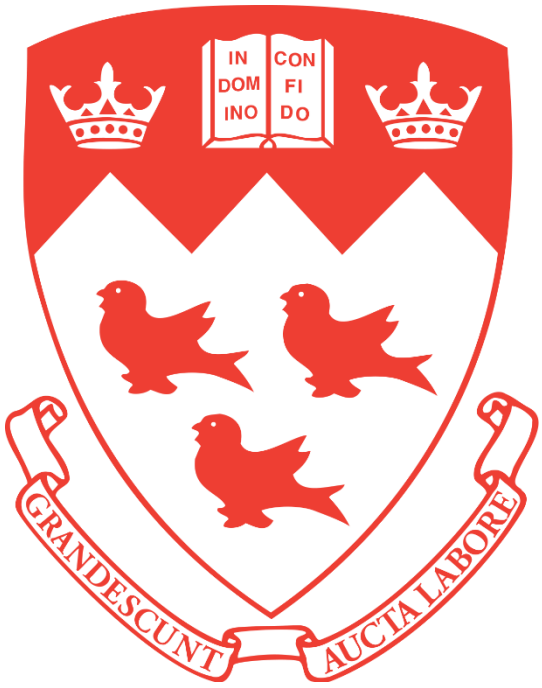

Injection Molding with Laser-Micromachined Molds to Fabricate Biomimetic Flow Enhancing Polymer Parts

Breno Mumic Sequeira
Department of Chemical Engineering
McGill University, Montreal, Quebec
July 2021

A thesis submitted to McGill University in partial fulfillment of the requirements of the degree of Master of Engineering

I. ABSTRACT

Self-emptying, non-stick polymer containers are sought after to decrease food waste and avoid additional handling. In this study, we attempt to develop an injection molding procedure that results in superhydrophobic, self-emptying containers. The phenomenon of superhydrophobicity can be attributed to the functionality imparted by microstructures on the surface, which are often superimposed by nanostructures. So, on a stainless steel mold, femtosecond laser micromachining is applied to create hierarchical micro/nanostructures with the inverse of the desired pattern for both polypropylene (PP) and high density polyethylene (PE). The optimum laser settings to create well-shaped structures of square and hexagonal geometry with different dimensions, spacings and depths have been determined. Further, we evaluated the resulting polymer samples in terms of polymer flowability and shape definition, both in industrial injection molding and in a laboratory hot press. We have demonstrated that hot press experiments can be adjusted to reliably represent injection molding. We have figured out that for the current lasing settings, the minimum width and spacing between features that can be laser-micromachined is 50 μm in order to maintain the intended shape of the geometries. The injection molding results show an aspect ratio limitation of 1.8, and that the most faithful replication are from pillared structures on the mold translating into holes on the polymer, PP, and larger structures. Square and hexagonal geometry have similar replication. Finally, a computational model is developed to predict which variables – width, spacing between features, and depth – for the abovementioned geometries, provide the best results in terms of superhydrophobicity for PE while considering the laser and injection molding constraints.

II. RÉSUMÉ

Les récipients en polymère antiadhésifs et à vidage automatique sont recherchés pour réduire les déchets alimentaires et éviter les manipulations supplémentaires. Dans cette étude, nous tentons de développer une procédure de moulage par injection qui permet d'obtenir des récipients superhydrophobes et à vidage automatique. Le phénomène de super-hydrophobie peut être attribué à la fonctionnalité conférée par les microstructures de la surface, sur lesquelles se superposent souvent des nanostructures. Ainsi, sur un moule en acier inoxydable, le micro-usinage par laser femtoseconde est utilisé sur le polypropylène (PP) et le polyéthylène à densité dure (PE), avec l'inverse du motif souhaité, pour créer des micro/nanostructures hiérarchiques. Les réglages optimaux du laser ont été déterminés afin de créer des structures bien définies de géométrie carrée et hexagonale avec différentes dimensions, espacements et profondeurs. En outre, nous avons évalué les échantillons de polymère obtenus en termes de fluidité et de définition de la forme, à la fois pour le moulage par injection industriel, et pour la presse à chaud en laboratoire. Nous avons démontré que les expériences de presse à chaud peuvent être ajustées pour simuler de manière fiable le moulage par injection. Nous avons déterminé qu'avec les réglages actuels du laser, la largeur et l'espacement entre les fonctions micro-usinées doivent être à un minimum de 50 µm afin de maintenir l'intégrité de la géométrie prévue. Les résultats du moulage par injection montrent une limitation du rapport d'aspect à 1,8. De plus, la réplication la plus fidèle provient de structures en piliers sur le moule se traduisant par des trous sur le polymère, le PP, et des structures plus grandes. Les géométries carrées et hexagonales présentent une réplication similaire. Enfin, un modèle est développé pour prédire quelles variables - largeur, espacement entre les fonctions, et profondeur -fournissent les meilleurs résultats en termes de super-hydrophobie pour les géométries susmentionnées et pour le PE, tout en considérant les contraintes du laser et du moulage par injection.

III. ACKNOWLEDGMENT

First of all, I would like to thank God for everything. As a catholic, I believe that God has always been supporting me, giving me strength, resilience, and constant guidance throughout my whole life. “Your word is a lamp to my feet and a light to my path.” Psalm 119:105.

Second, I would like to express my genuine gratitude to my amazing supervisor Prof. Anne-Marie Kietzig, for her endless support and for believing in me to take over this project. She has been my mentor for almost two years so far and I am deeply pleasured and grateful for all the time she has put into guiding, challenging, and providing me an unforgettable and pleasant experience, which I am honored to continue during my Ph.D.

Third, I would like to acknowledge my parents, who have supported me financially and emotionally throughout all of my master's studies. Also, my girlfriend, who has been the most loyal and supportive during this time. Even though we live apart, our love always shines through.

Fourth, I would like to thank all the great people in the Biomimetic Surface Engineering Lab. They have been so kind in supporting me, always with insightful discussions, and dedicating their precious time to help me in my project. Among all my amazing lab mates, a special thanks goes to Dr. Damon Aboud. He has been co-mentoring me since day 1, and I could say with confidence that because of him that I could manage to have so many results and interesting discussions in this project in such short amount of time.

Finally, I would like to acknowledge McGill University, more specifically the Faculty of Engineering. This institution has provided me an enormous number of opportunities, and I am extremely proud to be part of such selective number of students that study here.

IV. TABLE OF CONTENTS

V. LIST OF FIGURES

VI. LIST OF TABLES

1 INTRODUCTION

A problem in the use of food and waste packaging is the final emptying of these containers. In 2015, approximately 381 million tonnes of polymers were produced. Of this amount, only 9% were recycled, 12% incinerated, and 79%, which corresponds to 300 million tonnes of polymers, ended up in landfills (Geyer et al. 2017). This number of polymers in landfills contributes immensely to global warming and pollution. The reason why there are so many polymers being rejected in the recycling plants is due to the food waste in them. On average, about 25% of the polymers is too contaminated to go anywhere but the landfill (Semuels 2019). Also, food decomposition emissions are a major contributor to global warming, acidification, and eutrophication (Al-Rumaihi et al. 2020). Of similar importance, during garbage collection, trucks usually shake the trash cans to empty them, and that often causes their breaking. In San Diego, U.S., nearly 17,500 broken bins were replaced by their residents in 2018, costing more than US$1 million (Trageser 2019). Non-stick, self-emptying containers could address these problems.

The primary principle behind self-cleaning surfaces is a high liquid-solid contact angle, which can be attained either chemically or physically. The ones found in nature are mostly based on the physical approach, while the actual surface chemistry is trivial (Herminghaus 2000). For example, in the case of a lotus leaf, the surface features microscale bumps, which are superimposed on nanoscale hairy structures (hierarchical structures). This enables superhydrophobicity (e.g., extreme water repellence with contact angles > 150° and sliding angles < 5°) (Barthlott and Neinhuis 1997). Water drops sit on a composite surface made of air and solid, lowering the fraction of solid-liquid, and consequently resulting in very low adhesion. Rather than wetting the surface, water drops roll off the surface carrying dirt particles with them, resulting in a clean appearance of the leaf. These properties of wetting are known as Cassie wetting, in contrast to Wenzel wetting, where there are no air pockets beneath the liquid interface, but all surface valleys are filled with liquid. Wenzel can also result in contact angles > 150°, however the large solid-liquid contact areas result in high adhesion and thus high sliding angles (Cassie 1948; Wenzel 1936).

Femtosecond laser micromachining is an emerging technology that enables discrete shapes and functional surfaces to be made in a single step on diverse surface materials (Ahmmed et al. 2014). Such laser-structured surfaces are well suited for hot embossing and injection molding, which are standard methods used in the polymer industry (Groenendijk

2008; Yao et al. 2011; Gong et al. 2015; Toosi et al. 2016). Due to the contactless nature of laser micromachining, this process can be easily scaled up to the industrial level. Prof. Kietzig's Biomimetic Surface Engineering Laboratory group has acquired expertise over the past years in the fabrication of complex laser-inscribed surface features that yield hierarchical structures (Ling et al. 2016; Ahmmed and Kietzig 2016; Karthikeyan et al. 2018). The rough hierarchical structures on the laser-micromachined mold can be transferred as a mirror version to the polymer after the molding process, contributing to the lotus-like wetting behavior. Wetting tests are carried out by measuring the static contact angle and the contact angle hysteresis through a goniometer to assess the degree of hydrophobicity of the sample (Kietzig 2011). This research is intended to determine and optimize the patterns as well as injection molding conditions that would allow the transfer of all the hierarchical structures to the polymer, considering all possible constraints along the process.

This project runs in a collaboration between IPL Inc. and Prof. Kietzig's Biomimetic Surface Engineering Laboratory at McGill University. As the North America leader in manufacturing injection-molded polymer containers, IPL Inc. targets two major industrial sectors, food packaging, and waste containers. Both types of containers are susceptible to problems with content sticking to container walls, such as food waste and bad odors arising due to fouling. As a consequence, these containers require extra handling for emptying and cleaning, which also results in broken containers due to more aggressive emptying processes. IPL Inc. aims to revolutionize conventional packaging solutions through the creation of an economical method that makes polymer containers easy to flow and self-emptying, securing a competitive advantage over its competitors.

2 BACKGROUND

This chapter is a background of the state of femtosecond laser micromachining, wetting science, and the injection molding process. Fundamental principles and techniques are shortly discussed about these topics.

2.1 Femtosecond Laser Micromachining

Femtosecond laser micromachining is a precise machining process of high resolution, which has gained substantial attention over the past couple of decades (Ahmmed et al. 2014). The basic principle of a laser is to stimulate an atom's emission using light (Anisimov et al. 2008; Anisimov et al. 1974). Recent research on femtosecond laser micromachining has focused on functionalizing a surface of various materials with structures of different geometries and dimensions. By doing that, different properties of the material can be altered, such as electrical, mechanical, chemical, tribological, wetting, and optical. Each field requires a different type of surface structure to suit its application (Ahmmed et al. 2014).

The main principles behind laser micromachining are discussed in the following sub-chapters. Since the only material being laser-micromachined in this project is stainless steel P20, more emphasis will be given to the ablation of metals, other than other materials.

2.1.1 Laser-Matter Interaction and Ablation Threshold

In a laser beam, photons from coherent light excite electrons at the material's surface. If the energy delivered by the laser beam is high enough, a plasma plume is produced, and that material is removed in a process called ablation, in which ultimately hierarchical structures are formed (Sugioka and Cheng 2014). Laser ablation is affected by the material properties, the laser properties, and the machining environment. The ablation mechanism and experimental parameters influence the final surface modification. In particular, the threshold value for ablation is a crucial parameter for micromachining (Ahmmed et al. 2014).

Absorption of photons by electrons is the first step of laser-matter interactions. Ablation relies on both the amount of energy delivered to the substrate and its transfer to the lattice

away from the surface. As pulses last for femtoseconds, the electrons achieve much higher temperatures than the lattice. Then, the cooling of hot electrons is caused by hot electron diffusion and electron-phonon interaction. The lattice and electrons are thus able to reach thermal equilibrium. In general, the two-temperature model is used to explain the temperature dynamics before the electrons and the lattice reach thermal equilibrium (Anisimov et al. 1974; Chichkov et al. 1996). Thermal process is the name attributed to ablation that occurs after a few picoseconds. However, a non-thermal process is the laser material interaction that happens before this time, which is the case of femtosecond lasers (Von der Linde et al. 1997).

Femtosecond lasers guarantees advantages over other longer pulsed lasers (e.g., nano- or picosecond lasers) because of its shorter pulse duration (as short as 100 fs). As a consequence, high pressures and temperatures are produced in depths of the order of microns. Heat transferred by pulsed lasers rapidly heats the material, resulting in a direct transition to the vapour phase with high kinetic energy without passing through the melting point temperature due to the absorption of energy. As a result, the ablated area is more precise and smoother, and with less heat affected zone (HAZ) than what is typically observed with longer pulsed lasers (Nolte et al. 1997; Liu et al. 1997). In other words, less energy is needed to be delivered per unit area, designated as laser beam's fluence. The ablation threshold is conveyed in terms of peak fluence. It refers to the amount of energy per unit area that a surface experiences following a Gaussian profile and can be defined as (Mannion et al. 2004; Kruger and Kautek 2004):

$$F_0 = \frac{8P}{\pi f_p {\omega_0}^2} \tag{1}$$

where P is the average power of the laser beam measured through a power meter (W), f_p is the repetition rate of the laser (Hz) and ω_0 is the theoretical beam diameter (cm), that can be calculated by the following equation (Will et al. 2002; Noh et al. 2010):

$$\omega_0 = \frac{4l\lambda M^2}{\pi d} \tag{1}$$

where l is the focal length of the focusing length (cm), λ is the wavelength of the laser (cm), M^2 is the beam propagation factor (that represent the difference between a real laser

beam and an ideal diffraction-limited Gaussian beam), and d is the input/collimated laser beam diameter onto the focusing lens (cm).

A threshold fluence (F_{th}), or ablation threshold, is the amount of fluence caused by a certain pulse duration and fixed number of pulses that is enough for ablating a material (Nolte, et al. 1997). According to the following equation, the ablation threshold $F_{th}(N)$ for N pulses can be related to the single pulse ablation threshold $F_{th}(1)$, which is based on the accumulation model of Jee et al. (1998):

$$F_{th}(N) = F_{th}(1)N^{S-1} \tag{2}$$

where S is the incubation coefficient that determines the level of incubation in the material. Pulse accumulation, also known as incubation effect, is an extensively studied phenomenon in metals and other materials (Mannion et al. 2004; Rosenfeld et al. 1999; Semaltianos et al. 2009).

There are different methods for determining an ablation threshold. For its accuracy, diameter measurements are usually used. Micromachining parameters, such as pulse duration and wavelength, also affect the threshold fluence. However, below 100 picosecond pulses, there is no impact of pulse duration on the threshold fluence anymore (Gamaly et al. 2002). Furthermore, the metal sample thickness is a critical factor. For metal samples with thickness thinner than the hot electron diffusion length (*Lc*), the threshold fluence is increased. If they are larger than *Lc*, threshold fluence does not fluctuate with thickness anymore, and the fluence achieves its saturation (Wellershoff et al. 1999; Stuart et al. 1996; Gudde et al. 1998).

2.1.2 Area of Ablation and Accumulated Fluence

A pulsed laser emits energy in successive pulses, which are overlapping if a beam or sample is moving with a sufficiently low velocity, as it can be seen in Figure 1a. The change in horizontal pulse position is termed Δx (mm). Similarly, Δy is the change in vertical pulse position in raster scanning (mm). The equations are displayed below (Ahmmed et al. 2015).

$$\Delta x = \frac{v}{f_p} \tag{3}$$

$$\Delta y = (1 - \varphi_{line})\omega_{eff} \tag{4}$$

where v is the laser scanning velocity (mm/s), ω_{eff} is the experimentally obtained beam diameter of the effective beam diameter (mm), and φ_{line} is the line overlap, which can be calculated by the following (Ahmmed et al. 2014):

$$\varphi_{line} = \left(1 - \frac{\Delta z}{\omega_{eff}}\right) \times 100 \tag{5}$$

where Δz is the distance between the center of two overlapping lines (mm).

Using these three equations above, the number of pulses per spot (PPS) can be calculated by (Ahmmed et al. 2015):

$$PPS = \frac{\omega_0}{\Delta x}\frac{\omega_0}{\Delta y} \tag{6}$$

The surface ablated by a pulsed laser generates mainly two types of structures, laser-irradiated structures, and laser-inscribed structures. The laser-irradiated structures are the ones that are smaller than the laser beam itself, and only a few types of structures are reported. On the other hand, the laser-inscribed structures, the features are equal or larger than the beam diameter (ω_0), and the patterns are usually in a geometric shape, with virtually endless possibilities (Ahmmed et al. 2014).

As seen in Figure 1b, the laser-irradiated structures result from the ablation of the material's surface by a laser beam raster scanning successive lines. The size and shape of the features produced by successive pulses is directly related to the overall energy delivered to the material. Based on an irradiation model developed by Eichstädt et al. (2013), the total fluence distribution over a reference area was calculated by summing individual Gaussian pulses displaced by Δx and Δz. Equation 8 gives the fluence distribution of each individual Gaussian pulse (Eichstädt et al. 2013; Ahmmed et al. 2015).

$$F_p(x, y, z) = \left(\frac{8P}{\pi f_p {\omega_0}^2}\right) exp\left(-\frac{8(x^2 + z^2)}{{\omega_0}^2}\right) \tag{7}$$

Successive pulses in the multiple horizontal displacements of Δx are summed, resulting in the pulse's accumulated fluence of the ablated line, $F\sum pulse$. Whereas overlapping the

pulse-accumulated fluence in Δz displacement leads to the line-accumulated fluence, $F\sum line$, of a pattern (Ahmmed et al. 2014).

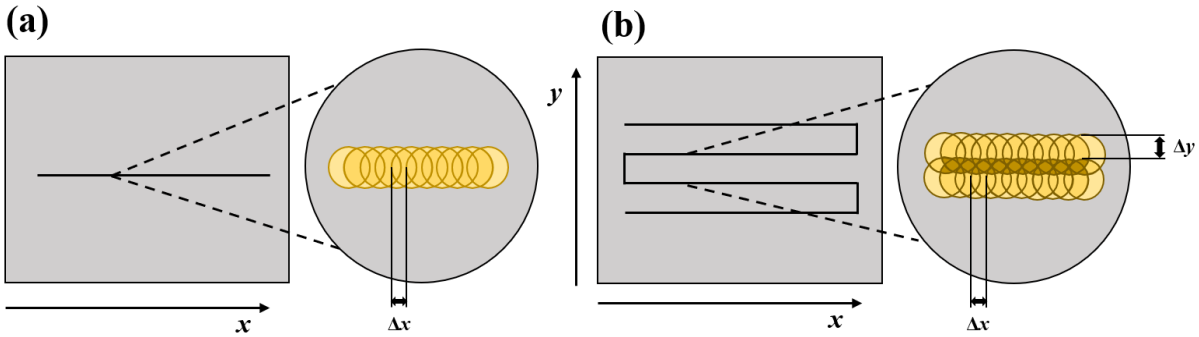

Figure 1. A series of successive pulses overlapping to form (a) a line, and (b) a pattern by raster scanning of a surface.

2.1.3 Laser Parameters

Laser micromachining employs a wide range of parameters, that can be divided into four main categories: (1) laser beam parameters, (2) sample parameters, (3) scanning parameters, and (4) processing parameters. Among the laser beam parameters are the average power of the laser beam, the pulse energy, the pulse duration, the repetition rate, the wavelength, and polarization of the light, as well as the collimated beam diameter. Sample parameters include the sample material and roughness. The scan velocity, scanner/stage distance from the focusing lens, angle of incidence, overlap, and the number of overscans are considered the scanning parameters. Lastly, the processing parameters that are taken into account are the micromachining environment, gas pressure, sample temperature, and sample mobility (stationary or mobile) (Ahmmed et al. 2014).

2.2 Surface Wetting

In its most general sense, wettability means a surface's ability to adhere to a liquid. The degree to which a liquid wets a surface is determined from the balance of cohesive and adhesive forces. In other words, if increasing the surface area of the liquid is more energetically advantageous than remaining in a sphere, then the solid will be at least minimally wetted (Shafrin and Zisman 1960). The wetting properties of a surface can be

significantly improved either by fabricating roughness on it (physical method), which is the case when using a femtosecond laser to micromachine the surface or by adding hydrophobic coatings to rough surfaces (chemical method) (Zhang et al. 2010).

Surfaces with small contact angle values (< 90º) are considered hydrophilic, e.g., high liquid-solid adhesion. Hydrophobic surfaces are the ones of which the contact angle values are between 90º and 150º, and the so-called superhydrophobic surfaces present a very high contact angle value (< 150º), with very low liquid-solid adhesion (Law 2014). In the following sub-chapters, different wettability models are discussed in detail.

2.2.1 Young's Model

Thomas Young made some important assumptions in 1805 when he determined the force balance at the three-phase, liquid/solid, liquid/air, and solid/air, contact line. First, an ideal surface was considered, with a pristinely smooth, chemically homogenous solid in contact with the liquid. This implies that the three-phase contact line does not become "pinned" but moves with the bulk water droplet on the surface. Second, in equilibrium, the force on the lines is stationary regardless of any infinitesimal shift in the orientation of the line (Young 1805). The result is that even while a "core area" is present in the vicinity of the three-phase contact line, it is feasible to calculate the contact angle by a force balance on the "far-field" surface energies independently, as shown in Figure 2 (de Gennes 1985). Equation 9 depicts Young's equation, which represents this force balance (Young 1805).

$$cos\theta_Y = \frac{\gamma_{sa} - \gamma_{sl}}{\gamma_{la}} \tag{8}$$

where γ_{sa}, γ_{sl} and γ_{la} are the surface tensions of the solid-air, solid-liquid, and liquid-air interfaces (N/µm), respectively, and θ_Y is the Young's contact angle.

Since ideal surfaces do not exist, measuring the Young's contact angle is not feasible. However, since establishing the value for this constant experimentally is necessary for wetting calculations, a flat surface is considered as ideal. In addition, real surfaces are neither perfectly smooth, nor homogeneous. In other words, each solid-liquid interaction may cause localized surface energies that differ based on the surface configuration of a specific area. As a result, the contact angle will vary depending on where the contact lines are located on the

surface (Wenzel 1936). The next sub-chapter describes Wenzel and Cassie-Baxter models, modified versions of Young's theory that take the surface roughness into account.

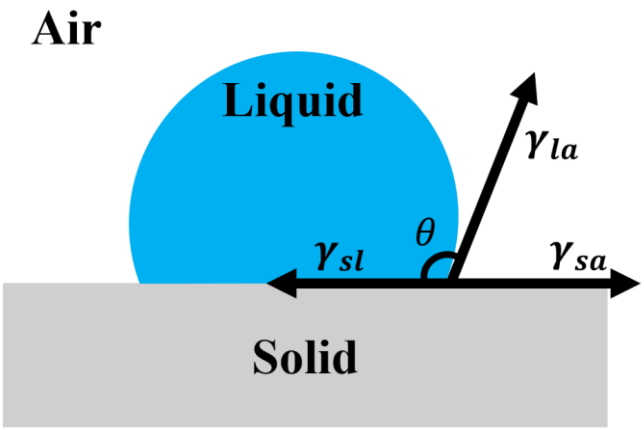

Figure 2. Contact angle at a three-phase (solid-liquid-air) contact line.

2.2.2 Wenzel (Homogeneous) and Cassie-Baxter (Heterogeneous) Models

Wenzel extended Young's relation to a roughened, chemically homogeneous surface with a roughness factor, *r*. The roughness factor is defined as the ratio of actual to apparent surface area. Wenzel's model describes the apparent contact angle (APCA) θ_w of a liquid drop on a rough surface, and the Young's contact angle of the same liquid deposited on a flat surface with identical chemical composition. During the Wenzel state, the liquid penetrates completely into the rough surface, causing only a solid-liquid interaction, as Figure 3a shows. The Wenzel apparent contact angle is calculated by Equation 10 (Wenzel 1936).

$$cos\theta_w = r\, cos\theta_Y \tag{9}$$

where *r* is defined by:

$$r = \frac{actual\ rough\ surface}{projected\ geometic\ surface} = \frac{real\ surface}{superficial\ surface} \tag{10}$$

An ideal surface results when r = 1 (Young's equation). So, when a real surface is considered, the roughness factor will always be > 1. Increasing the roughness of a surface

will increase its hydrophobicity or hydrophilicity, as the contact angle increases or decreases, respectively. Note that the equality in Equation 10 is not sustained if the roughness factor is large, or in other words if the surface is very rough.

Cassie and Baxter were the first to describe the heterogeneous wetting state for rough surfaces. In their model the surface is composed of *n* different materials, each with their respective material fraction f_i. Each material has its own surface tension value, and when summed represents the value of the entire system. Consequently, the Cassie-Baxter contact angle (θ_C) can be calculated by the following (Cassie and Baxter 1944):

$$r cos\theta_C = \sum_i^n f_i \left(\frac{\gamma_{i,sa} - \gamma_{i,sl}}{\gamma_{la}}\right) = \sum_i^n f_i cos\theta_{i,Y} \tag{11}$$

In 1964, Johnson and Dettre proposed that liquid can act differently from the Wenzel wetting state by resting on air pockets instead of impinging on rough surfaces. Thus, there is a reduction in the contact area between the solid and the liquid, as can be seen in Figure 3b. Applying this concept into the Cassie-Baxter two-component (solid-air) heterogeneous case, $f_1 = f_{sl}$ and $cos\theta_{1,Y} = cos\theta_Y$ for the solid-liquid fraction. For the liquid-air fraction, $f_2 = f_{la}$ and $cos\theta_{2,Y} = -1$, because it is completely dry. Therefore, Equation 12 plus roughness factor, *r*, can be reformulated as (Johnson and Dettre 1964):

$$cos\theta_C = f_{sl}(r\, cos\theta_Y + 1) - 1 \tag{12}$$

where $f_{sl} = A/A_C$. A is the interfacial area (μm²) and A_C the cell apparent area, or unit area (μm²).

Note that for $f_{sl} = 1$, the Equation 12 reduces to Wenzel's Equation 10, and that the lower f_{sl} value is, i.e., lower solid-liquid contact, the higher the θ_{CB} will be.

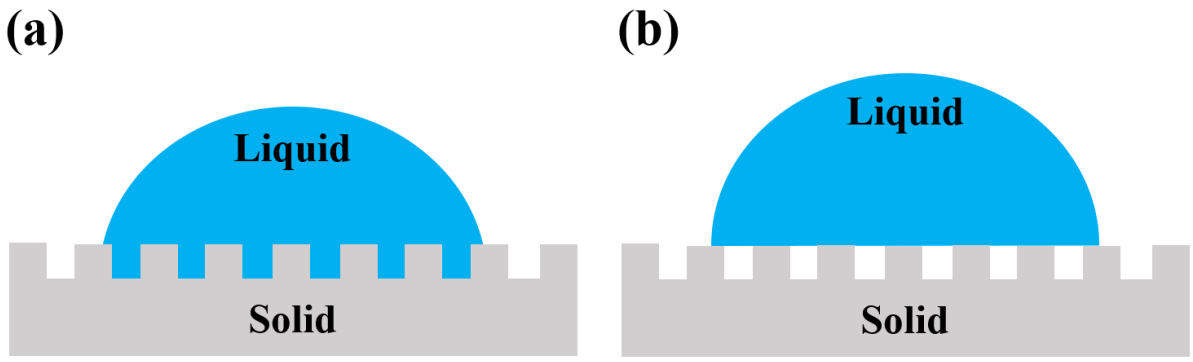

Figure 3. (a) Wenzel (homogeneous), and (b) Cassie-Baxter (heterogeneous) wetting states.

Understanding the fundamental differences between Wenzel's and Cassie-Baxter's superhydrophobicity is of paramount importance. In order to be considered superhydrophobic, the surface needs to satisfy two conditions: (1) present a θ > 150º, and (2) a contact angle hysteresis (CAH) < 5º. The contact angle hysteresis is defined as (Nosonovsky and Bhushan 2009):

$$CAH = \theta_{adv} - \theta_{rec} \tag{13}$$

where θ_{adv} is the advancing contact angle and θ_{rec} is the receding contact angle, with θ_{adv} > θ_{rec}.

Static contact angles > 150º can be achieved in both Wenzel and Cassie-Baxter wetting states. However, only through the Cassie-Baxter wetting state superhydrophobicity can be reached, since the CAH needs to be < 5º. In Wenzel's state, the CAH is much higher, since the water droplets are stuck into the cavities, not allowing them to easily roll off the surface. The well-known examples in nature are the lotus-leaf (Cassie-Baxter) and the rose petal (Wenzel) (Lin Feng 2008).

Leaf surfaces of superhydrophobic and self-cleaning plants are known to possess inherent hierarchical structures, which lead to very low solid-liquid contact areas and air pocket formation for water droplets of various sizes (Kock et al. 2008). The largest solid-liquid contact area is found on flat surfaces, that decreases when the surface presents microstructures, followed by nanostructured surfaces and is minimized in hierarchically structured surface (Bhushan 2019), as shown in Figure 4.

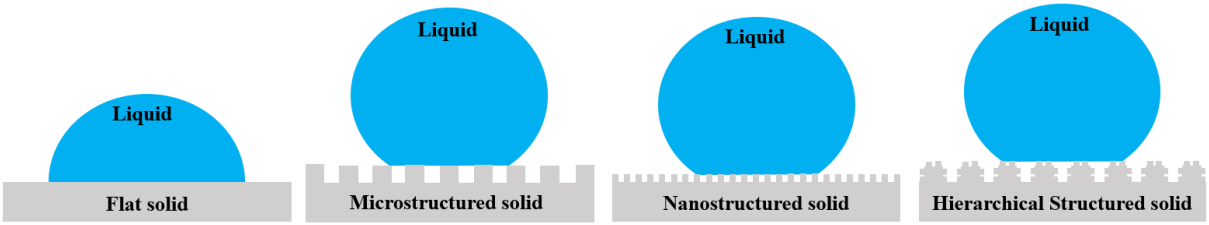

Figure 4. Schematic illustration of the wetting of four distinct surfaces: flat, microstructured, nanostructured, and hierarchical structured solids.

2.2.3 Prediction of the Predominance of Heterogeneous Wetting State Based on Thermodynamics and Kinetics Optimization

In literature, the energy and pressure concepts are being used to describe wetting phenomena on solid surfaces. Both allow for the estimation of the wetting transition barrier. However, while the energy concept essentially requires numerical models, the pressure concept commonly allows for analytical access in cases of solid surfaces with complex shaped geometries.

The relevance of wetting, in the context of this project, relates firstly to the desired outcome of the high density polyethylene (PE) and polypropylene (PP) melt to penetrate the stainless steel P20 mold (SS) features (Wenzel wetting) during injection molding and at the same time, the ability of the water beading off the polymer parts (Cassie-Baxter wetting). In other words, we are aiming for the transition between a Wenzel wetting state in terms of the polymer completely penetrating the steel mold, to a Cassie-Baxter wetting state in terms of the superhydrophobic behavior of water on the surface of the polymer after the transfer of the hierarchical structures from the metal mold to the polymer. Experimentally, if the mold has square pillars micromachined for example, square holes will be transferred to the polymer and vice versa. Figure 5 illustrates the difference between pillar and hole types of structures. In addition to it, as our goal is to create a superhydrophobic PE and PP, not only we want a Cassie-Baxter state to prevail in the H_2O on PE/PP scenario, but we also desire a Cassie-Baxter contact angle > 150^o with low hysteresis or a low roll off angle.

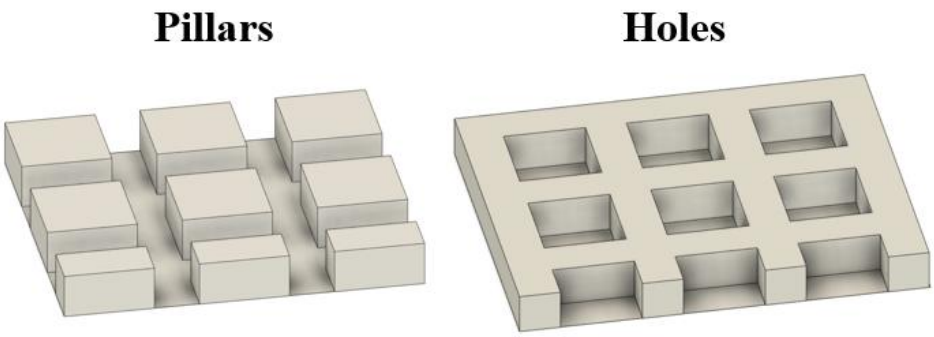

Figure 5. Illustration of the difference between pillar and hole types of structures.

2.2.3.1 Energy concept

The energy concept predicts the existence of heterogeneous wetting states on rough surfaces. The free enthalpy (Gibbs energy) of the three-phase system is analyzed for minima in the energy function that correspond to possible heterogeneous (Cassie-Baxter) or homogeneous (Wenzel) wetting states on a certain rough surface. Calculations of the global minimum in Gibbs energy predicts which of these two states is energetically favorable for a given system, depending on the surface geometry, topography, and local wettability. Furthermore, understanding the first principles of thermodynamics and kinetics will allow for optimization of dimensions of surface structures to achieve superhydrophobicity (Hensel et al. 2013). Generally, Gibbs free energy of a solid (s) - liquid (l) - air (a) wetting system is given as Equation 15:

$$G = \gamma_{la} A_{la} + \gamma_{sl} A_{sl} + \gamma_{sa} A_{sa} \tag{14}$$

Apart from the Cassie-Baxter and Wenzel wetting states, a third wetting state (Cassie-Baxter Metastable) is possible where the liquid partially penetrates the surface roughness (Patankar 2004). This partial penetration, depth (*h)*, can take various values corresponding to distinct geometrical interfaces and therefore results in different APCA as introduced in Figure 6 (Sarkar and Kietzig 2013).

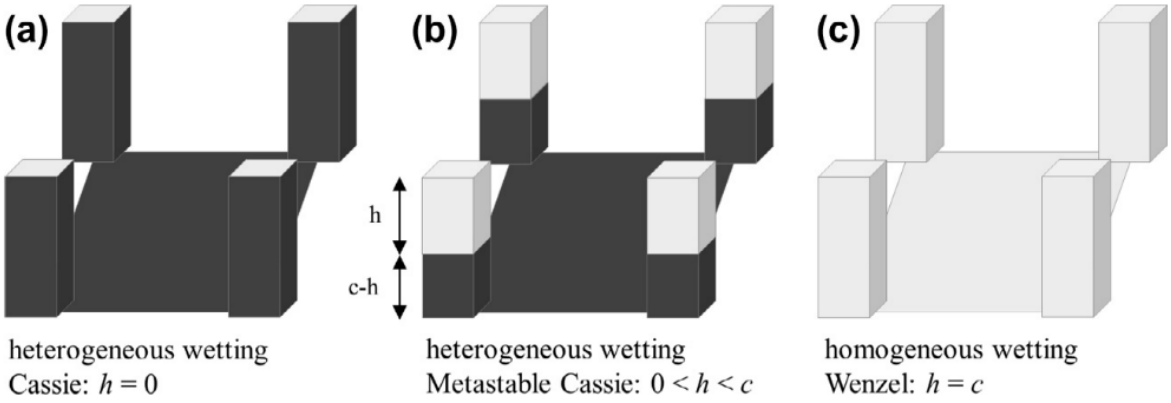

Figure 6. Penetration depth *h* of different wetting states indicating wetted (dark) and dry (bright) pattern surfaces. (a) Heterogeneous wetting: Cassie: $h = 0$; (b) heterogeneous wetting: metastable Cassie: $0 < h < c$; (c) homogeneous wetting Wenzel $h = c$ (Sarkar and Kietzig 2013).

Rearranging Young's equation (Equation 9), substituting it into the Gibbs free energy Equation 15, and using the relation that $\Delta A_{sl} = -\Delta A_{sa}$ we obtain a simplified equation:

$$\Delta G^{unit} = \gamma_{la}(\Delta A_{la} - \Delta A_{sl} cos\theta_y) \tag{15}$$

The unit areas were calculated for the square and hexagon geometries, both in pillar and hole types, considering the solid-air, solid-liquid, and liquid-air interfaces before the droplet is on the surface, during full wetting (Wenzel) and during partial wetting of the surface (Cassie-Baxter) (Sarkar and Kietzig 2013). Then, they were substituted into Equation 16, for both the Cassie-Baxter (G_{cassie}) and Wenzel (G_{wenzel}) wetting states to calculate $\Delta G_{max} = G_{wenzel} - G_{cassie}$. Maximizing the difference between G_{wenzel} and G_{cassie} (ΔG_{max}) renders the energy barrier between the two states harder to overcome, and the lower the energy of Cassie-Baxter state is, the more stable this wetting state will be.

2.2.3.2 Pressure concept

The pressure concept is an analytical determination of the wetting resistance, that is, the robustness of the heterogeneous wetting state. The penetration of an expanding fluid into the micro- and nanoscale grooves of rough surfaces is considered, until the homogeneous wetting state is achieved (Hensel et al. 2013).

The water-air interfacial tension $\gamma_{la} = 0.0728$ N/m can cause an inner pressure of $p = \frac{4\gamma_{la}}{d} = 235$ Pa for a spherical water droplet with 10^{-3} ml and diameter of d = 1.24 mm. Smaller droplets induce larger pressures (Zheng et al 2005). Raindrops can even cause pressures as high as 10^4-10^5 Pa on earth (Erpul et al 2002).

The critical or maximum hydraulic pressure for various pillar cross sections can be calculated using Equation 17, which is a unified, analytical, and precise formula. This equation assumes that the hydraulic pressure is homogeneous and that the microscale structures are much smaller than the water droplet diameter (~1 mm). Using such assumptions, we can study the effects of hydraulic pressure on only a cell for any periodic interpillar water-air interface. This model system is advantageous because the corresponding results are independent of the water droplet diameter (Zheng et al 2005).

$$\mathrm{P}_c = \frac{\gamma_{la} f_{sl} cos\theta_y}{(1 - f_{sl})\lambda} \tag{16}$$

where λ is a given pillar slenderness ratio (μm), and can be calculated by:

$$\lambda = \frac{A}{L} \tag{17}$$

in which L is the perimeter (μm).

It is worth noticing that the lower the solid-liquid fraction is, the lower the critical hydraulic pressure. That means that the higher the contact angle is, the lower the critical hydraulic pressure that the structures can handle before being completely wet, and the Wenzel state prevails. So, the geometrical dimensions must be selected in a way that the superhydrophobicity can be achieved, while holding the maximum hydraulic pressure possible.

3 REVIEW OF LITERATURE - MICRO-NANOSTRUCTURED MOLD FABRICATION WITH POSTERIOR REPLICATION ON POLYMERS THROUGH MOLDING

Molding of various polymers from micro-nanostructured metal molds have been investigated extensively for the creation of superhydrophobic polymer parts, because of their enhanced self-cleaning, anti-reflective and anti-fouling properties. Table 1 provides a summary of the most relevant studies, detailing the used techniques for machining and molding, and also the associated settings, materials, and relevant findings.

According to Table 1, the most used methods to create hierarchical structures on metal molds are machining with a micro-working robot, lithography, etching, electrical discharge machining (EDM), and laser micromachining. Among these methods, laser micromachining offers significant advantages for its reproducibility, high precision and controllability, minimum heat-affected zone, one-step, contactless, operation in standard ambient conditions, also being considered a green and inexpensive technique (Vorobyev and Guo 2013). This process allows the ablation of various geometries (e.g., squares, cylinders, and hexagons) and types (pillars and holes) in the microscopic scale. It also allows the fabrication of laser-induced periodic surface structures (LIPSS), that are a surface relief composed of (quasi-) periodic lines, and/or ripples, which are nanostructures formed spontaneously under laser irradiation (Fadeeva et al. 2011).

Effective molding methods that imprint the inverse of the hierarchical structures from the mold, for a variety of polymers and mass-production, are needed. The most used ones are injection molding and hot embossing, as it can be seen in Table 1. However, for industrial fabrication of polymers, injection molding is the main process used (Heckele et al. 1998). Stainless steel is the dominant material investigated for the mold, along with PP as the polymer.

Only a few authors have reported the achievement of superhydrophobic polymers through injection molding (Saarikoski et al. 2011; Guan et al. 2013; Guan et al. 2015). However, they have utilized additional techniques to improve the final polymer superhydrophobicity, such as UV/O_3 treatment post-injection molding and dip-coating of the mold insert with an ultrasonically dispersed solution of hydrophobic silica particles and ethanol. Without additional techniques, to the best of my knowledge, no authors have reported superhydrophobic polymer parts after injection molding yet. That is mainly due to

the difficulty in replicating nanostructures on top of microstructures, and the relatively low aspect ratio (< 2) penetration of the polymers in the mold during injection molding.

Some recent studies have focused on replicating only LIPSS on different polymers (Orazi et al. 2020; Piccolo et al. 2020; Lutey et al. 2021). They have successfully achieved that, however when the mold has also the presence of microstructures, the replication of LIPSS is compromised, as Wu et al. (2011) has previously found. One technique that has been investigated to overcome that is the use of a mold with higher temperature, helping the polymers to penetrate deeper into the structures (Rasilainen et al. 2010; Saarikoski et al. 2011; Vepsäläinen et al. 2012; Guan et al. 2013; Hong et al. 2015; Weng et al. 2017; Zhou et al. 2017; Romano et al. 2019; Piccolo et al. 2020; Lutey et al. 2021). That is because when the mold is at room temperature, the polymer melt in the mold grooves cools down rapidly, due to heat transfer from the polymer to the mold, and that prevents the complete filling of hierarchical structures (Matschuk and Larsen 2013; Stormonth-Darling et al. 2014). On the other hand, whenever the polymer penetration of high aspect-ratio structures is achieved, a better control of the demolding process is needed to not break the polymer's hierarchical structures during demolding. For that, the most commonly used technique is the application of an anti-sticking coating layer on the mold insert (Cech and Taboryski 2012; Griffiths et al. 2013 Hobæk et al. 2015). The choice of the polymer and molding settings also play a vital role regarding the polymer flowability inside the hierarchical structures. Considering the choice of polymer only, it is expected that polymers of comparatively lower viscosity will result in a more faithful replica of the mold structures than polymers of higher viscosity, also achieving higher aspect ratio structures. With respect to mold settings, increasing molding temperature or injection pressure, can also lower the polymer's viscosity, which is beneficial as mentioned. However, settings the molding temperature too high will lead to polymer degradation. Thermal processing of industrial thermoplastic polymers is typically carried out between 130 and 380 ºC. Operating within the 530 and 730 ºC range, where viscosity is expected to be 10 to 1000 times lower, could easily minimize many technological and economic limits. However, it is not possible to process polymers at these temperatures because of most polymers' thermal instability at those temperatures. It is necessary to perform processing operations in temperature domains just below what is known as the thermal stability ceiling (TSC), where melt viscosities are fairly high (Colin and Verdu, 2006).

As mentioned by Groenendijk (2008), the most important parameters for hydrophobic structures are height of the structures and the spacing between them. Since, if correctly chosen CA values on PP of up to 165º with very low CAH can be achieved. However, all the

authors have chosen their particular dimensions without optimization in terms of maintaining the Cassie-Baxter wetting state. In terms of geometry types imprinted on the polymer, most of the authors mentioned in Table 1 have tested cylindrical pillars, since this is the geometry and type that is found on the well-known lotus-leaf. Other than that, Weng et al. (2017) has tested square pillars with superimposed cylindrical nanopillars, Xie et al. (2019) square pillars, and Romano et al. (2019) square and hexagonal holes. However, none have achieved superhydrophobicity, with the first failing in replicating AR > 2 on the polymer, the second presented a very high rolling angle of 79º, and the last CAH of 27º, due to the low AR replication achieved (0.1 – 0.9).

Table 1. Prominent research on micro-structured mold fabrication with posterior replication on polymers through molding.

Author	Type of geometry/structures imprinted on the polymer	Dimensions of geometries/structures	Machining method	Laser settings	Mold and Polymer	Molding method	Molding settings	Relevant findings
Groenendijk (2008)	Cylindrical Pillars and Holes	Width = ~10 µm Spacing between structures = ~10 µm AR = ~1	Laser micromachining	Pulse length = 200 fs Rep. Rate = 250 kHz	Steel and PP	Injection molding	Not mentioned	• It is possible to create superhydrophobic surfaces with the use of a femtosecond laser
Noh et al. (2010)	Cylindrical Pillars (lotus-leaf-like structures), and Square Holes	Diameter = 10 µm Nanostructures diameter = 200 nm	Laser micromachining	Pulse length = 12 ps Wavelength = 355 nm Rep. Rate = 640 kHz ω0 = 35 µm Fluence = 12.99 and 25.89 mJ/cm² Speed = 0.1 m/s	Steel and PDMS	Polymer casting	-	• Replicated polymer present CA = 157°, in agreement with Cassie-Baxter theory rather than with Wenzel's.
Rasilainen et al. (2010)	Cylindrical Pillars	**Microstructures** Diameter = 20-126 µm Spacing between structures = 10-50 µm AR = ~0.3-1.3 **Nanostructures** Diameter = 50-90 nm	Micro-working robot and anodization with subsequent application of an epoxy layer	-	Aluminum and PP	Injection molding	Injection pressure = 5 bar Screw rotational speed = 100 rpm Mold temperature = 50 °C Molding temperature = 230 °C	• The best result is the highest AR value (1.33), with CA = 149±7° and CAH = 11±8°
Yao et al. (2011)	LIPSS	Period = 600-700 nm AR = ~0.3	Laser micromachining	Pulse length = 120 fs Wavelength = 800 nm Rep. Rate = 1 kHz Power = 130 mW Speed = 2 mm/s	Steel and PC	Gas-assisted (Nitrogen) hot embossing	Molding temperature = 150-170 °C Holding pressure = 20-40 bar	• Optimized hot-embossing parameters for duplicating the mold structures = 30 bar and 170 °C • Gas-assisted hot embossing improve the uniformity transcription of PC with Steel
Wu et al. (2011)	LIPSS	Period = 600 nm-28.8 µm	Laser micromachining	Pulse length = 120 fs Wavelength = 800 nm Rep. Rate = 1 kHz Fluence = 0.5-4.0 J/cm² Speed = 0.286-2 mm/s	Steel and PP	Injection molding	Holding pressure = 491.3 bar (5.22 s) Cycle time = 30.86 s Cooling time = 10 s Molding temperature = 204 °C	• Top surface of the microstructures not covered with nanostructures on the polymer • Higher fluence and lower speed to machine the mold present the highest CA value on the polymer replica (133°)
Saarikoski et al. (2011)	Cylindrical Pillars	**Microstructures** Diameter = 19 µm Spacing between structures = 22 µm AR = 1.84 **Nanostructures** Diameter = 58-63 nm	Micro-working robot and anodization	-	Aluminum and TPE	Injection molding with subsequent UV treatment	Injection pressure = 5 bar Mold temperature = 80-140 °C Molding temperature = 190-240 °C	• Pillars height on the TPE is 1.34 times the depth of the holes on the mold. UV-cured coating has good stretching conditions for the formation of long pillars • Nanopores on the mold assist the formation of the nail-shaped micropillars, which result in CA = 164° and SA close to 0°
Vepsäläinen et al. (2012)	Cylindrical Pillars	Diameter = 20 µm Spacing between structures = 20-80 µm AR = 1.5	Micro-working robot	-	Aluminum and PP	Injection molding	Injection pressure = 5 bar Screw rotational speed = 80/100 rpm Mold temperature = 70 °C Molding temperature = 230 °C	• PP has similar spatial frequency and roughness features to the mold • Input data of a micro-working robot can be used to predict experimental dimensions of structures on the polymer

Guan et al. (2013)	Cylindrical Pillars with submicron and curved grooves	**Cylindrical Pillars** Diameter = 250 µm AR = 0.44 **Curved grooves** Width = 540 µm AR = 0.2	Punching and Laser micromachining	Not mentioned	Steel and PP	Injection molding with subsequent UV/O_3 treatment to improve hydrophobicity	Injection rate = 154 cm^3/s Compression force = 200 kN (17 s) Compression speed = 35 mm/s Cooling time = 15 s Mold temperature = 120 °C Molding temperature = 230 °C	• Superhydrophobicity is achieved on the curved grooves only, with CA values from 155 to 170°, with RA values from 4 to 6° • Low roughness (nanoscale) of the sidewalls of the micro pillars led to the increased RA values
Gong et al. (2015)	Cylindrical Pillars (lotus-leaf-like structures)	Diameter = 24 µm Spacing between structures = ~10 µm AR = 1.25	Laser micromachining	Pulse length = 10 ps Wavelength = 1064 nm Rep. Rate = 100 kHz $\omega 0$ = 24 µm Fluence = 6.63 J/cm^2	Steel and PTFE	Hot embossing	Holdig pressure = 550~850 bar Molding temperature = 130 °C Cycle time = 2-15 min	• Optimized hot-embossing parameters = 700 bar and 15 min of cycle time. CA = 155° and SL = 5.5° • Thermal stability of the superhydrophobic PTFE surfaces could be kept until 340 °C
Guan et al. (2015)	Curved grooves	Width = ~250 µm AR = ~0.3	Laser micromachining. Mold dip-coated with an ultrasonically dispersed solution of hydrophobic silica particles and ethanol.	Not mentioned	Steel and PP with embedded silica particles	Injection molding	Molding temperature = 230 °C Compreesion force = 110 kN (30 s) Cooling time = 150 s	• Higher mold temperature and force led to more faithful PP replicas in terms of height (micro and nanostructures) and consequently higher CA value (average 172°) with average SA value of 3° and self-cleaning efficiency of 52%, characterizing rice-leaf wetting behavior • Better mechanical robustness and self-cleaning efficiency are seen in replicas with rose petal wetting behavior
Hong et al. (2015)	Cylindrical Pillars	Diameter = 30 µm Spacing between structures = 100 µm AR = 0.47	Lithography	-	Nickel and PMMA	Injection molding	Injection speed = 140 mm/s Holding pressure = 500 bar (0.43 s) Cooling time = 25 s Mold temperature = 80 °C Molding temperature = 270 °C	• Thermal contact resistance (TCR) between the mold and the polymer melt increases with elapsed time during the injection stage, but decreases during packing stage • TCR increases along with mold tickness Obs.: High TCR means that the polymer will cool down before reach the bottom of the cavities
Choi et al. (2016)	Irregular structures	Surface Roughness (Ra) 0.01, 0.1, 0.4, 1.0, 2.0, 3.2 and 5.0 µm	Electrical Discharge Machining (EDM)	-	Steel and PMMA and COC	Injection molding	Not mentioned	• Complete replica of irregular structures on both polymers for all different surface roughness values • COC samples presents CA values between 85° and 95° (Ra = 5.0) and PMMA ranging between 65 and 73° (Ra = 3.2)
Toosi et al. (2016)	Irregular structures (paraboloidal, triple roughness and cauliflowered)	Width = 18-50 µm AR = 0.7-3	Laser micromachining	Pulse length = 140 fs Wavelength = 800 nm Rep. Rate = 1 kHz Fluence = 16-310 J/cm^2 Speed = 0.46-0.93 mm/s	Steel and HDPE, PLA, and PVC	Hot embossing with trichloro silane coating applied onto the imprinted PVC and HDPE to reduce the surface energy	Molding temperature = 140-180 °C Holding pressure = 30-120 bar (10 min) Cooling time = 30 min (10 °C)	• HDPE and PLA present CA > 160° and CAH < 5°. However the water repellency feature of PLA is higher than HDPE, due to its lower viscosity, and consequently more faithful imprint on the mold • PVC does not achieve superhydrophobicity • Cauliflowered structures (formed at higher fluence and medium speed) present higher CA when translated into all the polymers
Weng et al. (2017)	Square Pillars with superimposed cylindrical nano-pillars	Width = 30 µm Spacing between structures = 45 µm AR = 1, 2 and 3	Litography and reactive ion etching	-	Nickel and PP	Injection molding	Injection rate = 18 cm^3/s Holding pressure = 1200 bar (5 s) Cooling time = 60 s Mold temperature = 120 °C Molding temperature = 250 °C	• Micro-pillars completely replicated, while nanostructures were composed of lumpy and grainy nano-protrusions • AR of 2 and 3 do not present complete polymer replica. The best result (AR = 1) presents CA = 163° and sliding angle of 5° (CAH = 15°)

Zhou et al. (2017)	Cylindrical Pillars	**Microstructures** Diameter = 200 µm Pitch = 400 µm AR = 0.4 **Nanostructures** Diameter = 400 nm Pitch = 450 nm AR = 12	Etching and AAO (Anode Aluminum Oxide) template with anti-sticking layer (fluoroalkylsilane solution)	-	Steel and PP and PC	Injection molding	Injection rate = 18 cm³/s Holding pressure = 800 bar (5 s) Cooling time = 90 s Mold temperature = 163 and 178 °C for PC and 103 and 118 °C for PP Molding temperature = 20 °C higher than glass transition of the polymer	• Higher CA values are achieved for higher mold temperatures in both polymers. For PP, CA = 152° and for PC, 151° (SA = 19°)
Xie et al. (2019)	Square Pillars	Width = ~70 µm Spacing between structures = ~25 µm AR = ~1	Not mentioned	-	Steel and PP	Hot embossing	Molding temperature = 230 °C Compreesion force = 110 kN (30 s) Cooling time = 150 s	• CA = 155° and RA = 79°
Romano et al. (2019)	Square and Hexagonal Holes	Pitch = 2 - 80 µm AR = 0.1 - 0.9	Laser micromachining	Pulse length = 310 fs Wavelength = 1032 nm ω0 = 30 µm Power = 0.245-3.945 W Rep. Rate = 100-500 kHz Speed = 500-2000 mm/s	Steel and PP	Injection molding	Injection pressure = 400 bar Injection speed = 200 mm/s Holding pressure = 450 and 700 bar (5 s) Cycle time = 25 s Mold temperature = 60 and 80 °C Molding temperature = 230 °C	• All samples show Wenzel state and did not achieve superhydrophobicity. • The best result presents CA = 160° and CAH = 27°
Orazi et al. (2020)	LIPSS, parallel and transversal to the flow direction	Sa = 0.5 µm Width = ~70 nm AR = 0.3	Laser micromachining	Pulse length = 8 ps Wavelength = 1064 nm ω0 = 30 µm Power - 3.5 W Rep. Rate = 1000 kHz Speed = 2.5 m/s	Steel and PET	Injection molding	Injection speed = 200-600 mm/s Holding pressure = ~625-725 bar Mold temperature = 15 °C Molding temperature = 300 °C	• LIPSS parallel to flow induce strong wall slip of the polymer melt, alowing a reduction in the injection pressure of 10%
Piccolo et al. (2020)	LIPSS, parallel and orthogonal	Width = ~480-1780 nm AR = 0.15-0.57	Laser micromachining	Pulse length = 8 ps Wavelength = 1064 nm ω0 = 40 µm Rep. Rate = 1000 kHz Speed = 1500 mm/s Fluence = 174-197 mJ/cm²	Steel and PS and PMMA	Injection molding	Injection speed = 110 mm/s Holding pressure = 450 (PS) and 500 bar (PMMA) Cooling time = 10 s Mold temperature = 40-120 °C Molding temperature = 235 (PS) and 255 °C (PMMA)	• CA values increased 20% and 17% for PMMA and PS, respectively with LIPSS when compared to flat surfaces • Mold temperature at 60 and 70 °C are the optimized ones for PMMA. Further increase in it does not improve hydrophobicity, even with higher replication accuracy in terms of depth
Lutey et al. (2021)	DLIP - holes and pillars - and LIPSS, oriented in parallel and perpedicular to the injection direction	Prominent periodicity = 0.82-0.92 µm Height = 39-55 nm	Laser micromachining	Pulse length = 10 ps Wavelength = 1064 nm ω0 = 28 µm Rep. Rate = 100-1000 kHz Power = 0.8-2.9 W Speed = 0.1-2 m/s	Steel and PP	Injection molding	Injection rate = 50 cm³/s Injection pressure = 300 bar Holding pressure = 450 bar Mold temperature = 65 °C Molding temperature = 260 °C	• Best transfer effectiveness achieved for LIPSS oriented parallel, followed by perpendicular to the injection direction, then DLIP holes and finally DLIP pillars. In the first case, 97% of the height from the mold is achieved on the PP
Bouchard et al. (2021)	Cylindrical Pillars with DLIP	Weight = 30-70 µm Spacing between structures = 30 µm AR = ~0.01	Laser micromachining	Pulse length = 4 ns and 70 ps Wavelength = 1064 and 532 nm Rep. Rate = 30 and 10 kHz	Steel and PET	Hot embossing	Molding temperature = 85 °C (10 min) then 50 °C (5 min) Compreesion force = 200 kN (30 s) Final pressure applied = 416 bar	• Very accurate replica of the micro and nanostructures on PET in terms of height/depth • Superhydrophobicty not reached. CA increased from 77° (flat) to 105° (hierarchical structures) on PET

4 THESIS OBJECTIVES

The research hypothesis was that it is possible to design surface patterns that will result in robust superhydrophobicity on injection molded polymer parts while considering the requirements and constraints of the laser machining and molding processes. Therefore, the motivation for this project was to find the patterns and injection molding conditions that would allow proper transfer of all roughness levels to the polymer.

The following sub-objectives were addressed:

1. Creation and optimization of Python codes to ablate different geometries (square, rhombus, hexagon, cylinder and triangles) in both types, pillars and holes;
2. Determination of laser settings (focusing lens, scan line overlap, overscans, power and scanning velocity) for efficient fabrication of patterns with different dimensions, selecting the candidate dimensions for the injection molding phase.
3. For the injection molding test, the goals were:
   I. Test injection molding limitations regarding different:
      a) Geometries (square and hexagon);
      b) Types for each geometry (pillar and hole);
      c) Dimensions.
   II. Test different polymers (PP and PE) for all settings abovementioned and compare:
      a) Quality of polymer replication for different injection molding cycles;
      b) Nanostructure's transfer.
   III. Compare injection molding with hot press results.
4. Determination of hot press settings (molding temperature, holding pressure, time under heating and pressure, and time for cooling) for effective transfer of hierarchical structures from the mold to the polymer, so this technique could be used as a comparison with injection molding.
5. Creation of a computation model based on first principles from thermodynamics and kinetics to predict which dimensions, for square and hexagonal geometry, with the type (pillar or hole) that had the best results from the injection molding campaign, that lead to superhydrophobicity, also considering the maximum

hydraulic pressure that the structures could handle before being penetrated by water, while respecting the laser and injection molding constraints.

5 MATERIALS AND INSTRUMENTATION

In this chapter the materials and equipment utilized for laser micromachining, hot press experiments, contact angle measurements, confocal and SEM analysis along with supporting software for analysis are described.

5.1 Materials

The metal mold used for laser micromachining and posterior hot press/injection molding is made of stainless steel P20. This metal is the main steel utilized for injection molding in the polymer industry due to its inherent properties such as enhanced toughness and hardness, machinability, and comparatively good thermal conductivity (AZoM, 2012). To test different laser parameters and Python codes with the trajectories to fabricate different geometries, small rectangular sheets of steel were used, with dimensions varying from 2x1 cm^2 to 3x2 cm^2, with thickness of around 1 mm (Figure 7a). For molding experiments at McGill, stainless steel cylindrical stubs with diameter of 13.2 mm were used (Figure 7b and c). Both steel shapes were bought at McMaster-Carr and cut in the Wong machine shop at McGill. Prior to laser micromachining, the steel samples were initially polished using a 600 grid sandpaper with posterior 1200 grid, until a mirror-like polish was achieved. For the injection molding campaign, IPL Inc. provided us industrially polished stainless steel P20 samples of around 1.4x1.4 cm^2 to be directly laser-micromachined (Figure 7d and e). After polishing and/or laser micromachining, the steel samples were sonicated in an ultrasonic bath with acetone inside a fume hood for five minutes for cleaning and removing loosely attached nanoparticles that are generated during laser micromachining and redeposited on the structures. Eventually it was realized that this sonication procedure was not enough for the removal of all redeposition particles in the mold. They were mostly removed or pushed to the bottom of the cavities after several hot press experiments or injection molding cycles. This particular topic will be further discussed in the next chapters.

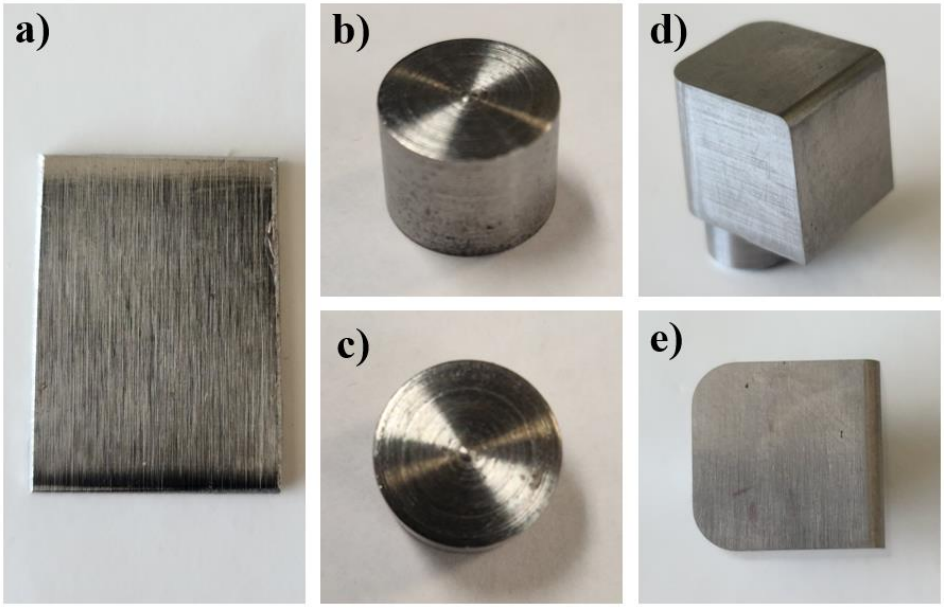

Figure 7. Schematic of the P20 stainless steel a) rectangular sheet before polishing, b) cylindrical stub before polishing diagonal view and c) top view, d) IPL steel sample diagonal view, and e) top view.

For the molding experiments at McGill, only PE resin was tested, while for injection molding at IPL Inc., PE, and PP were tested. For the molding experiments at McGill, IPL Inc. provided both polymers in a powder format. The PP has hardly been tested in the hot press due to time limitations mainly caused by COVID-19 pandemic restrictions experienced especially in 2020. PE (more specifically high density polyethylene 2074) is supplied to IPL Inc. by ExxonMobil Chemical, and PP (polypropylene copolymer 2071) by Total Petrochemicals. PE is one of the common polymers used for injection molding in the polymer industry due to its versatility, extreme strength, and moldability while being lightweight. PP is also widely used, due to its low viscosity, moldability, and resistance to a broad selection of bases and acids (ACME, 2019). Both polymers are used for the fabrication of food and waste containers. Their relevant properties for this thesis according to the abovementioned suppliers' data sheets are summarized in Table 2.

Table 2. Main resin properties of PE and PP.

	PE	**PP**
Density (g/cm^3)	0.948	0.905
Melt Flow (g/10 min)	5	50
Melting Temperature (°C)	130	160-165

Rheometry of both PE and PP was carried out at the *Laboratoire d'ingénierie des polymères et composites* at *L'École de technologie supérieure* (ÉTS), supervised by Prof. Nicole R. Demarquette. For that, a capillary rheometer (Instron SR20) was used. This type of rheometer was chosen because of the ability to closely replicate flow geometry and shear rate experienced by the polymer during injection molding. The experiments were carried out using conditions which are presented in Table 3.

Table 3. Experiment conditions for viscosity measurements.

Polymer	Temperature (^{0}C)	Capillary length (mm)	Capillary diameter (mm)
PE	220	10	1
		20	
PP	220	10	1
		20	

The data obtained was used to plot rheological curves, presented in Figure 8. From its analysis, it can be inferred that the PP viscosity is considerably lower than the one of PE across all tested shear rates. For example, for 50 s^{-1}, the apparent viscosity of PP is 3.32 times lower than the PE, and for 1000 s^{-1}, it is 4.61 times lower.

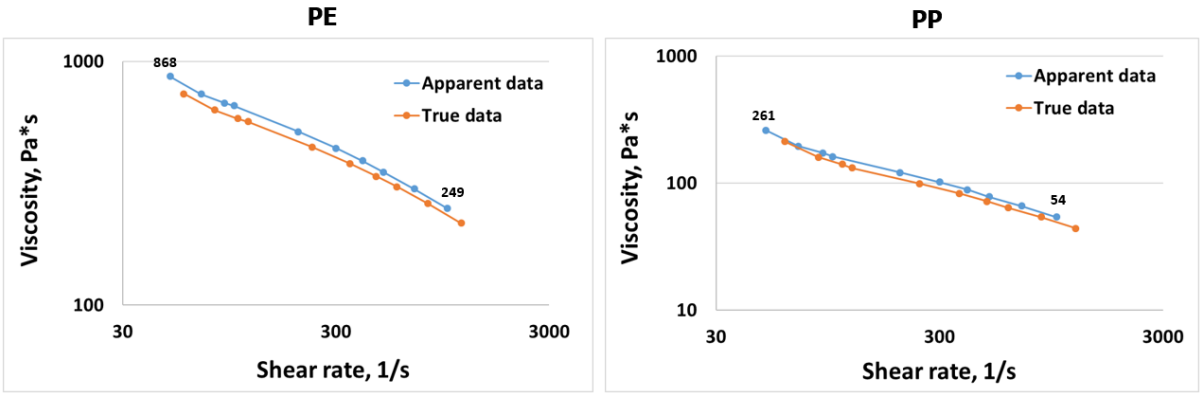

Figure 8. Rheological curves of PE and PP at 220 ºC.

To facilitate the demolding process after the hot press experiments, the lubricant WD-40 ® Specialist Silicone, bought at Canadian Tire, was utilized to act as a demolding agent. This lubricant was chosen mainly due to its effectiveness at temperatures ranging from -73 to 260 °C. In addition, according to the supplier, it is waterproof, protects metal and polymer surfaces, dries fast, and does not attach dirt particles. During molding experiments at McGill, WD-40 silicone lubricant was added gently on the cylindrical steel stubs, on their sides, and

in the donut hole of the mold where the stubs and polymer are placed. In the injection molding campaign at IPL, no demolding agent was applied.

5.2 Instrumentation

5.2.1 Laser Micromachining

The stainless steel P20 samples were all laser machined at the Biomimetic Surface Engineering Laboratory at McGill University. The laboratory houses of a solid state Ti:Sapphire femtosecond laser system (Coherent Libra) that delivers a Gaussian beam at a wavelength of 800 nm and in pulses of < 100 fs duration operated at a repetition rate of 1 kHz. A 4 W beam passes through a digitally controlled attenuator consisting of a half-wave plate and polarizing beam splitter to lower the pulse energy down to the desired value. It then passes through a digitally controlled mechanical shutter, before being focussed onto the sample of interest through a 25.4 mm bi-convex focusing lens to the desired spot size. The surface to be machined is placed on top of a 3D stage (Newport Corporation) whose trajectory of motion, as well as velocity, are computer software controlled. The experimental setup is displayed in Figure 9.

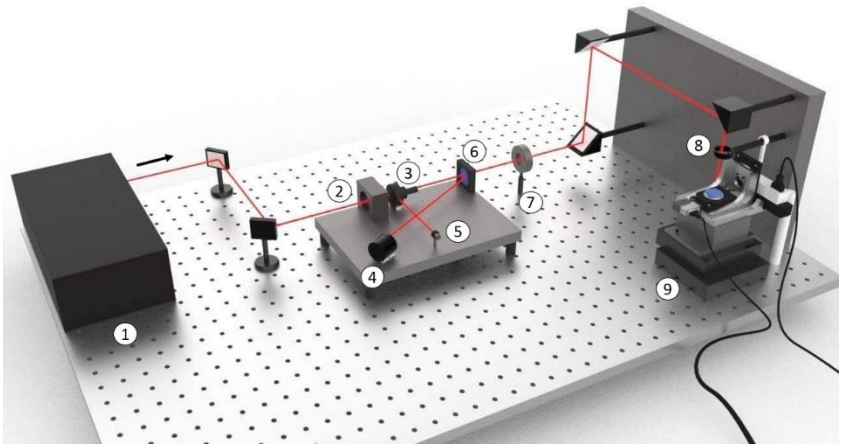

Figure 9. Experimental setup for femtosecond laser micromachining: 1) laser, 2) half-wave plate, 3) polarizing beam splitter, 4) power meter, 5) beam dump, 6) beam sampler, 7) mechanical shutter, 8) focusing lens, 9) 3D stage.

The 25.4 mm bi-convex lens was chosen according to equation 2, which shows that the theoretical beam diameter could be as small as 6 µm with around 6 pulses per spot when the scanning velocity is 1 mm/s. Theoretically this enables the fabrication of structures with

width and spacing between features as small as the theoretical beam diameter. As it will be shown and explained later in more details, according to the thermodynamic optimization, geometries will provide the highest degree of hydrophobicity if the width and spacing between features are as small as possible, with the highest possible depth/height.

5.2.2 Hot Press Molding

Following laser micromachining of the steel insert, molding experiments are conducted to transfer the negative of hierarchical structures in the steel samples to the PE resin. The molding experiments were conducted through a Carver vertical hydraulic hot press at the Biomimetic Surface Engineering Laboratory at McGill University. The variable parameters of the hot-pressing process allow for control over key variables including holding pressure, temperature of both plates used to compress the inserts, and time, both during holding pressure and for cooling, which allow this technique to be compared with injection molding.

After a hot press experiment is completed, the sample is demolded manually, by clamping the mold in a vise, and hammering the flat insert using a screw with a diameter smaller than the insert. This process is carefully carried out to not damage the inner hole of the mold, which could create leakage of polymer during pressing. As a side note, this process does not damage or interfere with the hierarchical structures of the final polymer replica.

5.2.3 Contact Angle Measurements

A contact angle goniometer is the equipment used to measure both the static contact angle and the contact angle hysteresis of surfaces. Prof. Kietzig's laboratory houses a home built goniometer, comprised of an *Infinity 3* microscope camera (Teledyne Lumenera, Inc.) equipped with a *VZM 200i* zoom imaging lens (Edmund Optics, Inc.). High backlighting is provided by an ultra-bright LED spotlight (Optikon Corp). A 70-2203 syringe pump module (Harvard Apparatus, Inc.), controlled by a custom Arduino code, pumps degassed reverse osmosis water onto the studied surface. The SCA 20 module is the base software module that allows the measurement of the static contact angles.

5.2.4 Confocal Microscopy

A confocal microscope (Olympus, LEXT OLS 5000) was used to create 3D elevation maps of the surface structures with a micrometer resolution. Confocal microscopy assists the measurement and comparison of the geometrical characteristics of the mold insert patterns and their polymer replicas, to ensure faithful polymer replica of the microstructures. The microscope is located in the Cellular Microenvironment Design Lab at McGill University from Prof. Christopher Moraes.

The confocal data was analyzed through a MATLAB code created by Dr. Damon Aboud at the Biomimetic Surface Engineering Laboratory. The code basically smoothes the data by removing noise, finds the maxima and minima of the structures and calculates the height/depth of the structures, and measure the full width at half maximum to calculate both the width and the spacing between the structures. Before using the MATLAB analysis code, an auto correction was applied in all data in the analysis confocal software.

The nomenclature for the dimensional parameters used throughout this thesis is as follows: for pillar structures *a* represents the feature width, *b* the spacing between features and *c* the height of the feature, while for hole structures *a* indicates the spacing between features, *b* the width of a single feature and *c* the depth.

5.2.5 Scanning Electron Microscopy (SEM)

A Scanning Electron Microscope (FEI Quanta 450 FE-ESEM) from the Facility for Electron Microscopy Research (FEMR) at McGill University was mostly utilized to check the nanostructures created by laser ablation on the mold and their expected replicas on the polymers. Through focusing a high-energy electron beam onto the surface of interest, a magnification of between 6 to 1,000,000x with a resolution up to 10 nm can be achieved. The interaction between the electron beam and the sample provides information on the surface morphology.

Prior to the SEM imaging, the polymer surfaces need to be coated with a conductive layer of metal to enable imaging. This layer inhibits charging, reduces thermal damage, and enhances the secondary electron signal required for topographical examination in the SEM (Höflinger, 2013). It is not required to coat the stainless steel inserts, since they are already

conductive. To coat the polymers, a platinum sputter coating technique was applied. For that, a Leica Microsystems EM ACE600 High Resolution Sputter Coater from FEMR at McGill University was utilized. The platinum coating layer had 5 nm thickness on the polymers.

6 DEVELOPMENT OF METHODOLOGY

In this chapter, the methodology applied for creation and optimization of Python codes for laser micromachining distinct geometries and types, optimization of laser parameters for the fabrication of well-defined geometries, optimization of hot press settings to achieve complete polymer replicas with the highest aspect ratio values, surface analysis through confocal microscopy, injection molding campaign, and contact angle measurements for the thermodynamic optimization are presented.

6.1 Creation and Optimization of Python Codes for Laser Micromachining

The 3D translation stage moving the sample under the stationary laser beam at the Biomimetic Surface Laboratory is controlled by an XPS-Q8 Controller. This XPS executes continuous multidimensional motion path in a three-dimensional XYZ space. The X and Y stages have a maximum acceleration of 300 mm/s² and the Z stage, 0.8 mm/s², and they are controlled through lines of commands in a .txt file. Each of them has nine different columns named, time (s), X position (mm), X velocity (mm/s), Y position (mm), Y velocity (mm/s), Z position (mm), Z velocity (mm/s), shutter position (mm) and shutter velocity (mm/s). As a side note, the shutter only serves to either expose the sample to the beam or to shield it. These .txt files can be written manually by inputting different commands. However, it is not viable to manually create lines of commands for each trajectory, since depending on its complexity, there could me more than 1,000,000 commands. So, in order to avoid that, the first stage of the project was the programming of Python codes to generate .txt files to micromachine different geometries, both in pillar and hole types. These codes have the goal to standardize the logics to create these different geometries mainly using “for loops”, which are control flow statements used for iterating over sequences. The codes are also adaptable for different laser parameters (scanning velocity, number of overscans, % of overlap, and beam width) and dimensions of the pattern and the structures (width and spacing between features) as desired.

One Python code was developed for each of the following geometries and types: square, rhombus, triangles, and hexagons, both in pillar and hole types, and one code for cylindrical holes. The cylindrical pillar code was not developed due to its complexity, and as it will be shown in the next sub-chapter, depending on the laser parameters chosen, the small

features ($a \leq 50$ µm) for square and hexagonal pillars laser micromachined on the mold actually resulted in cylindrical features caused by the Gaussian beam shape. Figure 10 illustrates the arrangements of the geometries coded for both pillars and holes. It is important to keep in mind that this figure is just for the sake of illustration of the arrangements, and that the dimensions of the geometries and the spacing between them can be altered as desired. These particular arrangements are being used to guarantee an equidistance between all the structures, maintaining the same value of spacing between features, therefore maintaining a stable Cassie-Baxter wetting state throughout the pattern.

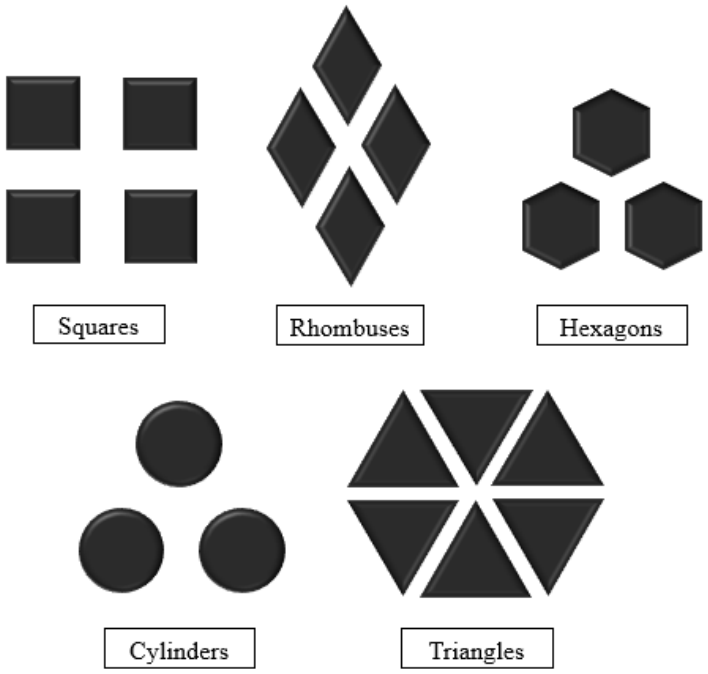

Figure 10. Illustration of the arrangements of the geometries coded for both pillars and holes.

The codes for square, hexagonal, and cylindrical holes, as well as hexagonal pillars already existed from previous studies in the Biomimetic Surface Engineering Laboratory. The other codes were developed in the context of this thesis. From all these nine codes, only square and hexagonal pillars and holes were fully tested, i.e., from their optimization for laser micromachining until the hot press and injection molding experiments. The other geometries will be fully tested and compared in terms of polymer flowability in the continuing collaboration with IPL Inc.

The first code developed by me was the one for square pillars. This first code was updated twice to achieve its final and optimized version. Figure 11 illustrates the 2D graphs generated by the commands given from the .txt file to the XPS from the first (Figure 11a),

second (Figure 11b), and final (Figure 11c) codes programmed for square pillars. The yellow lines represent the motion of the 3D stage when the shutter is closed especially during acceleration and deceleration, meaning that those areas were not ablated by the laser beam. The black areas represent the ones where the shutter is open, therefore the laser beam is ablating the surface. It is important to note that the dimensions of the structures, overlap, and laser parameters used to generate those graphs in Python are irrelevant for the moment, and that these graphs are being shown just for visualization of the trajectories in each of the codes developed. In addition, both *x* and *y*-axis of these graphs represent the length of the patterns in the *x* and *y* direction respectively, in *mm*. In the end, the shape of the structures on these graphs seems like rectangles rather than squares due to the scaling of the axis.

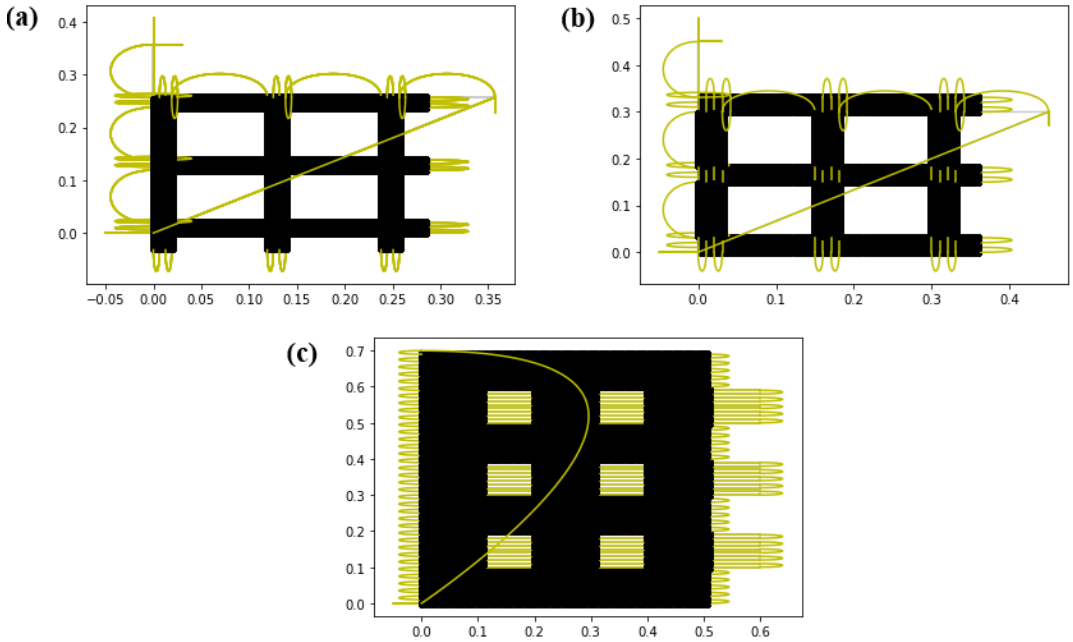

Figure 11. Illustration of the 2D graphs generated by the commands given from the .txt file to the XPS from the a) first, b) second and c) optimized codes programmed for square pillars.

The main problem with the first code (Figure 11a) is that the laser beam is ablating twice all the intersections. The laser starts ablating the horizontal lines (from left to right, then returning from right to left) and then the vertical lines (from top to bottom, then returning from bottom to top), crossing the same areas where the horizontal lines have already been ablated. That results in these intersections presenting higher depths than the rest of the pattern, which is undesirable. Therefore, this code was disregarded from the beginning without any single test in the laser. Then, an adaptation of this code was programmed to avoid the laser from ablating the intersections twice. As it can be seen in Figure 11b, for the

vertical lines, the shutter was now closing at the beginning where the horizontal lines were previously ablated, and reopening right after the end of them, avoiding it from ablating the intersections twice. However, one main problem was found with this approach. Since the Gaussian laser beam is not perfectly spherical, but slightly oval, the beam ablating horizontally always have a smaller diameter than the beam ablating vertically. In order to achieve square structures using this code, "band-aid" solutions were always necessary whenever the laser parameters or the dimensions of the squares changed. Figure 12 shows 2D heat maps with $a = b = 50$ µm square pillars with 1 overscan (Figure 12a) and 4 overscans (Figure 12b) using the second code tested. The laser parameters used to ablate these square pillars were 100 mW of power with 2 mm/s of scanning velocity. As it can be seen, fairly well-defined square structures were achieved, but due to its not adaptability for different dimensions of structures, this code was not further tested, and a new approach was tested. Well-defined structures are achieved when the bottom of the features laser micromachined on the mold have the shape of the desired geometry based on visual analysis of the heat maps from confocal microscopy. That is because when the pattern from the steel mold is replicated on the polymer, the bottom of the features from the pattern laser micromachined on the mold becomes the top of the features for the pattern on the polymer. As a consequence, the top of the features on the polymer is where the solid-liquid contact between the polymer and the water will occur. Therefore, well-defined structures are sought after so the thermodynamic optimization could be applied with more accuracy and these geometries can be compared in terms of polymer flowability into the cavities.

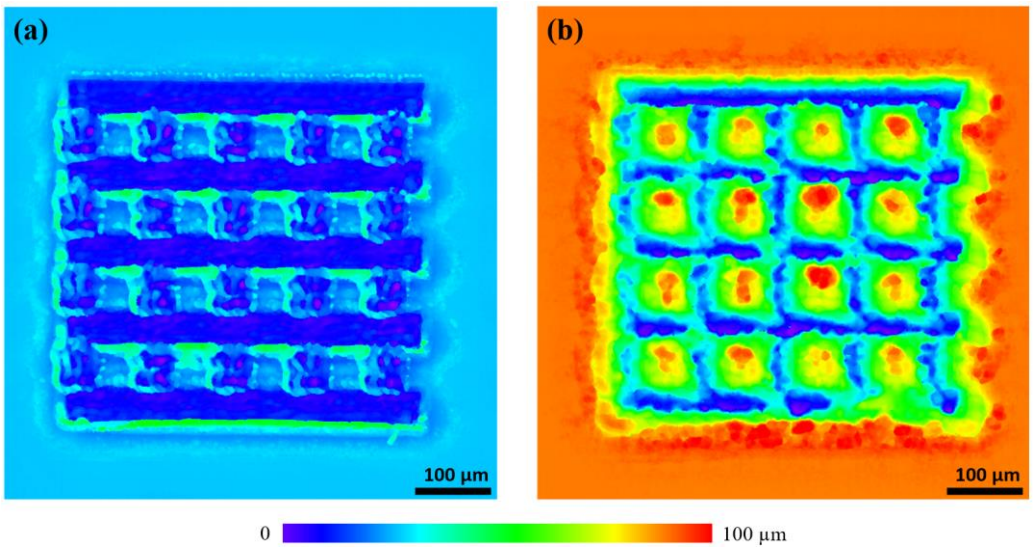

Figure 12. 2D heat maps from confocal microscopy for $a = b = 50$ µm square pillars with a) 1 overscan and b) 4 overscans from the second code tested.

Because of the problem with horizontal and vertical ablation with a Gaussian beam identified with the second code, a new code was developed (Figure 11c), but this time, ablating only horizontally to avoid the differences in beam width values. Figure 13 exhibits 2D heat maps from confocal microscopy for $a = b = 50$ µm square pillars with 1 overscan (Figure 13a) and 4 overscans (Figure 13b) using the optimized version of the code. The laser parameters used to ablate these square pillars were 100 mW of power with 2 mm/s of scanning velocity. As it can be noticed, not only fairly well-defined square pillars were achieved, but also this new code is adaptable for any dimensions wanted, without the need of "band aid" solutions.

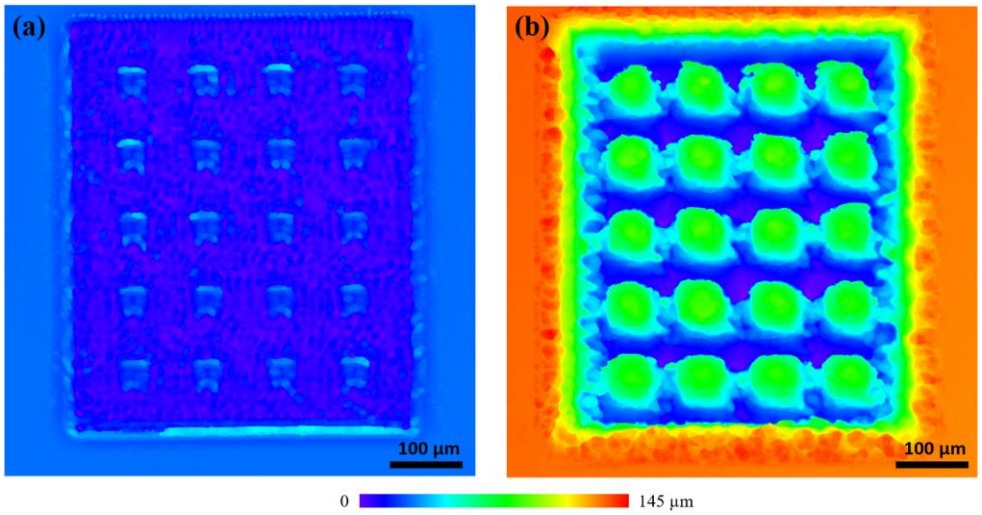

Figure 13. 2D heat maps from confocal microscopy for $a = b = 50$ µm square pillars with a) 1 overscan and b) 4 overscans from the optimized code tested.

At the time when the first code for square pillars was being created, the first code of rhombic pillars was also being programmed. The logic applied for square pillars was the same as the one applied for rhombic pillars in terms of trajectory design, and that is why the rhombic pillar code was also update twice (Figure 14a).

Hole structures were easier to design and program than pillar ones, because the laser beam does not need to ablate the contour of the geometries like for pillar structures but ablating inside the desired geometries decreases the complexity for the programming. As a consequence, the code for rhombic holes (Figure 14b) was easily adapted from the pre-existing square hole code. The last codes developed were the triangular pillars (Figure 14c) and holes (Figure 14d). Profiting from the knowledge acquired from the optimization of square and rhombic geometries, the triangular codes were quickly programmed, tested, and debugged.

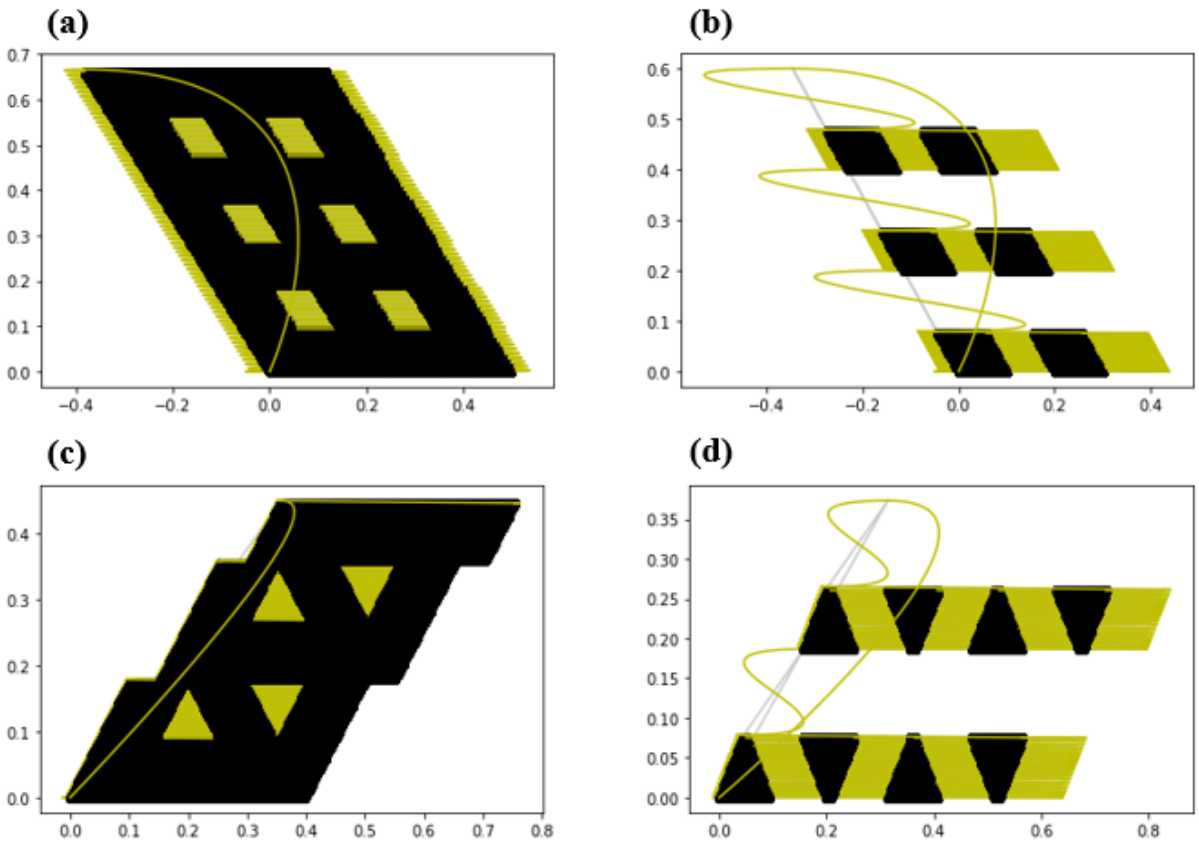

Figure 14. Illustration of the 2D graphs generated by the commands given from the .txt file to the XPS from a) rhombic pillars, b) rhombic holes, c) triangular pillars and d) triangular holes optimized codes.

6.2 Optimization of Laser Micromachining Parameters

After the trajectory codes for different geometries and types were ready, different laser micromachining parameters were tested. The optimized laser settings are the ones that present relatively smooth lines, maintaining their width and depth constant along their length, with minimum formation of recast layers. Therefore, it was anticipated that the settings that presented these characteristics are the ones that will produce well-defined geometries on the mold. As a side note, recast layers are when the ejected material resolidifies on the wall of the laser-ablated hole and may have properties different from the bulk material and, then they become undesirable (Nath 2014).

Another important factor to be considered when optimizing laser settings is the time of ablation. Depending on the choice of parameters, the time of ablation can be reduced by hours, e.g., by using higher powers and faster scanning velocities. However, the main interest was still the selection of parameters that led to well-defined geometries. To select the best

combinations of power and scanning velocities, single lines were ablated horizontally and vertically, with the parameters listed in Table 4, and then checked through confocal microscopy.

Table 4. Different powers and scanning velocities tested to select the optimized laser parameters.

Power (mW)	Scanning Velocity (mm/s)	Power (mW)	Scanning Velocity (mm/s)
20	0.1	100	1
	0.5		2
	1		3
	2		4
	4	125	1
40	0.1		2
	0.5		3
	1		4
	2	150	1
	4		2
60	0.1		3
	0.5		4
	1	175	1
	2		2
	4		3
80	0.1		4
	0.5	200	1
	1		2
	2		3
	4		4

The results from the experiments described in Table 4 are that a combination of 40 mW with 1 mm/s ($F_0 = 2598\,J$ and $PPS = 6$), 100 mW with 1 mm/s ($F_0 = 6496\,J$ and $PPS = 6$), and 100 mW with 2 mm/s ($F_0 = 6496\,J$ and $PPS = 3$) are the best parameters to be used for lasing micromachining, with experimental beam width of 5.97, 10.87, and 9.67 μm, respectively. First, all the low scanning velocities (0.1 and 0.5 mm/s) for all powers were disregarded because of the resulting undesirably long machining time. Second, powers settings above 100 mW resulted in considerable noise in the lines, for all velocities. In addition, the formation of large recast layers was seen due to high energy absorption of the material, which possibly influences the final shape of the structures. Third, for 20 mW only the very low speeds result in smooth lines, therefore, they were not further considered. As a side note, the formation of large recast layers is established when their height is equal or

higher as the depth of the hole, as seen in Figure 15a. In addition, a high quantity of noise is established when the height of the peak-to-peak noise is equal or higher as the depth of the hole, as illustrated in Figure 15b.

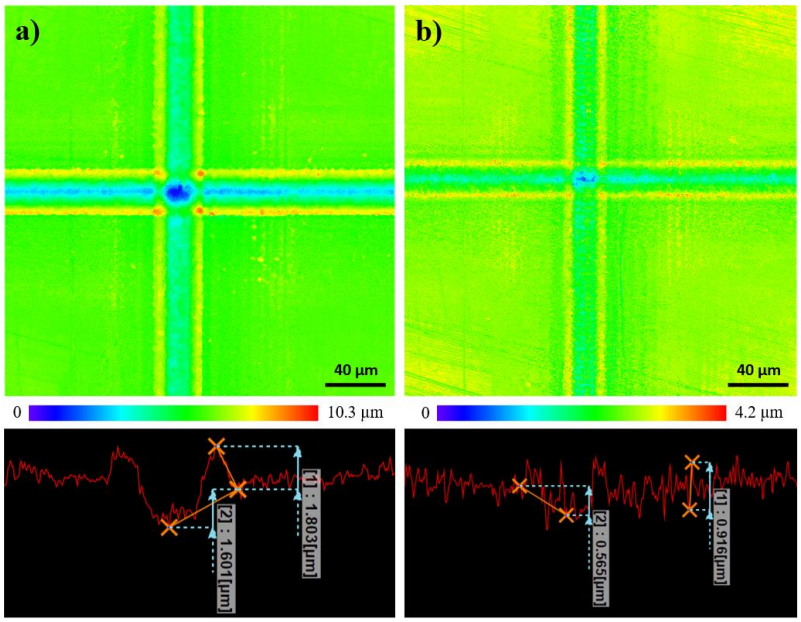

Figure 15. 2D heat maps from confocal microscopy for a) 150 mW with 2 mm/s and, b) 100 mW with 4 mm/s lines. The bottom images are the profile of a randomly picked part of the line just for comparison between the different settings.

The first combination of parameters chosen was 40 mW with 1 mm/s, since they barely presented formation of recast layers (Figure 16a), with medium scanning velocity, and small experimental beam width, allowing smaller dimensions of structures to be better defined (e.g., $a = b = 50$ µm square pillars). However, the disadvantage of this combination is that it presents the highest amount of noise in the ablated line when compared to the other optimized laser parameters. When considering the same power but higher speeds, the ablated areas were very shallow, e.g., around 0.3 µm depth of a single line for 2 mm/s. So, these velocities for 40 mW were not further considered. The second combination chosen was 100 mW with 1 mm/s (Figure 16b), since they presented a smooth ablated line, with medium scanning velocity and high depth for a single line. The drawback of these settings was the formation of larger recast layers (as it can be seen in the red areas of Figure 16b), when compared to the other optimized parameters, which could be detrimental for the shape of geometries. Finally, the third combination chosen was 100 mW with 2 mm/s (Figure 16c), because it can ablate surfaces much faster, with relatively moderate noise and medium formation of recast layers.

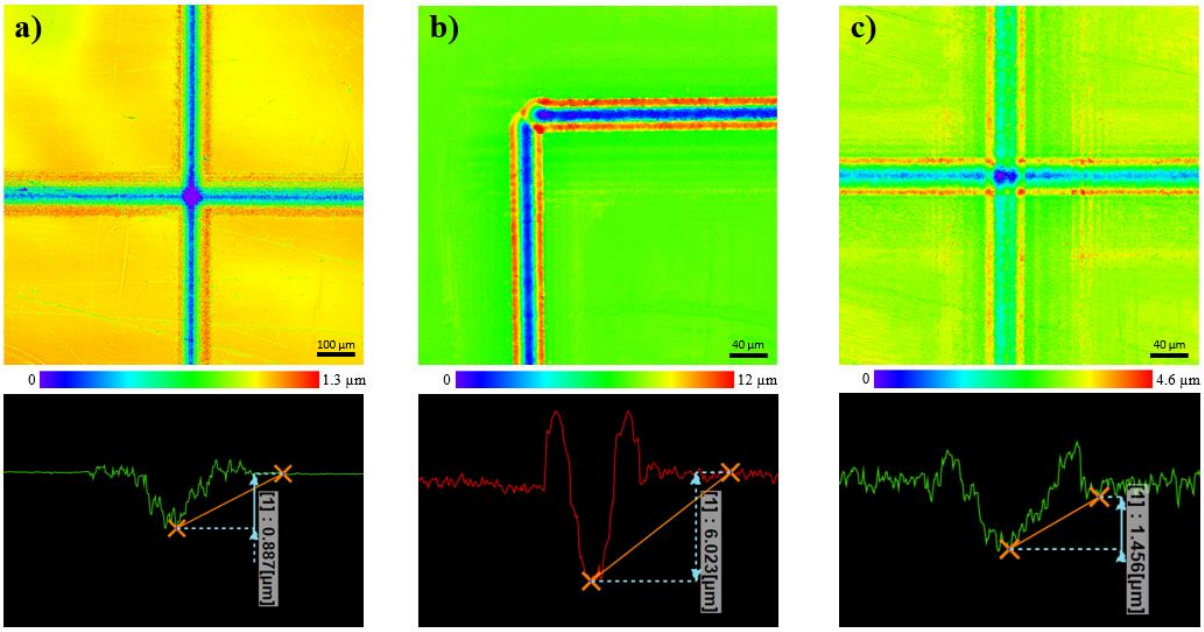

Figure 16. 2D heat maps from confocal microscopy for a) 40 mW with 1 mm/s, b) 100 mW with 1 mm/s, and c) 100 mW with 2 mm/s lines. The bottom images are the profile of a randomly picked part of the line just for comparison between the different settings.

The square pillar and hole geometries were chosen for laser micromachining. These patterns were scanned with 90% line overlap. That is because previous proof of concept experiments from former students at the Biomimetic Surface Engineering Laboratory show that 90% line overlap mostly led to well-defined geometries if the other parameters are effectively selected. The patterns were lased first with 1 overscan, and then the number of overscans were increased to check if the shape remained unaltered.

The first combination of laser parameters tested was a power of 100 mW, scanning speed of 2 mm/s and 3 overscans. Figure 17 presents the 2D heat maps from confocal microscopy of each dimension tested, considering $a = b$ for square pillars and holes.

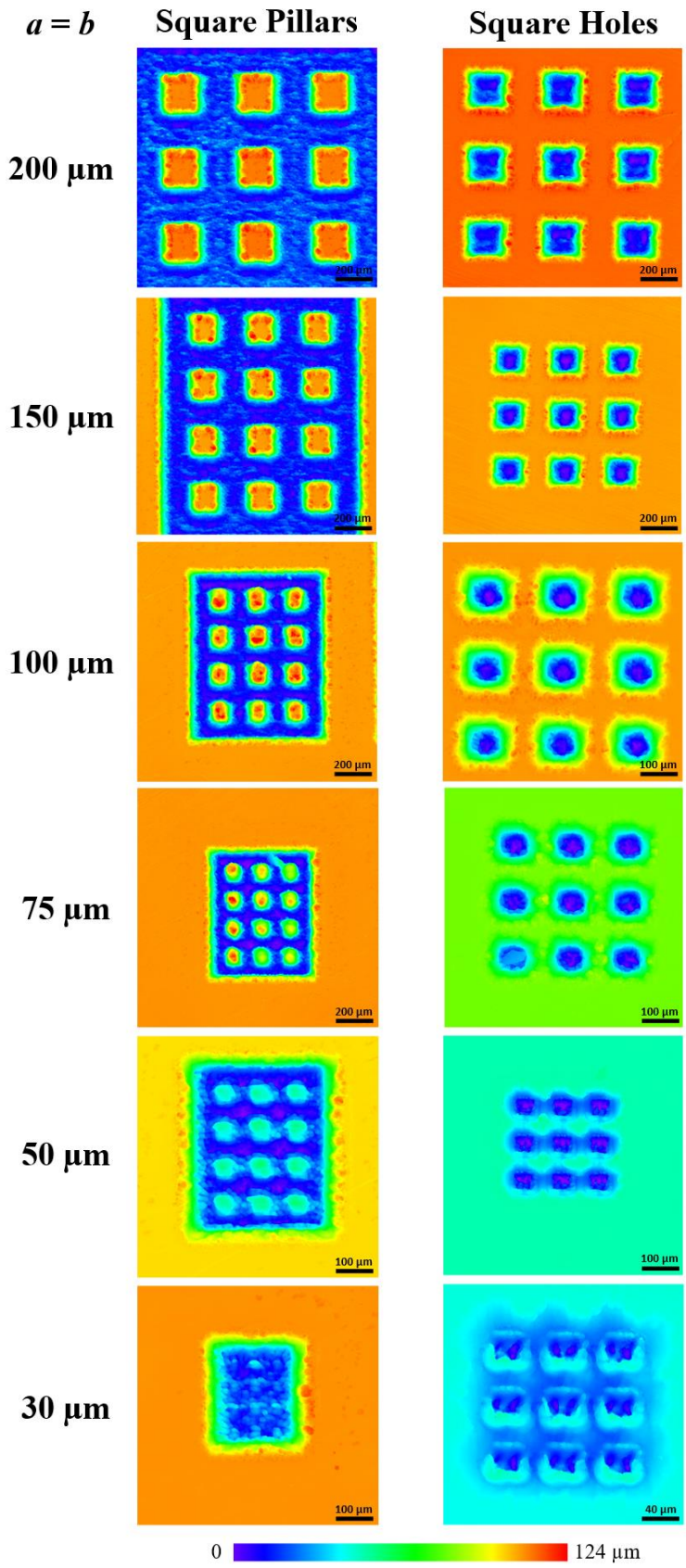

Figure 17. 2D heat maps from confocal microscopy for different *a* and *b* laser-micromachined square pillars and holes on SS by using power of 100 mW, scanning speed of 2 mm/s and 3 overscans.

As it can be noticed from Figure 17, structures smaller than $a = b = 75$ µm for square pillars and holes, presented problems. The $a = b = 50$ µm square pillars and holes showed a very small height/depth of the squares (e.g., 25 and 30 µm, respectively), when compared to the $a = b = 75$ µm squares, with average height/depth of 80 and 72 µm. For the $a = b = 30$ µm square pillars, no geometrically distinct structures were formed. Due to the Gaussian beam shape, the beam ablated partially the pillars while ablating the spacing between them, and since the pillars are fragile due to their significantly small dimension *a*, it was impossible to precisely shape them with these laser settings. On the other hand, for $a = b = 30$ µm square holes, the squares were properly ablated, however, with a high quantity of redeposition particles at the edges of the squares, also with considerably small depth (25 µm) after 3 overscans.

Upon analysis of the results found for $a = b = 50$ µm, and $a = b = 30$ µm for both square pillars and holes by using 100 mW, 2 mm/s and 3 overscans, the same dimensions were then ablated by considering 100 mW, 1 mm/s and 2 overscans. Figure 18 presents the 3D heat maps from confocal microscopy of the results.

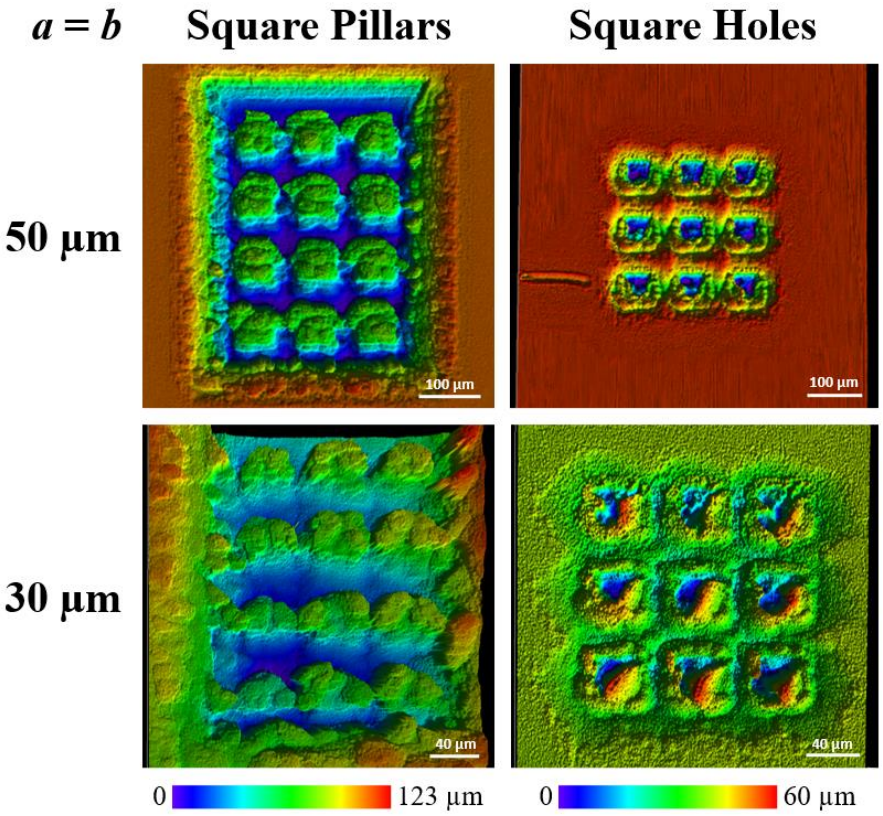

Figure 18. 3D heat maps from confocal microscopy for $a = b = 50$ µm, and $a = b = 30$ µm laser-micromachined for square pillars and holes by using 100 mW of power, 1 mm/s of scanning speed and 2 overscans.

With the laser power remaining the same at 100 mW while the scanning velocity is reduced by half (i.e., from 2 to 1 mm/s), the number of PPS is also cut in half (i.e., from 6 to 3 PPS). As it can be seen from Figure 18, the $a = b = 50$ µm square pillars was the only pattern considerably improved from the PPS reduction. The other patterns presented a high amount of redeposition of nanoparticles between the structures for the case of square pillars, and on top of the holes for the square holes, that were not removed during the process of sonication. To prevent this nanoparticles redeposition, the same patterns were produced again, but with nitrogen gas flow during lasing micromachining. Unfortunately, the nitrogen gas flow did not remove or partially remove the redeposited nanoparticles on the patterns. Instead, the nitrogen gas flow increased the degree to which the underlying structured surface was covered with large nanoparticle agglomerates. According to Wood et al. (2021) an increase in the gas flow rate results in confinement of the expanding nanoparticle plume, causing nanoparticles ejected from the substrate to agglomerate. Only after injection molding and hot press experiments, it was realized that all patterns still presented redeposition particles, which had never been completely removed by sonication, which interfered in the data analysis of the mold samples. Steady state in the mold structure dimensions was only achieved after about 4 cycles of molding, as it is presented in the next sub-chapter.

One more laser parameter combination was tested for $a = b = 50$ µm, and $a = b = 30$ µm, which is 40 mW, 1 mm/s and 4 overscans. Figure 19 shows the 3D heat maps from confocal microscopy by using these new laser settings.

This change in laser settings means that by reducing the power from 100 mW to 40 mW, the fluence is reduced in 60% (i.e., from 6496 to 2598 J), while keeping the scanning velocity at 1 mm/s, the number of PPS remains the same as when considering 100 mW and 1 mm/s (i.e., 3 PPS). Figure 19 shows that laser micromachining with 40 mW and 1 mm/s improved the square hole structures. However, no improvement was noticed for the $a = b = 50$ µm square pillars, and no structures were formed for $a = b = 30$ µm square pillars. The explanation for the latter is the same as described for when using power of 100 mW, scanning speed of 2 mm/s and 3 overscans.

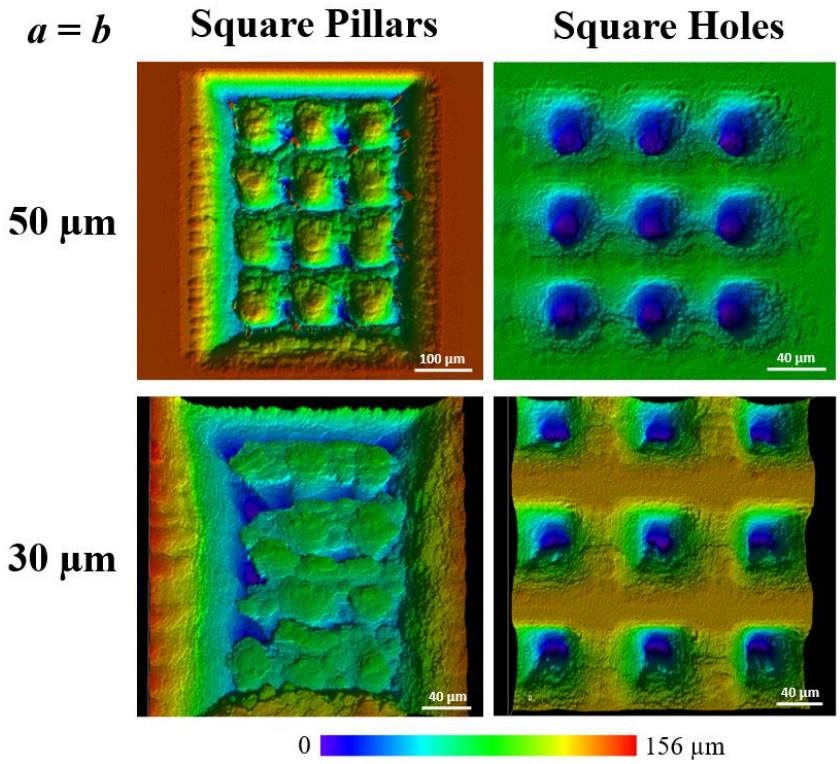

Figure 19. 3D heat maps from confocal microscopy for $a = b = 50$ µm, and $a = b = 30$ µm laser-micromachined for square pillars and holes by using 40 mW of power, 1 mm/s of scanning speed and 4 overscans.

Since for all optimized laser settings, there were no satisfactory results for $a = b = 30$ µm square pillars by using the here chosen lens with 25mm focal length, $a = 50$ µm for pillar geometries was set as the minimum value that the current laser settings can achieve without damaging and compromising the features. Following and in addition to the square features tested up to now, $a = b = 50$ µm hexagonal pillars and holes were produced with alike laser settings with 4 overscans, to check whether there would be any difference in the shape and formation of the hexagonal features. Figure 20 illustrates the 3D heat maps of these results from confocal microscopy.

From the analysis of Figure 20, it can be inferred that 40 mW with 1 mm/s was the best combination of laser parameters for hexagonal pillars, creating well shaped hexagonal structures. For the hexagonal holes, all of them presented a cylindrical shape, with slightly better results from 40 mW with 1 mm/s. It was concluded that these settings also work for bigger dimensions, as had been observed with squares.

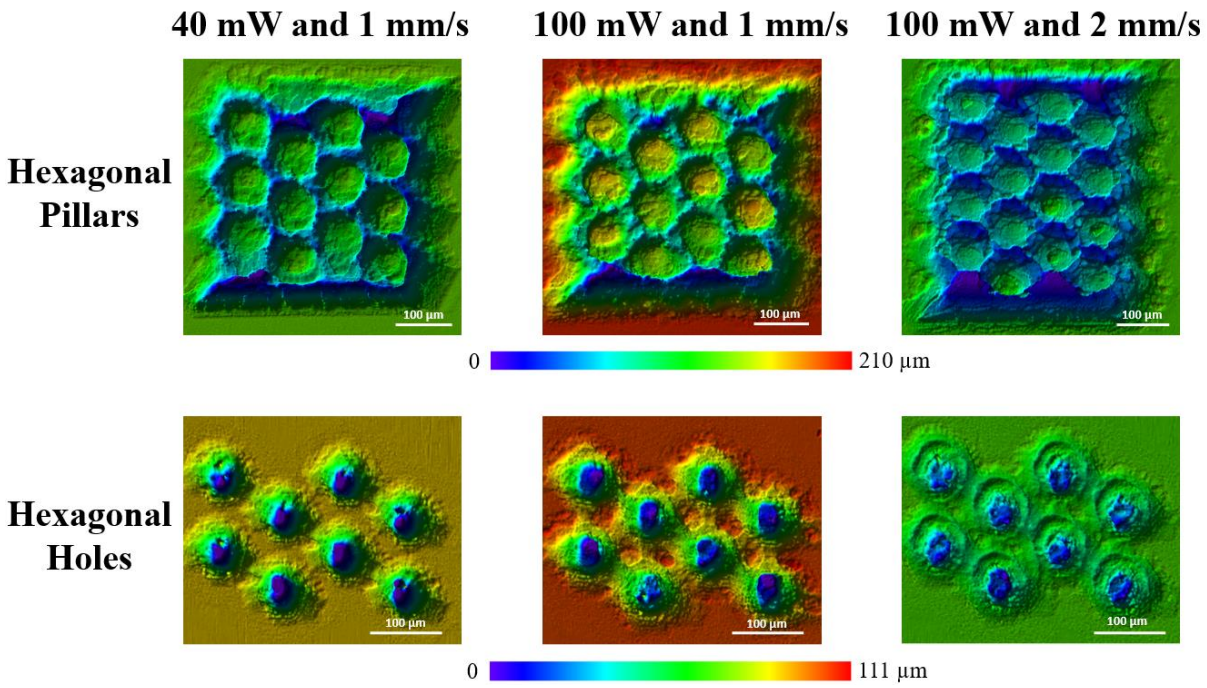

Figure 20. 3D heat maps from confocal microscopy for the $a = b = 50$ µm hexagonal pillars and holes with all the optimized laser parameters with 4 overscans.

Table 5 lists a summary of the optimized laser settings that were used to ablate the dimensions of interest of square and hexagonal features, both in pillar and hole types. The settings marked with "✓" are the ones that presented well-defined geometrical features, and the ones marked with "×" are the settings that which did not present well-defined features upon laser micromachining. As it can be seen, 40 mW with 1 mm/s is the combination of laser settings that works in all geometries and types, with structures bigger than $a = b = 50$ µm. It is important to remember that these laser settings are based on ablating with a 1 kHz femtosecond laser, 800 nm of wavelength, 25.4 mm bi-convex focusing lens and 90% overlap of lines.

Table 5. Summary of all laser settings that can be used to ablate the particular dimensions for well-defined squares and hexagons, both in pillar and hole types.

Geometry and type lased on the mold	Dimensions *a* and *b* (μm)	**Optimized Laser Settings**		
		40 mW and 1 mm/s	100 mW and 1 mm/s	100 mW and 2 mm/s
Square Pillars	30	×	×	×
	50	✓	✓	×
	75	✓	✓	✓
	100	✓	✓	✓
	150	✓	✓	✓
	200	✓	✓	✓
Square Holes	30	✓	×	×
	50	✓	×	×
	75	✓	✓	✓
	100	✓	✓	✓
	150	✓	✓	✓
	200	✓	✓	✓
Hexagonal Pillars	50	✓	×	×
Hexagonal Holes	50	✓	×	×

6.3 Surface Analysis Through Confocal Microscopy

The procedure used to extract the dimensions *a*, *b*, and *c* of the laser micromachined geometries and their polymer replicas is illustrated in Figure 21, where square pillars laser-micromachined in the mold, translate into square holes in the polymer after molding (the blue areas in the heat map images are the deep part of the patterns, and the orange/green are the top part of them). Two measurements were taken vertically, and two measurements were taken horizontally (black squares in the image). The final values of *a*, *b* and *c* were the average of these four measurements. For hexagonal pillars and holes, the measurements were taken diagonally. Whenever the structures of the mold seemed to be damaged or with redeposition nanoparticles, or the polymer replica seemed to contain debris (based on their heat maps), the data of different rows and/or columns were taken.

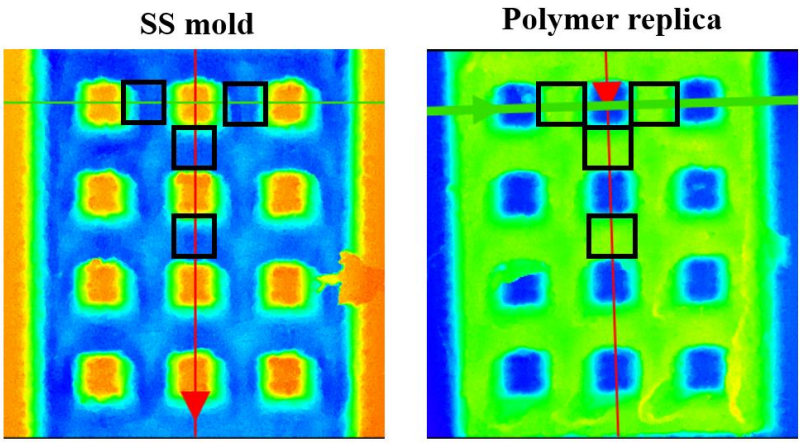

Figure 21. 2D heat maps of square pillars in the mold and the polymer replica (square holes), where the black squares illustrate where the measurements for the geometrical patterns *a*, *b*, and *c* are taken, both vertically and horizontally.

Mostly due to the lack of enough lubricant on the steel mold and inserts before molding, some polymer replicas presented "hairy micro/nanostructures" after the demolding process. When molten polymer is still not solidified during demolding, it sticks to the bottom of cavities, and when the polymer is detached from the steel insert, these hairy micro/nanostructures will be formed. It is expected that these hairy features can enhance the superhydrophobicity of the polymer part, but this aspect has not been investigated yet by our group. However, it is a challenge to measure the spacing between features of these patterns because the hairs can lead to misleading data, more specifically, increased values, as it can be noticed in the heat map of Figure 22a. In addition, another aspect that can lead to erroneous spacing between features data is the presence of polymer debris inside of hole structures on the polymer, as it seen in Figure 22b. To avoid extracting non-representative data of heat maps from confocal microscopy, the particular structures that presented any of the problems abovementioned were not consider. If all the structures of a pattern presented problems, the whole pattern was disregarded, and no data was extracted from it.

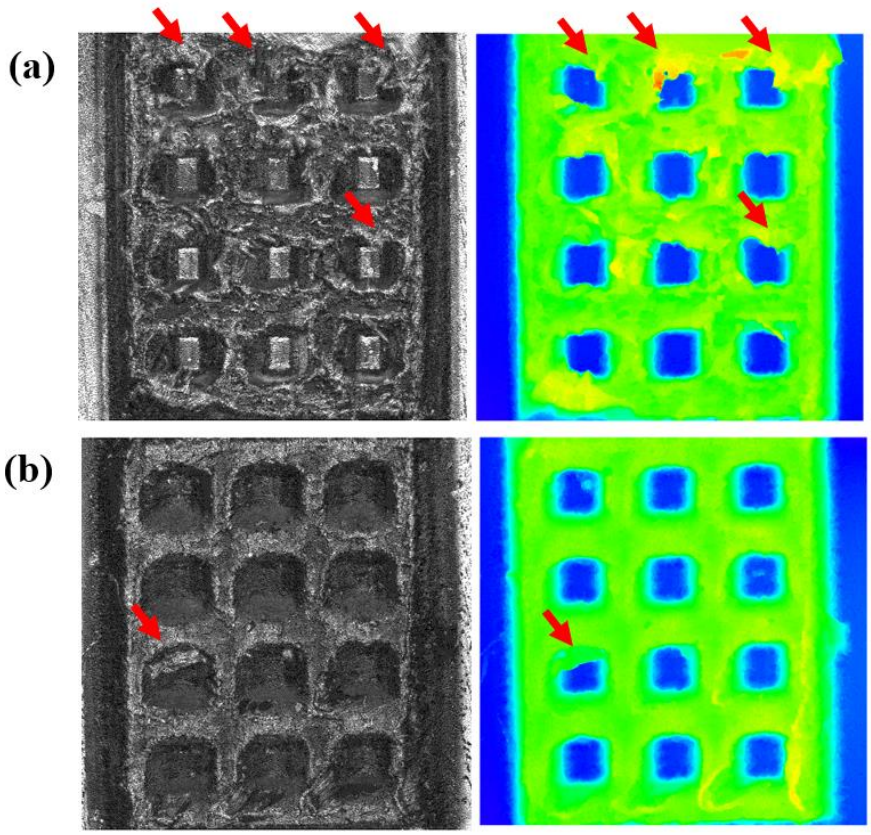

Figure 22. Intensity (left side) and 2D heat maps (right side) of square holes on the polymer replica, where red arrows point the areas where a) hairy micro/nanostructures and b) polymer debris interfere with the data extraction.

Another problem that led to misrepresentation of data was identified. Initially the measurements from the dimensions *a*, *b*, and *c* of patterns from the mold were taken after the insert was laser-micromachined and sonicated. However, only after injection molding and hot press experiments it was realized that the sonication procedure was not efficient to completely remove all the redeposited nanoparticles on the mold structures. Figure 23 shows the 2D heat maps from confocal microscopy, comparing a square pillar pattern on a steel mold right after laser micromachining (after sonication), and the same pattern after 4 hot press experiments. The red arrows indicate the areas where the presence of redeposition can be noticed (left) and the same areas upon 4 hot press experiments. It can be noticed that after 4 hot press experiments, all, or most of the redeposition nanoparticles were removed from the pillar walls, but it is still unknown if 4 hot press experiments were necessary to completely remove them or not. This aspect will be further investigated in a future work.

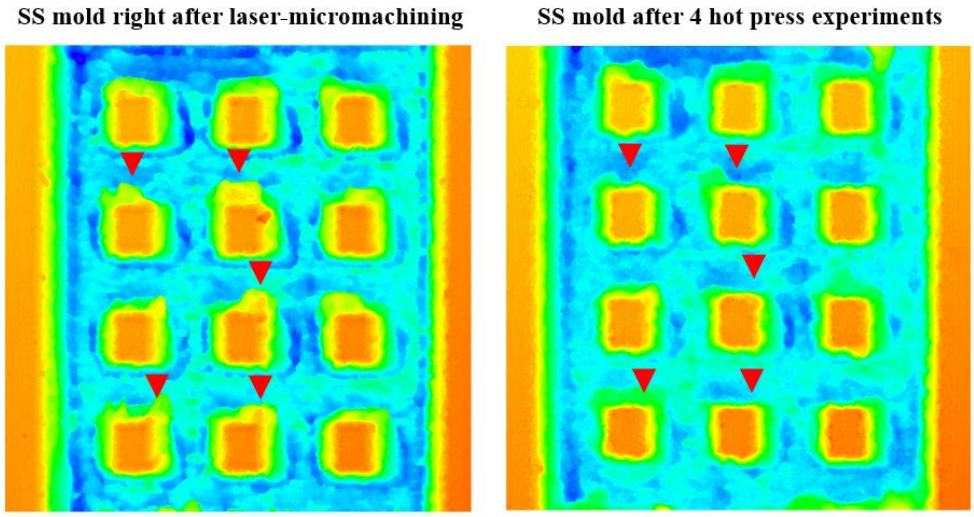

Figure 23. 2D heat maps from confocal microscopy comparing a square pillar pattern on a steel mold right after laser micromachining (after sonication), and the same pattern after 4 hot press experiments. The red arrows indicate the areas where it can be noticed the presence of redeposition and their removal after 4 hot press experiments.

To further investigate how the removal of the redeposited particles affects the values of *b* and *c* of pillar patterns, different square and hexagonal pillar patterns were produced on the SS cylindrical mold according to Table 6. The dimensions *b* and *c* of these patterns were quantified, comparing their values for the patterns right after laser micromachining (after sonication), and after 4 hot press experiments. Due to some non-identified laser issue, the pillar structures from pattern number 4 were damaged, as it can be seen in Figure 24a, and therefore they were disregarded. In addition, pattern number 9 after 4 hot press experiments presented a large piece of PE stuck on top of the structures, as shown in Figure 24b, and as a consequence no measurements could be taken from it. Therefore, this pattern was also disregarded.

Table 6. Experimental plan designed to assess the difference between the geometrical dimensions *b* and *c* of pillar patterns right after laser micromachining (after sonication), and after 4 hot press experiments.

Patterns laser micromachined using 25 mm lenses, 1 mm/s of speed, 90% overlap				
Pattern	Geometry and type	Dimensions *a* and *b* (µm)	Power (mW)	Overscans
1	Square Pillars	50	100	2
2		100		
3		150		
4		50		4
5		100		
6		150		
7		50	40	2
8		150		4
9	Hexagonal Pillars	50		4
10		100		
11		150		

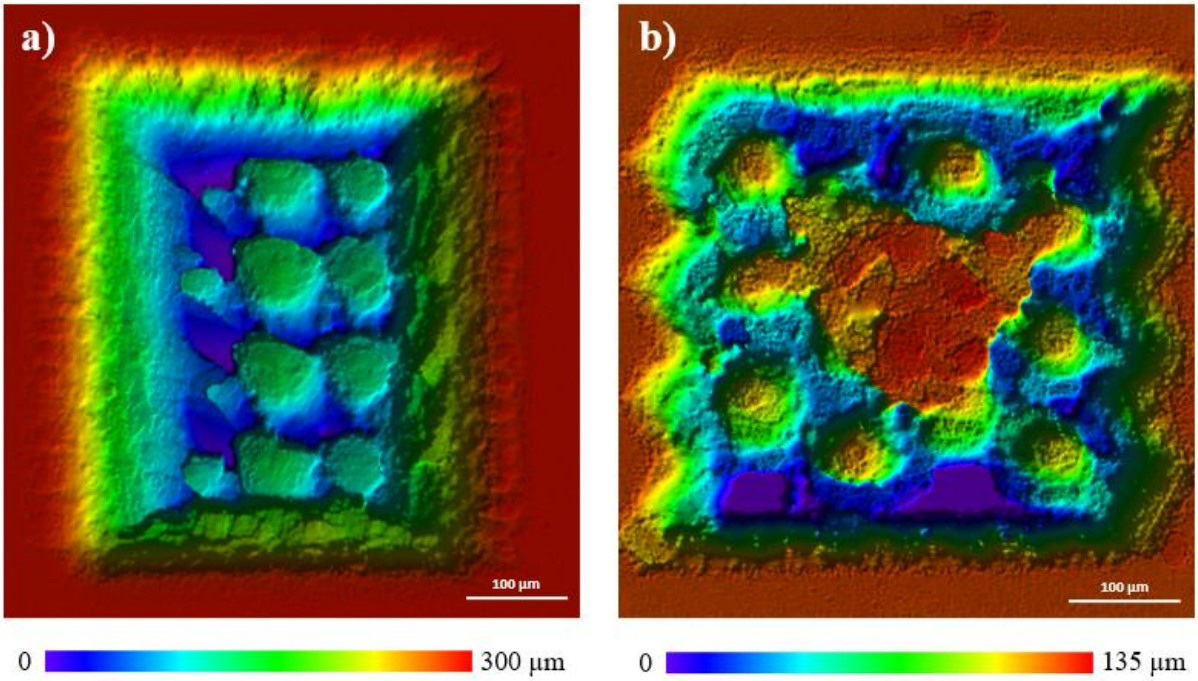

Figure 24. 3D heat maps from confocal microscopy showing the problems with pattern number 4 right after laser micromachining (after sonication), and pattern number 17 after 4 hot press experiments.

For the different pillar structures from Table 6, Figures 25 and 26 present a comparison of the experimentally measured features *b* and *c*, respectively, right after laser micromachining, and after 4 hot press experiments.

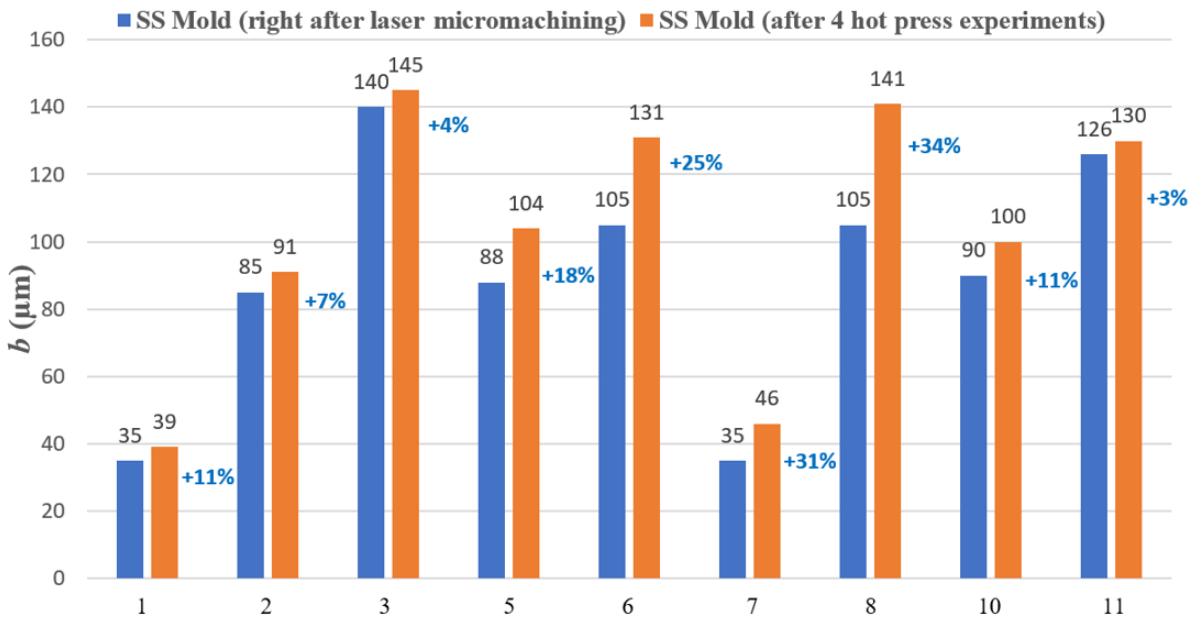

Figure 25. Spacing between features comparison graph of the mold pillar structures from Table 6, right after laser micromachining, and after 4 hot press experiments.

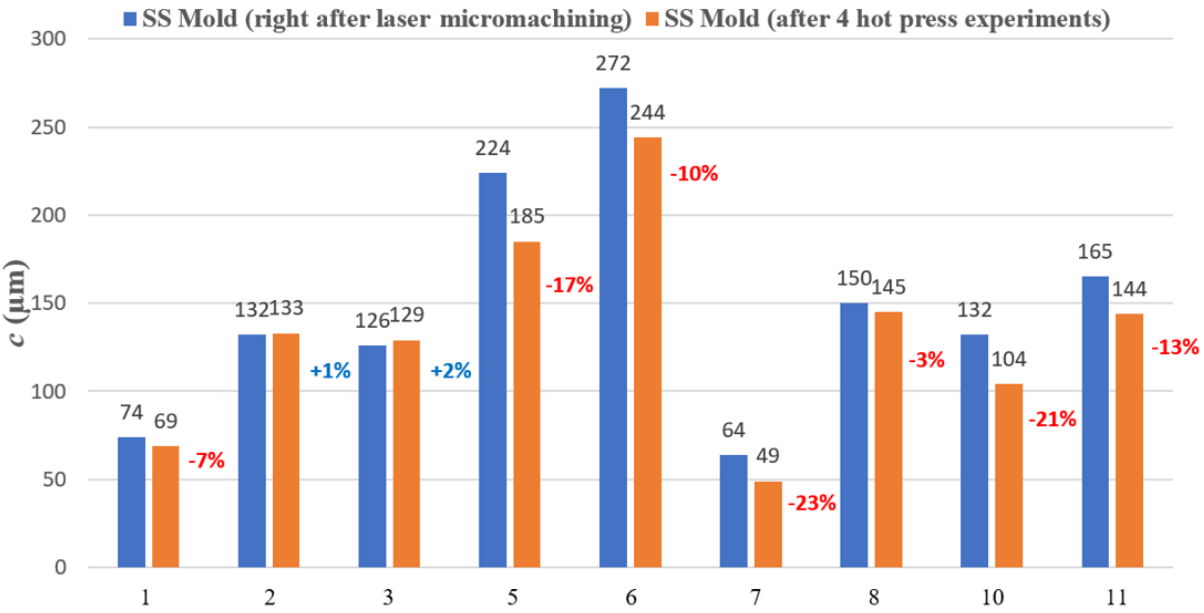

Figure 26. Depth comparison graph of the mold pillar structures from Table 6, right after laser micromachining, and after 4 hot press experiments.

From Figure 25 it can quickly be seen that overall, the feature *b* (spacing between features) increases with repeated hot press experiments, while Figure 26 highlights that the feature *c* (depth) decreases. Across all pillar structures, an average increase of 16% in the spacing between features and a decrease of 10% in depth was determined. These values can be explained by taking the redeposited particles into consideration. Typically, these attach at

the side of pillar structures during laser micromachining as seen in Figure 23. That is because the nanoparticles that are being ejected from the steel during ablation redeposit on top and on the side of the pillars. Under polymer molding conditions, the redeposited particles are dislodged and pushed to the bottom of the cavities by the molten polymer, which increases the spacing between features values and decreases the depth values upon subsequent hot press experiments.

6.4 Optimization of Hot Press Molding Parameters

Optimized hot press settings mean that the polymer will completely penetrate the microcavities with the highest depth possible, replicating the nanostructures created during laser micromachining at the bottom of the cavities. As already stated, the replication of hierarchical structures is crucial to fabricate superhydrophobic polymer surfaces, also maintaining the Cassie-Baxter wetting state.

Figure 27 shows the step-by-step process of hot pressing after the cylindrical stubs and the mold are properly lubricated. The final PE samples have 1 mm thickness for 0.6 g of polymer.

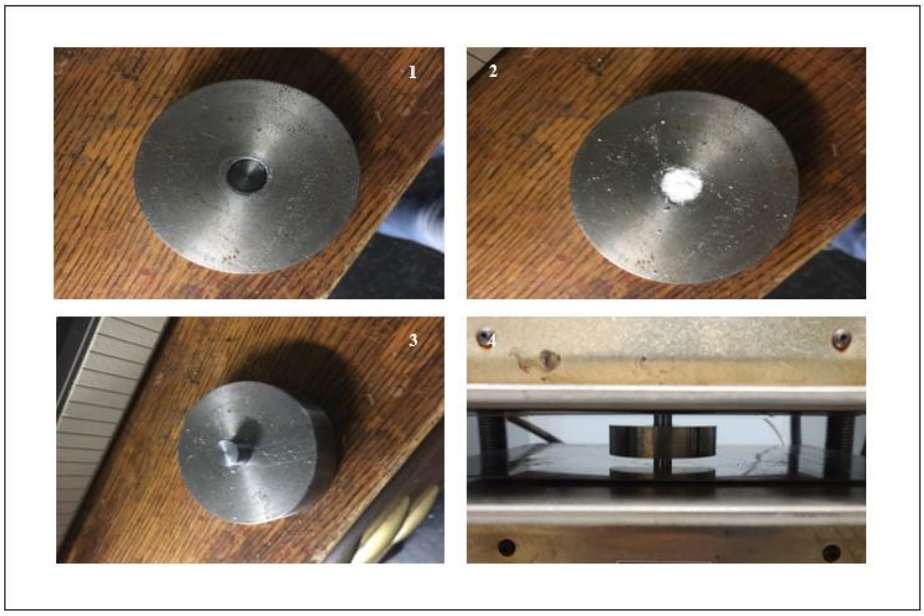

Figure 27. Step process of hot pressing after lubricating the donut hole, the micromachined insert and a flat insert: 1) place micromachined insert into the donut hole, 2) add from 0.5 to 0.6 g PE on top, 3) place a flat blank insert on top, sandwiching the mixture, and 4) place between hot plates in hot press.

The square pillar and hole patterns presented in Figure 17 that were produced on a cylindrical steel insert were used to test the first hot press experiments. The fixed parameters used in the hot press experiments were plates at temperature 230 °C (which is about the same temperature used at IPL Inc. in injection molding of PE), and a cooling time of 25 minutes. For the cooling process, the plates are effectively water cooled with water at a temperature of around 10 °C, which passes through the cooling channels, transferring heat with the plates.

The first trials were run as follow, with the conditions stated on Table 7:

1. Heat plates to T_1;
2. Place mold into press;
3. Apply pressure P_1 for a duration of t_1;
4. Release pressure;
5. Cool plates for t_2.

Table 7. Hot press experiment conditions for the first trials.

Hot Press Experiment	T_1 (°C)	P_1 (psi)	t_1 (min)	t_2 (min)
1	230	2000	30	25
2	230	3000	30	25

The resulting PE polymer replicas from the hot press experiment 1 did not present the alike high/deep structures as the mold patterns, for most of the dimensions in both pillars and holes. Then, in a next trial (hot press experiment 2) keeping the same methodology but increasing the pressure to 3000 psi, the polymer completely leaked out of the mold, and no sample was formed.

After careful revision of the hot press methodology by comparing it with injection molding, two steps were missing during the first hot press experiments. These steps are applied during injection molding and are crucial to ensure more faithful replicas with higher depth polymer penetration. First, the polymer must be molten before the pressure is applied, to ensure that it enters the cavities. Applying the pressure while the polymer is still solid does not force it to enter the cavities, and therefore a poor replication will happen at the end. So instead of applying 2000 psi of pressure and leaving for 30 minutes as before, we then applied a small pressure at the beginning, and waited some minutes until the pressure drops to 0. That time is crucial for the heat transfer to occur between the plates and the steel mold and inserts, arriving at the polymer and melting it. The pressure dropping to 0 indicates that the

polymer is molten, and then the 2000 psi of pressure should be applied. Second, the pressure should be kept constant while cooling the mold and the polymer, so that the molten polymer that is being pressurized until the bottom of the cavities is cooled down. As a consequence, the polymer solidifies replicating the nanostructures at the bottom of the cavities. If the pressure is released before cooling down as we were doing before, the molten polymer will retract inside the cavities, not replicating the nanostructures at the bottom of the cavities, in addition to lower the depth polymer penetration. Keeping the pressure while cooling down ensures a reduction in polymer shrinkage, that happens due to thermal stress (Guo et al. 2006).

Afterwards, the next hot press experiments were run as follow, keeping the same methodology but altering t_2,with the conditions presented in Table 8:

1. Heat plates to T_1;
2. Place mold into press;
3. Apply pressure P_1 for a duration of t_1;
4. Apply pressure P_2 for a duration of t_2;
5. Cool plates for t_3;
6. Release pressure.

Table 8. Hot press experiment conditions using the new methodology.

Hot Press Experiment	T_1 (°C)	P_1 (psi)	t_1 (min)	P_2 (psi)	t_2 (min)	t_3 (min)
3	230	500	10	2000	20	25
4	230	500	10	2000	30	25
5	230	500	10	2000	60	25

The mold patterns used for these three hot press experiments were the ones mentioned in Table 6. Yet only patterns 2, 3, 8 and 11 were considered for the comparison between the three different hot press experiments, because these patterns were the only ones that had PE replicas without any problems for all hot press experiments. The problems found on the remaining patterns are the ones explained in the sub-chapter 6.3.

Table 9 shows the results, in which the *b* and *c* dimensions of the SS mold patterns were measured after 4 hot press experiments to ensure that the redeposited nanoparticles are pushed to the bottom of the cavities.

Table 9. Comparison between the *c* values from the SS mold pillar patterns (from Table 6) with their respective PE replicas from hot press experiments 3, 4 and 5. SS mold *b* and *c* values were measured after 4 hot press experiments.

Pattern	SS mold			PE replica - Hot press experiment 3	PE replica - Hot press experiment 4	PE replica - Hot press experiment 5
	c (µm) Average	*b* (µm) Average	Aspect ratio	*c* (µm) Average	*c* (µm) Average	*c* (µm) Average
2	133	91	1.46	122 -8%	132 -1%	127 -5%
3	129	145	0.89	126 -1%	124 -4%	127 -2%
8	145	141	1.03	147 +1%	155 +7%	152 +5%
11	144	130	1.11	146 +1%	143 -1%	140 -3%

As seen in Table 9, all experiments resulted in similar penetration depth. However, slightly more faithful replicas were found for the hot press experiment 4 (with t_2 = 30 min).

6.5 Injection Molding

The injection molding campaign was conducted at IPL Inc. facility, located in St-Damien, QC. The whole process from machining the IPL mold until the fabrication of the polymer container, with the SEM images of the mold and the polymer replica is displayed in Figure 28.

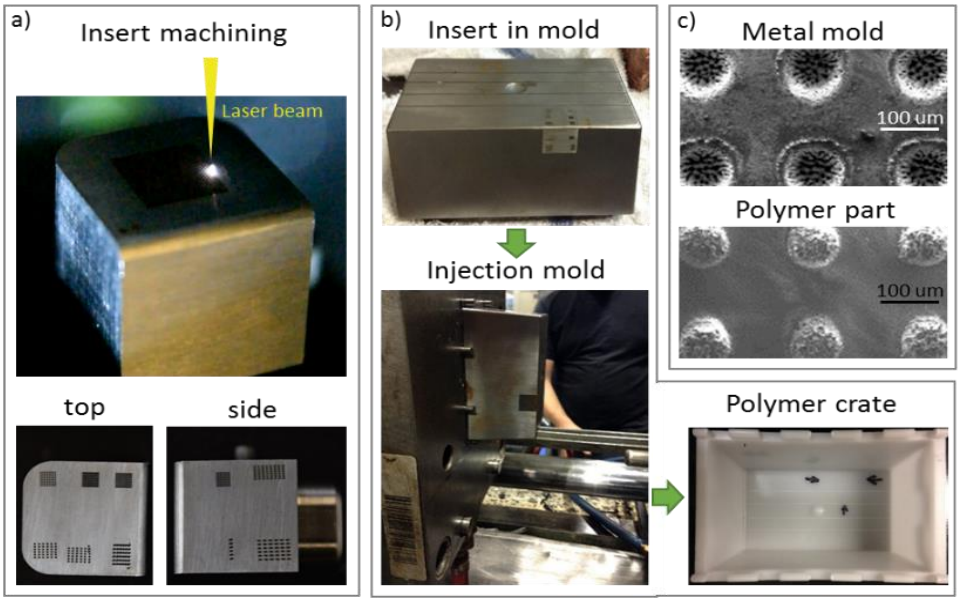

Figure 28. Illustration of a) P20 steel insert laser-machining, b) industrial injection molding process, c) SEM images of metal mold and polymer part.

After the steel inserts were sent to McGill, they were laser-micromachined, sonicated, and sent back to IPL Inc. Due to the ongoing pandemic restrictions, the engineers at IPL Inc. conducted the experiments in my absence. The main parameters used during the injection molding campaign at IPL, for both PE and PP are described in Table 10.

Table 10. Main parameters used for the injection molding campaign at IPL Inc. for both PE and PP.

Parameters	**PE**	**PP**
Cycle time (s)	19.8	15.6
Cooling time (s)	11	9
Screw rotational speed (rpm)	351	357
Injection pressure (bar)	48	69
Injection speed (mm/s)	100	100
Molding temperature (°C)	235	213

6.6 Contact Angle Measurements for Thermodynamic Optimization Codes

The goniometer was used only once in the scope of this thesis to measure the contact angle of H_2O on PE, at room temperature (20 ºC), which is a crucial value to be used in the thermodynamic optimization equations.

A syringe gently deposited a 5 µL water droplet at a rate of 0.25 µL/s on top of a flat PE surface. The water droplet is illuminated from behind with a white backboard, and then a zoomed photo of the droplet is taken. After that, the PE flat sample is dried in the oven for 10 minutes at a temperature of 60 ºC, and then the procedure is repeated. Three images are taken, analyzed through the software, and averaged. Table 11 presents the contact angle (CA) values measured by the software for all three images from H_2O on PE and the final average. The contact angle of 95º found for H_2O on PE at room temperature matches with data published by Luna et al. (2014).

Table 11. CA left, right, and average values measured from three images of H_2O on PE and the final average.

Sample	CA Left	CA Right	Average
H2O on PE - 1	97.6	99.3	98.5
H2O on PE - 2	93.8	94.5	94.2
H2O on PE - 3	91.8	91.9	91.9
H2O on PE - Average	**95**		

For the contact angle of PE on SS, a different approach was followed. Since the PE needs to be heated up until the desired temperature (which is the temperature used in the molding process to melt the polymer – 230 ºC in this study), the goniometer could not be used. However, three pellets of PE weighing 0.0277, 0.0273 and 0.0264 g were placed on top of a polished SS substrate with roughness average (Ra) = 2.53 µm in the hot press with both plates at 230 ºC and, with the superior plate at around 5 cm distance from the pellets. After 20 minutes, with the pellets in a liquid state, a zoomed picture was taken from a Samsung Galaxy S20 Plus. The SCA 20 module software from the goniometer was used to try to measure the CA from the PE on SS. However, since the quality of the images were not as good as the camera used in the goniometer, the software failed in identifying the edges of the PE droplets. Therefore, an open-source software ImageJ with the DropSnake plugin was used to measure the contact angles. Unlike the SCA 20 module software that identify the droplet edges and automatically calculates the CAs, in ImageJ the droplet edges are traced manually. The CA values for the three PE pellets were measured and averaged and are displayed in Table 12.

Table 12. CA left, right, and average values measured from three images of PE on SS and the final average. SS with Ra = 2.53 µm and 20 min under heating.

CA Measurements - Ra = 2.53 µm and 20 min			
Sample	**CA Left**	**CA Right**	**Average**
PE on SS - 1	116.7	106.5	111.6
PE on SS - 2	109.4	112.0	110.7
PE on SS - 3	115.6	116.3	116.0
PE on SS - Average	**113**		

To make sure that the contact angle was 113º for PE on SS, the same experiment was repeated, but now with a better polished SS sample with Ra = 1.98 µm and with the three pellets under heating for 10 minutes. The weights of the pellets were 0.0292, 0.0268 and 0.0258 g. The new results are shown in Table 13.

Table 13. CA left, right, and average values measured from three images of PE on SS and the final average. SS with Ra = 1.98 μm and 10 min under heating.

CA Measurements - Ra = 1.98 μm and 10 min			
Sample	**CA Left**	**CA Right**	**Average**
PE on SS - 1	82.8	79.2	81.0
PE on SS - 2	73.1	64.5	68.8
PE on SS - 3	61.2	61.7	61.5
PE on SS - Average	**70**		

The difference in the contact angle for PE on SS for the first and second experiment (113 and 70º, respectively), can be explained by the decrease in the Ra value from the polished SS samples, and the reduced effect of thermal oxidation of PE due to the lower exposure time under heating. Those reasons led the contact angle to drop from 113º to 70º. Considering that the typical samples before laser machining come with a roughness of a range from $1.98 \leq Ra \leq 2.53$ μm, and with different PE heating times, the two values were averaged 92º. However, all three values were considered in the thermodynamic optimization codes for comparison.

7 INJECTION MOLDING WITH PE AND PP

In this chapter the mold design and the results from the injection molding campaign at IPL Inc. are presented.

7.1 Mold Design for Injection Molding

Upon preparation of the laser machining codes for squares and hexagons, pillars and holes, and subsequent optimization of laser parameters, an experimental plan for laser micromachining a steel insert for injection molding at IPL Inc. was developed (Table 14). This plan was designed so that these geometries and types could be compared, also assessing the injection molding limitations based on different dimensions (*a*, *b*, and *c*). In addition, two different laser parameters, 100 mW with 1 mm/s, and 40 mW with 1 mm/s, were tested for square pillars and holes to compare the quality replication for different laser settings. These particular two laser settings were chosen since they laser micromachined well-defined geometrical features in a broader range of dimensions, as presented in Table 5.

The first polymer to be injection molded was PP with 350 cycles. Right after, the polymer was changed to PE and 300 more cycles were run.

Table 14. Experimental plan designed for injection molding campaign at IPL Inc.

Patterns laser micromachined using 25 mm lenses, 1 mm/s of speed, 90% overlap				
Pattern	Geometry and type	Dimensions *a* and *b* (µm)	Power (mW)	Number of overscans
1	Square Pillars	50	100	2
2		100		
3		150		
4		50		4
5		100		
6		150		
7		50	40	2
8		150		4
9	Square Holes	50	100	2
10		100		
11		150		
12		50		4
13		100		
14		150		
15		50	40	2
16		150		4
17	Hexagonal Pillars	50	40	4
18		100		
19		150		
20	Hexagonal Holes	50	40	4
21		100		
22		150		

7.2 Robustness over time: Effect of Different Cycles - Same Geometry and Dimension

To analyze the robustness over time in the quality of the replicated structures, the PP samples fabricated at the 50th, 200th and 350th injection cycle, and the PE samples from the 1st, 150th and 300th were compared. For this comparison, the pattern number 3 from Table 14 was chosen. Figure 29 shows 3D heat maps from confocal microscopy of the laser machined steel mold and the respective replica of each injection molding cycle abovementioned. To simplify the identification of the images the numbers after PP or PE are the cycle numbers, e.g., *PE 001* represents the PE replica from the 1st cycle. In addition, the number before SS

stands for the pattern enumerated in Table 14. An important factor is that all images from the SS mold patterns were taken after the insert was micromachined and sonicated, yet before injection molding.

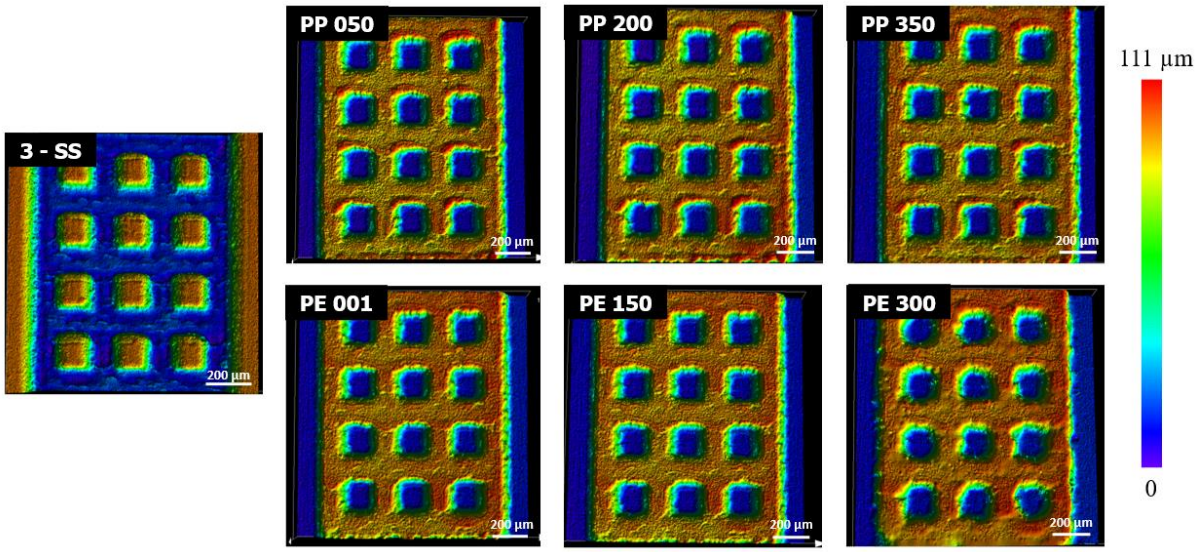

Figure 29. 3D heat maps from confocal microscopy of 3 – SS, and its polymer replicas PP 050, PP 200, PP 350, PE 001, PE 150, and PE 300 from injection molding.

From the analysis of the heat maps in Figure 29, it can be inferred that only PE 300 presented distorted square hole structures, as the edges of the squares appear rounded such that the features resemble cylinders. This observation is attributed to polymer incrustations which can be seen on the mold after cycle 500th (350 from PP and 150 from PE), as illustrated with Figure 30, causing the changes in shapes observed in PE 300. A mold cleaning procedure should be developed to remove these firmly attached polymers in future work.

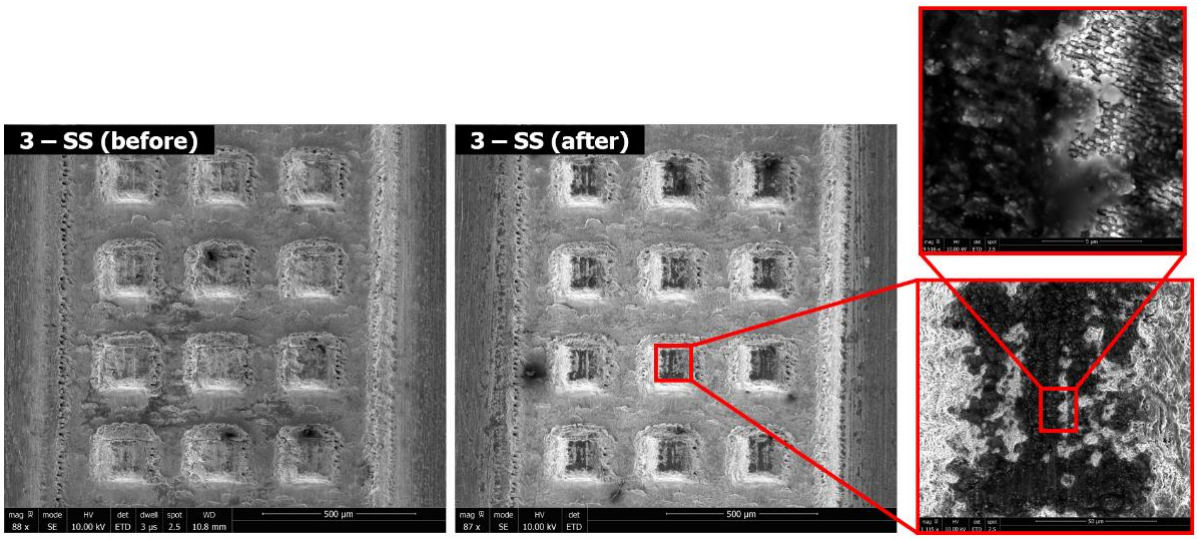

Figure 30. SEM images of 3-SS before and after injection molding campaign. Polymer incrustations can be seen on the latter.

7.3 Quality of Imprint for the Late Cycles

The quality of imprint for the late cycles, PP 350 and PE 150 were investigated for the same geometry and type, but different dimensions, and different geometries and types, but with the same dimension. PE 300 was not considered as the late cycle for PE for these analyses since all patterns presented problems of mold deterioration and polymer incrustation as discussed in the last sub-chapter. Therefore, it can be inferred that the problem occurred between PE 150 and PE 300. Further analysis would be required to precisely determine the cycle count that allows for faithful replication.

7.3.1 Same Geometry and Type, but Different Dimensions

Figure 31 shows the 3D heat maps from confocal microscopy, where 1-SS, 2-SS and 3-SS were chosen, representing the same geometry and type on the mold, but with different dimensions ($a = b = 50$ µm, $a = b = 100$ µm, and $a = b = 150$ µm) to be compared for late cycles for both PP and PE.

From the heat maps $a = b = 150$ µm structures replicated more faithfully than smaller structures ($< a = b = 150$ µm). This is because larger structures laser-machined on the mold surface present lower frictional resistance to the polymer flow. For the smaller structures,

since the frictional resistance is higher, energy dissipation happens, and under certain conditions, can cause nucleation and development of microcracks in the polymer replicated structures (Bartenev and Lavrentev 1981; Briscoe 1986). At last, no significant difference was observed between the replication quality of PP and PE.

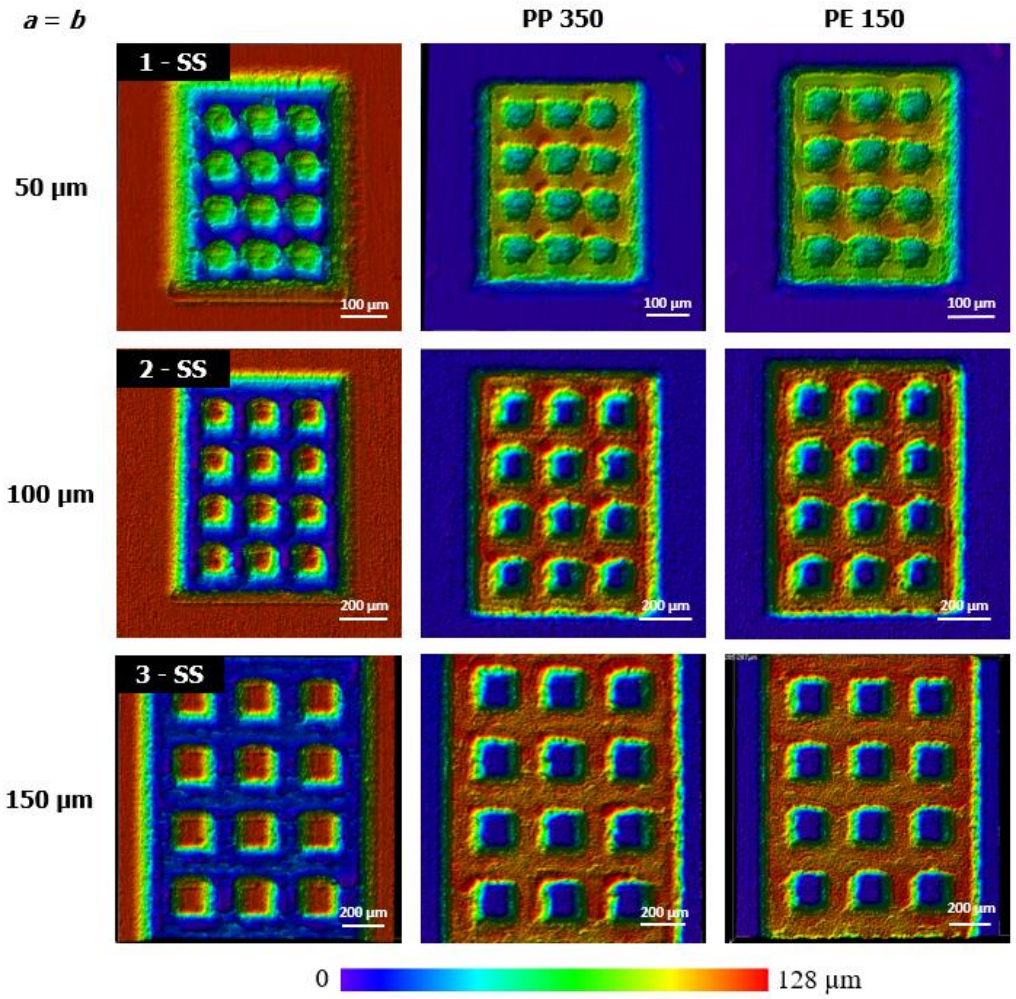

Figure 31. 3D heat maps from confocal microscopy of 1 – SS, 2 – SS and 3 -SS, and their polymer replicas on PP 350 and PE 150 from injection molding.

7.3.2 Different Geometries and Types, but Same Dimension

Figure 32 illustrates the 3D heat map from confocal microscopy, where 8-SS, 16-SS, 19-SS, and 22-SS were the patterns compared to represent the different geometries (squares and hexagons) and types (pillar and hole) on the mold, but with the same dimension ($a = b =$ 150 µm) for late cycles for both PP and PE.

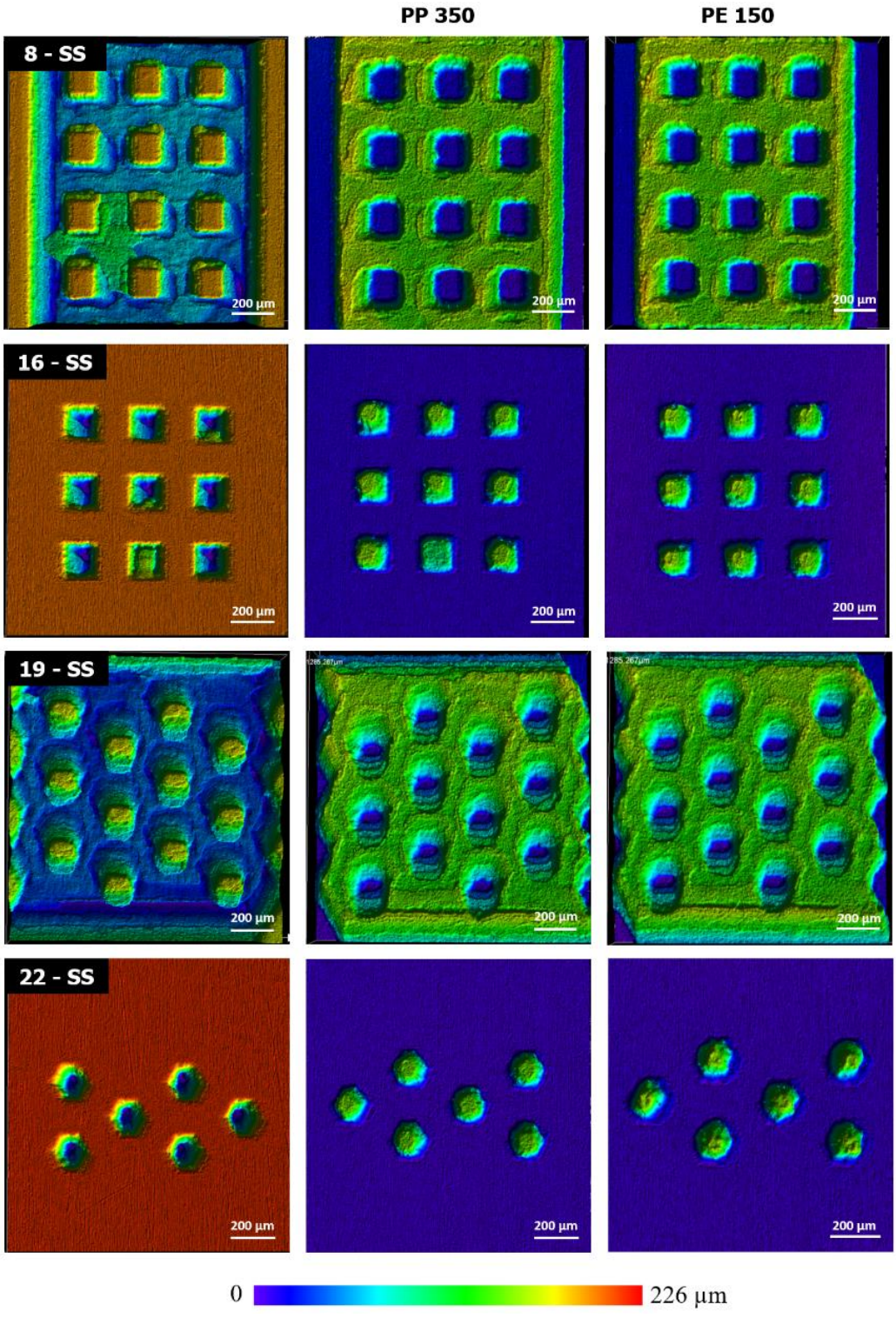

Figure 32. 3D heat map graphs from confocal microscopy of 8 – SS, 16 – SS, 19 – SS, and 22 -SS, and their polymer replicas on PP 350 and PE 150 from injection molding.

After careful analysis of the heat maps in Figure 32, it can be noticed that first, pillar structures on the mold, presented more faithful replication than hole structures on the mold.

That can be attributed to air trapped inside the holes in the mold while the molten polymer is being pressured, not allowing the polymer to reach the bottom of the cavities. For pillar structures on the mold, the air escapes sideways while the polymer is filling the cavities. Consequently, the polymer can reach the bottom of the cavities with less harsh injection molding conditions (e.g., lower holding pressure, temperature, and injection rate). Second, the actual geometry, i.e., square, or hexagonal pillars or holes did not affect polymer replication. At last, again, no significant difference was observed between the replication quality of PP and PE.

7.4 Analysis of the Nanostructures Transfer Based on Scanning Electron Microscopy (SEM)

SEM analysis was conducted to investigate whether laser machined nanostructures at the bottom of the mold cavities replicated on the raised features on the polymer replicas. Figure 33 shows SEM images of such nanostructures on 8-SS and 14-SS, and their respective replicas on PE 300.

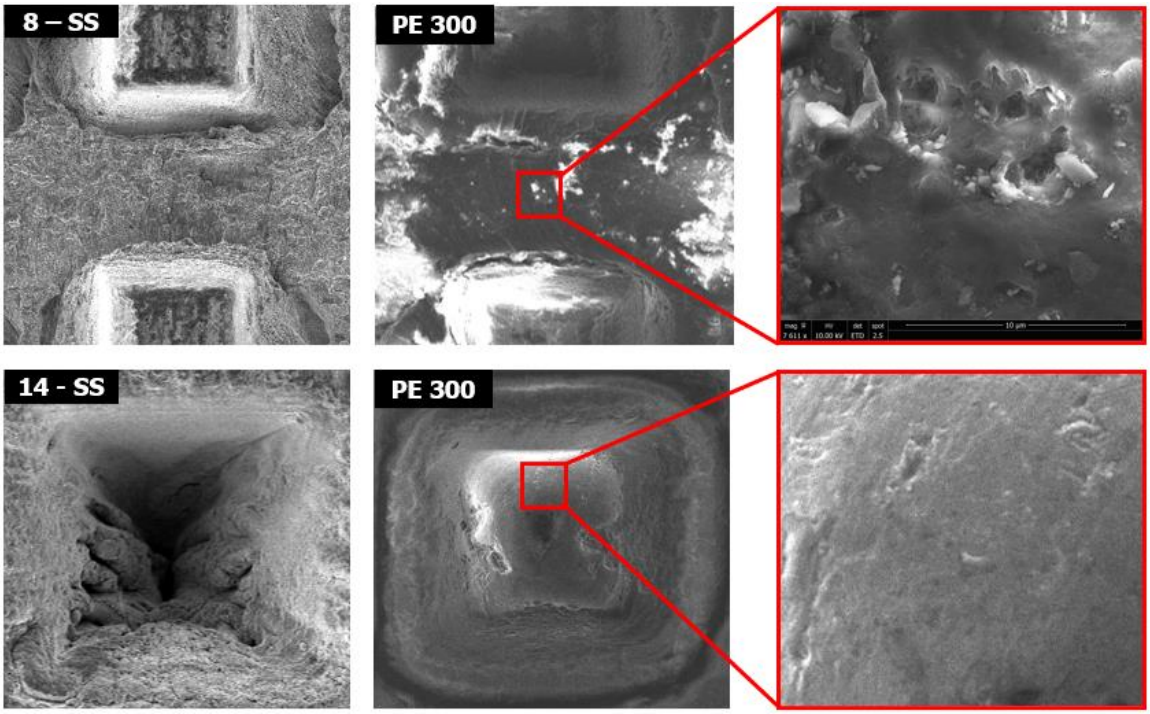

Figure 33. SEM images of nanostructures replicated on PE 300 for 8-SS and 14-SS.

Nanostructures created on 8-SS (pillar structures on the mold) were to a certain degree replicated on PE 300. This means that the polymer completely filled and thus reached the bottom of the cavities. However, no replicated nanostructures were found on the PE 300 replica from 14-SS (holes structures on the mold), and a flat top surface of the polymer pillars was obtained, which let us conclude that in this case the polymer did not reach the bottom of the hole cavities. The reason for this difference likely lies in the nature of the cavities: holes trap air below the penetrating polymer front, while for pillar structures, the air is pushed out between pillars, as explained in the sub-chapter 7.3.2.

Figure 34 exhibits the SEM images of nanostructures created during laser ablation on 8-SS, and their replicas on PP 350 and PE 300.

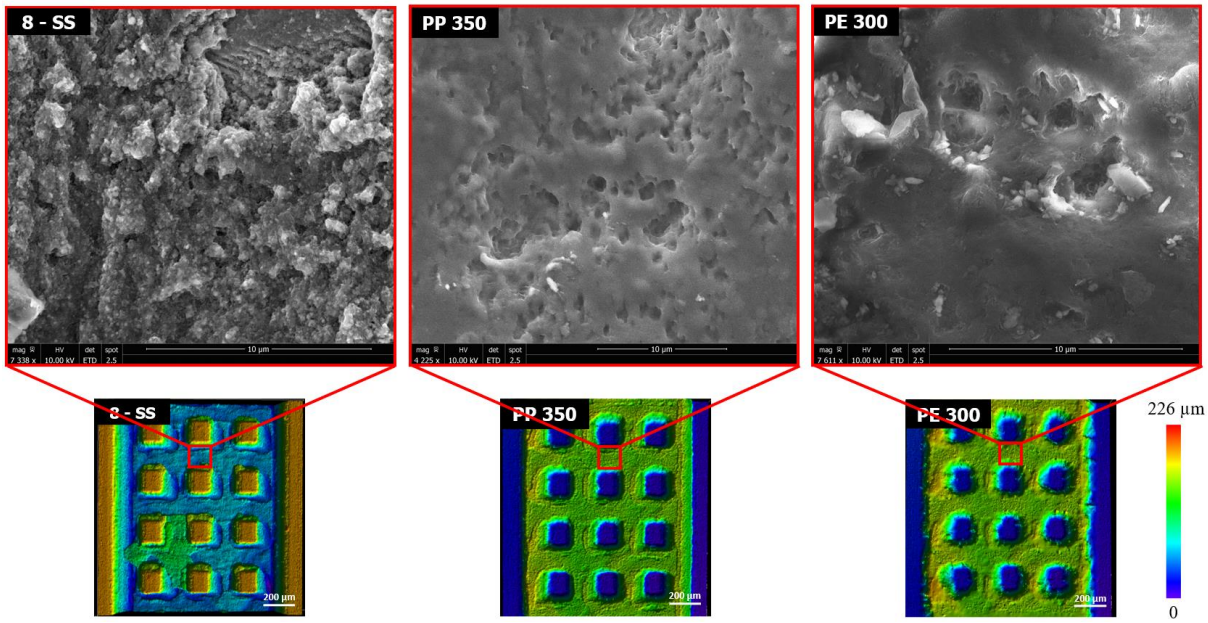

Figure 34. SEM images of nanostructures created during laser ablation on 8 – SS, and their replicas on PP 350 and PE 300.

These results show that PP 350 replicated more faithfully the nanostructures from the mold than the PE 300, which is explained by the considerably lower viscosity of PP.

7.5 Assessment of Polymer Penetration for the Late Cycles

In this sub-chapter, the assessment of polymer penetration of mold pillar structures on PP 350 and PE 150 replicas is presented. Only the pillar structures were considered since as discussed in the sub-chapter 7.3.2, this type of structure allows for better replication than hole

structures due to limited air trapping. Also, pillar structures laser micromachined on the mold translate into hole structures on the polymer, and for the polymer surfaces, the air being trapped in the holes is now beneficial, since it helps the surface to remain in the Cassie-Baxter wetting state, without the water penetrating the cavities.

Table 15 shows the comparison between the *c* values from the SS mold pillar patterns (from Table 14) with their respective PP 350 and PE 150 replicas. As a side note, after injection molding campaign the SS mold had been destroyed in the effort to analyze structures on the side wall of the mold insert, which concerns a postdoc project. Therefore, no analysis could be done in the SS mold after the injection molding campaign, as it would have been desired in hint sight. Yet, assuming that the initial subsequent injection molding cycles result in alike dimensional changes as seen for the hot press molding process, the SS mold *b* values were increased by 16% and the *c* values decreased by 10% from the measurements analyzed before the injection molding campaign, to account for the redeposited particles formed during laser micromachining that are pushed to the bottom of the mold cavities by the molten polymers as described in sub-chapter 6.3. In addition, the aspect ratio values for the mold patterns are crucial to establish the injection molding limitations in terms of polymer flowability into the cavities for different *b* and *c* values laser micromachined on the SS mold.

Table 15. Comparison between the *c* values from the SS mold pillar patterns (from Table 14) with their respective PP 350 and PE 150 replicas. SS mold *b* values were increased by 16% and the *c* values decreased by 10% from the measurements before the injection molding campaign.

Pattern	SS mold			PP 350	PE 150
	c (µm) Average	*b* (µm) Average	Aspect ratio	*c* (µm) Average	*c* (µm) Average
1 - SS	53	44	1.20	53	51 -4%
2 - SS	102	97	1.05	107 +5%	108 +6%
3 - SS	100	154	0.65	113 +13%	113 +13%
4 - SS	84	37	2.27	60 -29%	62 -26%
5 - SS	192	88	2.18	171 -11%	169 -12%
6 - SS	224	118	1.90	204 -9%	209 -7%
7 - SS	57	43	1.33	54 -5%	54 -5%
8 - SS	130	157	0.83	142 +9%	144 +11%
17 - SS	63	35	1.80	71 +13%	63
18 - SS	115	107	1.07	112 -3%	110 -4%
19 - SS	129	170	0.76	135 +5%	137 +6%

To interpret the results from Table 15 some aspects are taken into consideration. For the *c* values on PP 350 and PP 150 that are higher than the respective values on the SS mold, the polymer penetration is considered successful with a perfect polymer replica. As a side note, the increase in height values can be explained by an elastic relaxation of the polymers due to the induced shear stress during demolding (Stormonth-Darling et al. 2016). For the *c* values on PP 350 and PP 150 smaller than the SS mold ones, as long as the difference is not smaller than 5%, the polymer penetration is considered unsuccessful. In other words, if the SS mold has a c = 100 µm and the PP 350 replica c = 95 µm for example, the replication is still considered successful. The 5% consideration is just to account possible human errors while analyzing the dimensions, since any slight change in the lines considered for analysis of the confocal data can alter the final averaged results.

According to Table 15, PP 350 and PE 150 presented very similar polymer penetration inside the mold structure cavities in almost all patterns. One exception can be seen for 17 - SS, where *c* for PE 150 is not as high as for PP 350. For the high aspect ratio patterns (2.27, 2.18 and 1.90 from 4 - SS, 5 - SS and 6 - SS, respectively), both polymers did not reach the bottom of the cavities. For 17 - SS with aspect ratio of 1.80, both polymers reached the bottom of the cavities. In addition, for all the other patterns with aspect ratio < 1.80, a complete polymer penetration in the mold cavities was achieved. So, 1.80 was established as the experimental limit for the aspect ratio ensuring a perfect polymer replica for the tested injection molding parameters. This value was the one used in the thermodynamic optimization codes as the aspect ratio limitation for injection molding, which is presented in the next chapter.

8 COMPUTATIONAL THERMODYNAMIC OPTIMIZATION

The goal of the industry collaboration with IPL Inc. is the production of self-cleaning plastic containers. In the scope if this master thesis the focus was on establishing the framework for this further development. The findings from earlier sections provided relevant limits for theoretically deriving the key dimensions that should lead to optimal hydrophobicity. These dimensions when considering hole structures for H_2O on PE/PP are, minimum *a* value of 6 µm based on the laser line width (ω_{eff}) when using the optimized laser parameters (power of 40 mW with speed of 1 mm/s), minimum *b* value of 50 µm, and maximum aspect ratio (*c*/*a*) value of 1.80 to achieve a complete polymer replica during injection molding. Therefore, the energy concepts as well as the pressure concept as introduced in chapter 2 are taken into consideration.

Before presenting the individual equations considering the energy and pressure concepts for thermodynamic optimization, it is important to understand that the geometrical parameter *a* in the PE/PP on SS cases, is the tunable parameter, which means that it is dictated by the machining process (ω_{eff}), resulting in a boundary condition (6 µm, as shown before). However, *a* in the H_2O on PE/PP cases, is the raised feature dimension, meaning that it is the idealized case that makes for the top surface area. Figure 35 illustrates the transition from holes to pillars (blue arrow) and pillars to holes (green arrow) with squares as the example. In other words, the green arrow indicates when square pillars are laser-micromachined on the mold, translating into square holes on the polymer, and the blue arrow stands for square holes laser-micromachined on the mold, translating into square pillars on the polymer. Also, the white areas indicate the raised features, and the black areas are the depleted ones.

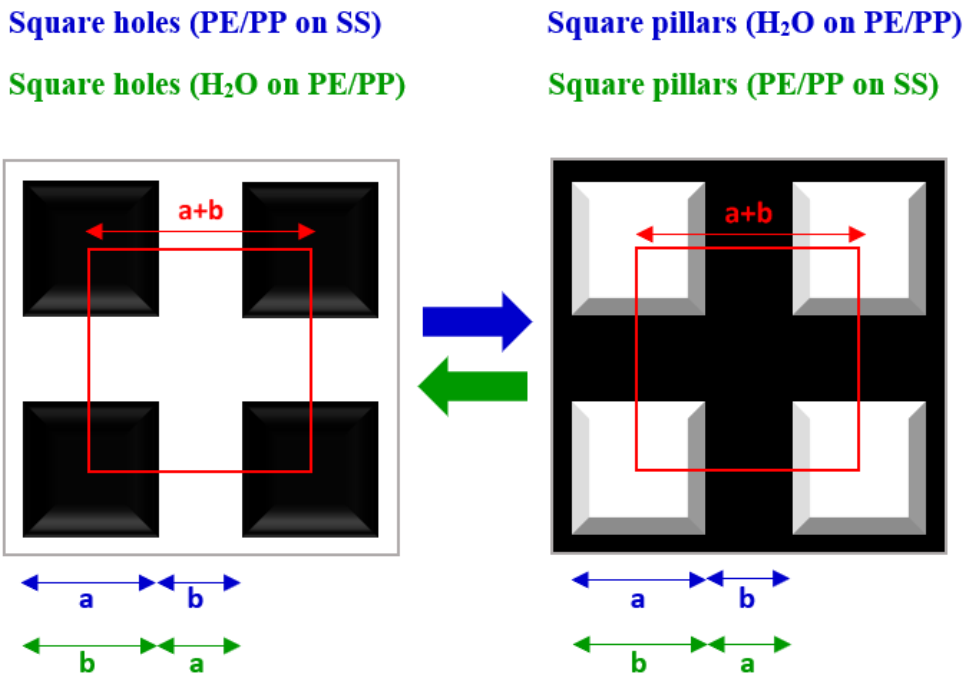

Figure 35. Transition from square holes (PE/PP on SS) to square pillars (H_2O on PE/PP), represented by the color blue in the figure, and the transition from square pillars (PE/PP on SS) to square holes (H_2O on PE/PP), represented by the color green in the image.

Below are the calculated area fractions and free energy for each unit area for the square and hexagonal geometries (pillars and holes) for H_2O on PE/PP when considering the energy concept for thermodynamic optimization. By inverting the dimensions *a* and *b*, the equations are adapted for the PE/PP on SS case.

Square pillars

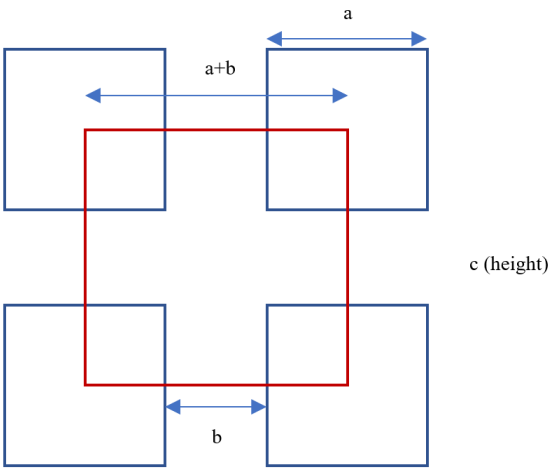

Figure 36. Top view of four square pillars, which outline a unit (red square).

Solid-Air interface

Before formation of the droplet: $A_{sa} = (a+b)^2 + 4ac$ (18)

For complete wetting (Wenzel): $A_{sa} = -(a+b)^2 - 4ac$ (19)

For partial wetting: $A_{sa} = -a^2 - 4ah$ (20)

Solid-Liquid interface

Before formation of the droplet: $A_{sl} = 0$ (21)

For complete wetting (Wenzel): $A_{sl} = 4ac + (a+b)^2$ (22)

For partial wetting: $A_{sl} = a^2 + 4ah$ (23)

Liquid-Air interface

Before formation of the droplet: $A_{la} = 0$ (24)

For complete wetting (Wenzel): $A_{la} = \frac{2(a+b)^2}{(1+cos\theta)}$ (25)

For partial wetting: $A_{la} = \frac{2(a+b)^2}{(1+cos\theta)} + b(2a+b)$ (26)

The free energy of a unit is then calculated according to the Equation 16, and the calculated area values for the square unit:

Cassie-Baxter: $G_{cassie} = \gamma_{la}(2ab + b^2 + \frac{2(a+b)^2}{(1+cos\theta_c)} - a^2 cos\theta_y)$ (27)

Wenzel: $G_{wenzel} = \gamma_{la}\left(\frac{2(a+b)^2}{(1+cos\theta_w)} - ((a+b)^2 + 4ac)cos\theta_y\right)$ (28)

with:

Wenzel: $cos\theta_w = r\, cos\theta_y = \left(\frac{4ac}{(a+b)^2} + 1\right) cos\theta_y$ (29)

Cassie-Baxter: $cos\theta_c = f_1\left(cos\theta_y + 1\right) - 1 = \frac{a^2}{(a+b)^2}\left(cos\theta_y + 1\right) - 1$ (30)

Square holes

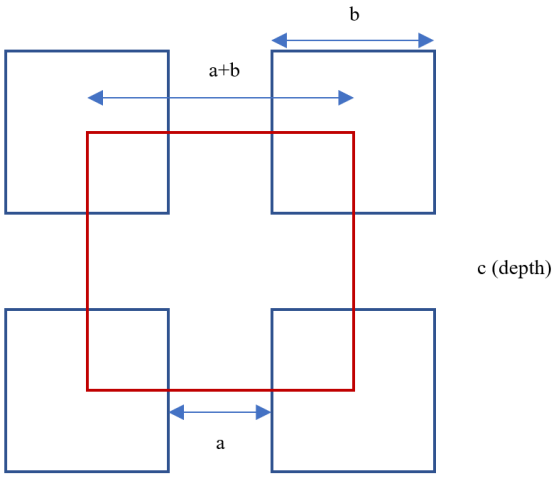

Figure 37. Top view of four square holes, which outline a unit (red square).

Solid-Air interface

Before formation of the droplet: $A_{sa} = (b+a)^2 + 4bc$ (31)

For complete wetting (Wenzel): $A_{sa} = -(b+a)^2 - 4bc$ (32)

For partial wetting: $A_{sa} = -a(2b+a) - 4bh$ (33)

Solid-Liquid interface

Before formation of the droplet: $A_{sl} = 0$ (34)

For complete wetting (Wenzel): $A_{sl} = (b+a)^2 + 4bc$ (35)

For partial wetting: $A_{sl} = a(2b+a) + 4bh$ (36)

Liquid-Air interface

Before formation of the droplet: $A_{la} = 0$ (37)

For complete wetting (Wenzel): $A_{la} = \frac{2(b+a)^2}{(1+cos\theta)}$ (38)

For partial wetting: $A_{la} = \frac{2(b+a)^2}{(1+cos\theta)} + b^2$ (39)

The free energy of a unit is then calculated according to the Equation 16, and the calculated area values for the square unit:

Cassie-Baxter: $$G_{cassie} = \gamma_{la}\left(\frac{2(b+a)^2}{(1+cos\theta_c)} + b^2 - \big(a(2b+a)\big)cos\theta_y\right) \quad (40)$$

Wenzel: $$G_{wenzel} = \gamma_{la}\left(\frac{2(b+a)^2}{(1+cos\theta_w)} - ((b+a)^2 + 4bc)cos\theta_y\right) \quad (41)$$

with:

Wenzel: $$cos\theta_w = r\,cos\theta_y = (\frac{4bc}{(b+a)^2} + 1)cos\theta_y \quad (42)$$

Cassie-Baxter: $$cos\theta_c = f_1\big(cos\theta_y + 1\big) - 1 = \frac{a(2b+a)}{(b+a)^2}\big(cos\theta_y + 1\big) - 1 \quad (43)$$

Hexagonal pillars

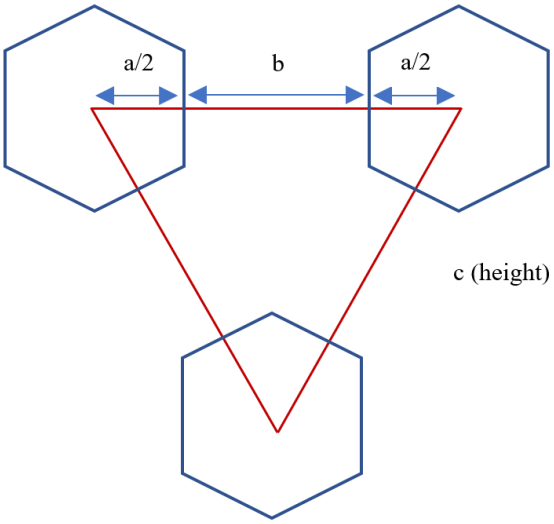

Figure 38. Top view of three hexagonal pillars, which outline a unit (red triangle).

Solid-Air interface

Before formation of the droplet: $$A_{sa} = \frac{\sqrt{3}(a+b)^2}{4} + \frac{3ac}{\tan 60°} \quad (44)$$

For complete wetting (Wenzel): $$A_{sa} = -\frac{\sqrt{3}(a+b)^2}{4} - \frac{3ac}{\tan 60°} \quad (45)$$

For partial wetting: $$A_{sa} = -\frac{3\sqrt{3}a^2}{4(\tan 60°)^2} - \frac{3ah}{\tan 60°} \quad (46)$$

Solid-Liquid interface

Before formation of the droplet: $$A_{sl} = 0 \quad (47)$$

For complete wetting (Wenzel): $$A_{sl} = \frac{\sqrt{3}(a+b)^2}{4} + \frac{3ac}{\tan 60°} \quad (48)$$

For partial wetting: $$A_{sl} = \frac{3\sqrt{3}a^2}{4(\tan 60°)^2} + \frac{3ah}{\tan 60°} \quad (49)$$

Liquid-Air interface

Before formation of the droplet: $$A_{la} = 0 \quad (50)$$

For complete wetting (Wenzel): $$A_{la} = \frac{\sqrt{3}(a+b)^2}{2(1+cos\theta)} \quad (51)$$

For partial wetting: $$A_{la} = \frac{\sqrt{3}(a+b)^2}{2(1+cos\theta)} + \frac{\sqrt{3}(a+b)^2}{4} - \frac{3\sqrt{3}a^2}{4(\tan 60°)^2} \quad (52)$$

The free energy of a unit is then calculated according to the Equation 16, and the calculated area values for the hexagonal unit:

Cassie-Baxter $$G_{cassie} = \gamma_{la}\left(\frac{\sqrt{3}(a+b)^2}{2(1+cos\theta_c)} + \frac{\sqrt{3}(a+b)^2}{4} - \frac{3\sqrt{3}a^2}{4(\tan 60°)^2} - \frac{3\sqrt{3}a^2}{4(\tan 60°)^2}cos\theta_y\right) \quad (53)$$

Wenzel: $$G_{wenzel} = \gamma_{la}\left(\frac{\sqrt{3}(a+b)^2}{2(1+cos\theta_w)} - \left(\frac{\sqrt{3}(a+b)^2}{4} + \frac{3ac}{\tan 60°}\right)cos\theta_y\right) \quad (54)$$

with:

Wenzel: $$cos\theta_w = r\,cos\theta_y = \left(\frac{\frac{\sqrt{3}(a+b)^2}{4} + \frac{3ac}{\tan 60°}}{\frac{\sqrt{3}(a+b)^2}{4}}\right)cos\theta_y \quad (55)$$

Cassie-Baxter: $$cos\theta_c = f_1(cos\theta_y + 1) - 1 = \frac{3a^2}{(\tan 60°)^2(a+b)^2}(cos\theta_y + 1) - 1 \quad (56)$$

Hexagonal holes

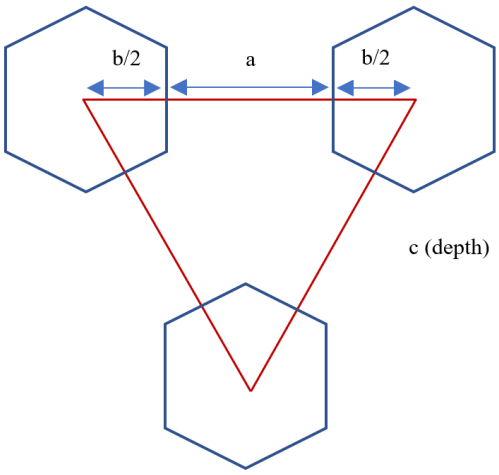

Figure 39. Top view of three hexagonal holes, which outline a unit (red triangle).

Solid-Air interface

Before formation of the droplet: $$A_{sa} = \frac{\sqrt{3}(b+a)^2}{4} + \frac{3bc}{\tan 60°} \quad (57)$$

For complete wetting (Wenzel): $$A_{sa} = -\frac{\sqrt{3}(b+a)^2}{4} - \frac{3bc}{\tan 60°} \quad (58)$$

For partial wetting: $$A_{sa} = -\left(\frac{\sqrt{3}(b+a)^2}{4} - \frac{3\sqrt{3}b^2}{4(\tan 60°)^2}\right) - \frac{3bh}{\tan 60°} \quad (59)$$

Solid-Liquid interface

Before formation of the droplet: $$A_{sl} = 0 \quad (60)$$

For complete wetting (Wenzel): $$A_{sl} = \frac{\sqrt{3}(b+a)^2}{4} + \frac{3bc}{\tan 60°} \quad (61)$$

For partial wetting: $$A_{sl} = \left(\frac{\sqrt{3}(b+a)^2}{4} - \frac{3\sqrt{3}b^2}{4(\tan 60°)^2}\right) + \frac{3bh}{\tan 60°} \quad (62)$$

Liquid-Air interface

Before formation of the droplet: $$A_{la} = 0 \quad (63)$$

For complete wetting (Wenzel): $$A_{la} = \frac{\sqrt{3}(b+a)^2}{2(1+cos\theta)} \quad (64)$$

For partial wetting: $$A_{la} = \frac{\sqrt{3}(b+a)^2}{2(1+cos\theta)} + \frac{3\sqrt{3}b^2}{4(\tan 60°)^2} \quad (65)$$

The free energy of a unit is then calculated according to the Equation 16, and the calculated area values for the hexagonal unit:

Cassie-Baxter: $$G_{cassie} = \gamma_{la}\left(\frac{\sqrt{3}(b+a)^2}{2(1+cos\theta_c)} + \frac{3\sqrt{3}b^2}{4(\tan 60°)^2} - \left(\frac{\sqrt{3}(b+a)^2}{4} - \frac{3\sqrt{3}b^2}{4(\tan 60°)^2}\right)cos\theta_y\right) \quad (66)$$

Wenzel: $$G_{wenzel} = \gamma_{la}\left(\frac{\sqrt{3}(b+a)^2}{2(1+cos\theta_w)} - \left(\frac{\sqrt{3}(b+a)^2}{4} + \frac{3bc}{\tan 60°}\right)cos\theta_y\right) \quad (67)$$

with:

Wenzel: $$cos\theta_w = r\,cos\theta_y = \left(\frac{\frac{\sqrt{3}(b+a)^2}{4} + \frac{3bc}{\tan 60°}}{\frac{\sqrt{3}(b+a)^2}{4}}\right)cos\theta_y \quad (68)$$

Cassie-Baxter: $$cos\theta_c = f_1\left(cos\theta_y + 1\right) - 1 = \left(\frac{\frac{\sqrt{3}(b+a)^2}{4} - \frac{3\sqrt{3}b^2}{4(\tan 60°)^2}}{\frac{\sqrt{3}(b+a)^2}{4}}\right)\left(cos\theta_y + 1\right) - 1 \quad (69)$$

Below are the maximum hydraulic pressure equations, from Equation 17, adapted for square and hexagonal geometries (pillars and holes) when considering the pressure concept for thermodynamic optimization.

Square pillars:
$$P_c = \frac{\gamma_{la}\left(\frac{a^2}{(a+b)^2}\right)cos\theta_y}{\left(1-\left(\frac{a^2}{(a+b)^2}\right)\right)\left(\frac{a}{4}\right)} \quad (70)$$

Square holes:
$$P_c = \frac{\gamma_{la}\left(\frac{3a^2}{(\tan 60°)^2(a+b)^2}\right)cos\theta_y}{\left(1-\left(\frac{3a^2}{(\tan 60°)^2(a+b)^2}\right)\right)\left(\frac{\sqrt{3}a}{4(\tan 60°)}\right)} \quad (71)$$

Hexagonal pillars:
$$P_c = \frac{\gamma_{la}\left(\frac{3a^2}{(\tan 60°)^2(a+b)^2}\right)cos\theta_y}{\left(1-\left(\frac{3a^2}{(\tan 60°)^2(a+b)^2}\right)\right)\left(\frac{\sqrt{3}a}{4(\tan 60°)}\right)} \quad (72)$$

Hexagonal holes:
$$P_c = \frac{\gamma_{la}\left(\frac{\frac{\sqrt{3}(b+a)^2}{4}-\frac{3\sqrt{3}b^2}{4(\tan 60°)^2}}{\frac{\sqrt{3}(b+a)^2}{4}}\right)cos\theta_y}{\left(1-\left(\frac{\frac{\sqrt{3}(b+a)^2}{4}-\frac{3\sqrt{3}b^2}{4(\tan 60°)^2}}{\frac{\sqrt{3}(b+a)^2}{4}}\right)\right)\left(\frac{\left(\frac{\sqrt{3}(b+a)^2}{4}-\frac{3\sqrt{3}b^2}{4(\tan 60°)^2}\right)}{\frac{3b}{\tan 60°}+3a}\right)} \quad (73)$$

The ΔG_{max} ($G_{wenzel} - G_{cassie}$), Pc and θ_c values from the equations derived above for square and hexagonal holes, H_2O on PE, were calculated by algorithms, that were developed on the software Python, in a selected range for the dimensions *a*, *b*, and *c*. The respective ΔG_{max} and Pc for square and hexagonal pillars, PE on SS, for the dimensions were also calculated in the same models. These models basically provide a list of all combinations in the selected range for the dimensions *a*, *b*, and *c* that fulfill the boundary conditions from the laser micromachining and injection molding constraints. In the end, the selected *a*, *b*, and *c* to be laser-micromachined and consequently imprinted on the PE are the ones that present the highest ΔG_{max}, Pc and/or θ_c for the hole structures, H_2O on PE, with the minimum ΔG_{max} and/or Pc for the pillar structures, PE on SS. It is important to notice that the thermodynamic optimization calculations considering PP were not carried out in this study, but it will be in a near future work.

The $\gamma_{la} = 0.0728$ N/m for H_2O at 20 ºC and $\gamma_{la} = 0.02373$ N/m for PE at 230 ºC, calculated by the equation $\gamma_{la}(PE) = 35.7 - 0.057(T - 20)$, experimentally derived by Wu (1969) using the pendent drop method, which T is the temperature of the PE (ºC), are the

values utilized in the models. Table 16 summarizes the range used for the dimensions *a*, *b* and *c* determined based on the laser constraints and the maximum aspect ratio from the injection molding constraint. The interval for the dimensions were set as 5 µm, i.e., if the minimum value of the dimension *a* is set as 6 µm, the second value considered in the calculation is 11 µm, then 16 µm, and so on, until the maximum value set is achieved. The interval of 5 µm was chosen since controlling the variables with more precision than that with the current laser settings is not feasible and unnecessary. The maximum values for the dimensions *a* and *b* were set as 150 µm and *c* was set as 270 µm. For the dimension *a*, it is expected that the larger its value is, while maintaining the other parameters constant, the easier will be for the water droplets to penetrate the cavities, i.e., the Wenzel wetting state will prevail. Similarly, for the dimension *b*, it is expected that the larger its value is, while maintaining the other parameters constant, the higher the solid-liquid contact area will be, which decreases the hydrophobicity of the surface. That is why set large values for these dimensions are unnecessary, and therefore 150 µm is recommended as a reasonable maximum value for the dimensions *a*, and *b*. However, the dimension *c* could be set relatively unlimited, but it is limited by the aspect ratio constraint from injection molding, thus its maximum value was set as 270 µm, which is the maximum *b* value multiplied by 1.80 from the aspect ratio constraint.

Table 16. Summary of the ranges used for the dimensions a, b and c determined based on the laser constraints and the maximum aspect ratio from the injection molding constraint.

		Laser Constraints			**Injection Molding Constraint**
Geometry and type	Dimension	Minimum value (µm)	Maximum value (µm)	Geometry and type	Maximum Aspect Ratio (c/b) value
Square Holes (H2O on PE)	*a*	6	150	Square Pillars (PE on SS)	1.8
	b	50			
	c	1	270		
Hexagon Holes (H2O on PE)	*a*	6	150	Hexagon Pillars (PE on SS)	
	b	50			
	c	1	270		

Along with the constraints from the laser and injection molding, two more boundary conditions were used in the codes. Only the combination of dimensions that results in $\Delta G_{max} > 0$ and $\theta_c \geq 100°$ for H_2O on PE were investigated. The first is to guarantee that the Cassie-Baxter wetting will prevail in the final PE part. The second, the minimum θ_c was

set as 100° instead of 150° because the model does not account for the presence of nanostructures in the SS, imprinting on PE, which in the end enhances the hydrophobicity of the sample. So, it is expected that the experimental value of θ_c will be always higher than the theoretical one. However, at present, it is unknown without experimentation if a combination that theoretically yields in, e.g., θ_c = 100º, will experimentally achieve superhydrophobicity. For the *Pc*, no restrictions were inputted.

After all the boundary conditions were applied, the code provided a list of all possible combinations of *a*, *b*, and *c* that can fulfill the respective requirements. From all the results, two combinations were chosen for each geometry. First, the one that provided the highest *Pc* for H_2O on PE. Among the possibilities with equal highest *Pc*, then the one with highest ΔG_{max} was chosen. The second combination is the one that had the highest θ_c for H_2O on PE. Between the results with equal highest θ_c, the one with highest *Pc* was selected. Table 17 shows the results.

Due to the laser and injection molding limitations, there was no combination that provided θ_c > 104º for H_2O on PE for both geometries. Interestingly the dimensions found for square and hexagonal holes for H_2O on PE are equal in both scenarios, also presenting equal values of *Pc* for PE on SS. When comparing the geometries, square holes presented higher ΔG_{max}, lower *Pc* and equal θ_c values than hexagonal holes for H_2O on PE. For the different θ_y for PE on SS, it can be noticed that by decreasing its value, both ΔG_{max} and *Pc* also decreases, and when $\theta_y < 90°$ all the *Pc* values are negative. Negative values of ΔG_{max} and *Pc* for PE on SS means that the polymer will wet the cavities without any induced pressure. These results will be experimentally tested in a near future work.

By improving the limitation values of laser micromachining and injection molding, better results of θ_c, *Pc* and ΔG_{max} can be achieved. Table 18 shows the new hypothetical results if the minimum value used for *b* is 30 µm instead of 50 µm for the laser micromachining, and 3.0 of aspect ratio instead of 1.8 for injection molding, when considering the $\theta_y = 92º$ for PE on SS.

As it can be seen, iteratively improving the constraints results in new combinations of higher θ_c, *Pc* and ΔG_{max} to direct laser machining and the subsequent molding strategies. With the new hypothetical constrains, the new maximum θ_c is increased from 104º to 110º in both geometries, and the *Pc* and ΔG_{max} are increased substantially. So, it is worth to improve the laser constraints by, e.g., first, using lens with shorter focal distance (< 25.4 mm) so a smaller beam diameter can be achieved. Second, using a top-hat beam, which means that the

sloped tails of the beam increase in slope and thus a side angle for machining of 87º can be achieved (Gosh et al. 2018). The top-hat beam is obtained by a Fourier transform based filter that converts a Gaussian beam shape into a flat-top profile to better shape pillar structures, especially the ones with width < 50 µm, without distorting the geometry. At last, improving the injection molding constraint through, for example, testing higher injection pressures, injection rates, and mold temperature, so that higher aspect ratio values can be achieved.

In the context of this thesis, it was not possible to laser micromachine surface patterns following the recommended settings from the theoretical analysis due to COVID-19 related interruptions in the laboratory, and significantly delayed delivery and installation of a novel laser system. Thus, the comparison of the predicted contact angles for specific feature dimensions and geometry, to actual measured values on mold substrates will be subject of future work.

Table 17. Optimized dimensions of a, b, and c for square and hexagonal holes (H_2O on PE), with the current laser and injection molding constraints.

												Θy = 113°		Θy = 92°		Θy = 70°	
Geometry and type	**Combination**	**a (µm)**	**b (µm)**	**c (µm)**	**ΔGmax (µJ)**	**Θc (°)**	**Pc (Pa)**	**Geometry and type**	**a (µm)**	**b (µm)**	**c (µm)**	**ΔGmax (µJ)**	**Pc (Pa)**	**ΔGmax (µJ)**	**Pc (Pa)**	**ΔGmax (µJ)**	**Pc (Pa)**
Square Holes (H2O on PE)	Highest Pc, then ΔGmax	111	50	196	0.000339	100	1634	Square Pillars (PE on SS)	50	111	196	0.046054	79	-0.012372	7	-0.009907	-69
	Highest Θc, then Pc	96	65	171	0.000006	104	967		65	96	171	1.217921	111	-0.006922	10	-0.006038	-97
Hexagon Holes (H2O on PE)	Highest Pc, then ΔGmax	111	50	196	0.000147	100	2459	Hexagon Pillars (PE on SS)	50	111	196	0.019942	79	-0.005357	7	-0.00429	-69
	Highest Θc, then Pc	96	65	171	0.000003	104	1389		65	96	171	0.527375	111	-0.002997	10	-0.002614	-97

Table 18. Hypothetical optimized dimensions of a, b, and c for square and hexagonal holes (H_2O on PE), if the minimum value used for the dimensions are 30 µm for the laser micromachining, and 3 of aspect ratio for injection molding.

												Θy = 92°	
Geometry and type	**Combination**	**a (µm)**	**b (µm)**	**c (µm)**	**ΔGmax (µJ)**	**Θc (°)**	**Pc (Pa)**	**Geometry and type**	**a (µm)**	**b (µm)**	**c (µm)**	**ΔGmax (µJ)**	**Pc (Pa)**
Square Holes (H2O on PE)	Highest Pc, then ΔGmax	66	30	196	0.000404	100	2707	Square Pillars (PE on SS)	30	66	196	-0.004313	12
	Highest Θc, then Pc	71	80	211	0.000018	110	599		80	71	211	-0.003059	16
Hexagon Holes (H2O on PE)	Highest Pc, then ΔGmax	66	30	196	0.000175	100	4070	Hexagon Pillars (PE on SS)	30	66	196	-0.001867	12
	Highest Θc, then Pc	71	80	211	0.000008	110	805		80	71	211	-0.001324	16

9 CONCLUSION

Hierarchical structures were fabricated using a pulsed femtosecond laser beam on a SS mold with the inverse of the desired pattern for the polymer replica. Then, the laser machined mold was tested in a laboratory hot press and in an industrial injection molding process, and polymer penetration into mold features and shape replication of micro and nanostructures were investigated. We have demonstrated that hot press experiments can be adjusted to reliably represent injection molding. The optimum laser settings to create well-shaped structures of square and hexagonal geometry with different *a*, *b* and *c* are 40 mW of power with 1 mm/s of scanning velocity, when considering the use of a 25.4 mm 25.4 mm bi-convex focusing lens and 90% overlap of lines for a 1 kHz femtosecond laser with 800 nm of wavelength. Additionally, the minimal dimension for *b* of pillars laser micromachined on the mold achieved with the current laser settings, so the shape of the pillar structures remain unaltered, was 50 μm.

From the injection molding campaign, we realized that a perfect replica was achieve for pillars on the mold translating into holes on the polymer, because the air is not trapped inside the cavities but escapes sideways, allowing the polymers to reach the bottom of the cavities, and consequently also imprint the nanostructures. The maximum aspect ratio achieved in these tests to allow a complete polymer penetration into the mold structures was 1.8. Furthermore, PP showed better nanostructures replication than PE owing to its lower viscosity, and larger structures laser-machined on the mold surface presented the most faithful replicas, which is explained by lower frictional resistance to the polymer flow. At last, no significant difference was observed between the replication quality of square and hexagonal features.

As a basis of future research that will be focused on the laser machining and molding of superhydrophobic polymer pieces, a computational model based on thermodynamics, and kinetics was developed to predict which geometrical parameters (*a*, *b*, and *c*) for the square and hexagonal geometries (pillars translating into holes) should be chosen in the laser machining process to provide the best results in terms of superhydrophocity for the polymer replicate, while considering the laser and injection molding established limitations. Exemplarily the analytical code was run for PE and the limitations derived for the laser system used in this particular research and it was found that there was no combination that provided $\theta_c > 104^o$ for H_2O on PE for both geometries. Square holes presented higher ΔG_{max},

lower Pc and equal θ_c values than hexagonal holes for the same dimensions for H_2O on PE. It is expected that by improving both laser micromachining and injection molding constraints, better results of θ_c, Pc and ΔG_{max} can be achieved.

10 ORIGINAL CONTRIBUTIONS

The original contributions of this master's thesis are as follows:

1. Laser micromachining settings to ablate well-shaped geometries up to $a = b = 50$ µm were established;
2. A laboratory hot press procedure was developed to achieve the most faithful polymer replicas, also proving that it can be used to mimic industrial injection molding results;
3. We have laser-micromachined square and hexagonal geometry, both in pillars and holes, and proven that pillars on the mold translating into holes on the polymer presented more faithful replicas, with nanostructures transfer from the mold to the polymer. Also, square, and hexagonal geometry presented similar replicas in terms of polymers flowability;
4. A computation model based on thermodynamic and kinetics considerations was developed to predict which dimensions (*a*, *b*, and *c*) would present the best superhydrophobic properties for pillars geometries translating into holes.

11 FUTURE WORK

Future work will focus to improve the laser micromachining and injection molding constraints. For the first, producing pillar structures on the SS mold with $a < 50$ μm is the main goal. For that it is worth using a smaller focusing lens (< 25.4 mm), so a smaller beam diameter can be achieved at focus, and consequently smaller structures can be fabricated. In addition, a top-hat beam, instead of a Gaussian beam, should be tested, also in an attempt to achieve well-shaped pillar structures with $a < 50$ μm. Finally, in an effort to reach aspect ratio values higher than 1.8, different injection molding settings should be tested and compared for different aspect ratio patterns, e.g., higher injection pressure, lower screw rotational speed, slower cooling time, etc.

The Biomimetic surface engineering laboratory has recently received a new laser system with 1 MHz of frequency, which allows surface processing at much higher rates. That is beneficial since one of the laser constraints is laser ablation time, and that can be drastically reduced, especially for laser micromachining patterns of larger area necessary for goniometry analysis. As a consequence, it will become possible to laser micromachine various dimensions derived from the thermodynamic optimization model described in this work, test them in the goniometer and compare the experimental values with the theoretical ones. If superhydrophobicity is not achieved, the main focus will be to improve the constraints for both laser micromachining and injection molding as abovementioned.

12 REFERENCES

ACME. “HDPE and PP Plastic: What’s the Difference?”. AcmePlastics, 07 Jan 2019, https://www.acmeplastics.com/content/hdpe-and-pp-plastic-whats-the-difference/

Ahmmed, K. M. T., et al. (2014). “Fabrication of micro/nano structures on metals by femtosecond laser micromachining.” *Micromachines 5*, 1219-1253.

Ahmmed, K. M. T., and Kietzig, A.-M. (2016). “Drag reduction on laser-patterned hierarchical superhydrophobic surfaces.” *Soft Matter 12*, 4912–4922.

Ahmmed, K. M. T., et al. (2015). "Introducing a New Optimization Tool for Femtosecond Laser-Induced Surface Texturing on Titanium, Stainless Steel, Aluminum and Copper." *OLEN 66*, 258-268.

Al-Rumaihi, A., et al. (2020). "Environmental Impact Assessment of Food Waste Management Using Two Composting Techniques." *Sustainability, 12*(4).

Anisimov, S. I., et al. (1974). “Electron emission from metal surfaces exposed to ultrashort laser pulses.” *Landau Institute of Theoretical Physics, 66*, 776-781.

Anisimov, S. I., et al. (2008). “Interaction of short laser pulses with metals at moderate intensities.” *Applied Physics A, 92*(4), 939-943.

AZoM. “P20 Tool Steel – Low-Carbon Mold Steel UNS T51620”. AZO Materials, 17 Dec 2012, https://www.azom.com/article.aspx?ArticleID=6239.

Bartenev, G. M. and Lavrentev, V. V. (1981). “*Friction and Wear of Polymers*.” Elsevier, Amsterdam.

Barthlott, W. and Neinhuis, C. (1997). “Purity of the sacred lotus or escape from contamination in biological surfaces.” *Planta 202*, 1-8.

Bhushan, B. (2019). “Lessons from nature for green science and technology: an overview and bioinspired superliquiphobic/philic surfaces.” *Phil. Trans. R. Soc. A 377*, 20180274.

Briscoe, B. J. (1986). “*Friction and Wear of Polymer Composites*.” Ed. F. Klaus (Elsevier, Amsterdam), p. 25.

Bouchard, F., et al. (2021). "Hierarchical Microtextures Embossed on PET from Laser-Patterned Stamps." *Materials (Basel) 14*(7).

Cassie, A. B. D. (1948). “Contact angles”. *Discussions of the Faraday Society 3*, 11-16.

Cassie, A. B. D., and Baxter, S. (1944). "Wettability of Porous Surfaces." *Transactions of the Faraday Society 40(0)*, 546-551.

Cech, J. and Taboryski, R. (2012). “Stability of FDTS monolayer coating on aluminum injection molding tools.” *Applied Surface Science 259*, 538-541.

Chichkov, B.N., et al. (1996). “Femtosecond, picosecond, and nanosecond laser ablation of solids.” *Appl. Phys. A, 63*, 109–115.

Choi, S. Y., et al. (2016). "Material- and feature-dependent effects on cell adhesion to micro injection moulded medical polymers." *Colloids Surf. B. Biointerfaces 145*, 46-54.

Colin, X. and Verdu, J. (2006). “Polymer degradation during processing.” *C. R. Chimie 9*, 1380-1395.

de Gennes, P. G. (1985). "Wetting: Statics and Dynamics." *Reviews of Modern Physics 57(3)*, 827-863.

Eichstädt, J., et al. (2013). "Determination of Irradiation Parameters for Laser-Induced Periodic Surface Structures." *Applied Surface Science 264*, 79-87.

Erpul, G., et al. (2002). “Raindrop-induced and wind-driven soil particle transport.” *Catena 47*, 227-243.

Fadeeva, E., et al. (2011). “Bacterial retention on superhydrophobic titanium surfaces fabricated by femtosecond laser ablation.” *Langmuir 27*, 3012-9.

Gamaly, E. G., et al. (2002). “Ablation of solids by femtosecond lasers: Ablation mechanism and ablation thresholds for metals and dielectrics.” *Phys. Plasmas, 9*, 949–957.

Geyer, R., et al. (2017). “Production, use, and fate of all plastics ever made”. *Science Advances, 3*(7) e1700782.

Gong, D., et al. (2015). “Thermal stability of micro-nano structures and superhydrophobicity of polytetrafluoroethylene films formed by hot embossing via a picosecond laser ablated template.” *Applied Surface Science 331,* 437-443.

Gosh, A., et al. (2018). “Layer-by-layer combination of laser powder bed fusion (LPBF) and femtosecond laser surface machining of fabricated stainless steel components.” *Journal of Manufacturing Processes 35*, 327-336.

Griffiths, C. A., et al (2013). “A novel texturing of micro injection moulding tools by applying an amorphous hydrogenated carbon coating.” *Surface and Coating Technology 235*, 1-9.

Groenendijk, M. (2008). “Fabrication of Super Hydrophobic Surfaces by fs Laser Pulses.” *Laser Technik Journal 5*, 44-47.

Guan, W.-S., et al. (2015). "Tuning 3D topography on biomimetic surface for efficient self-cleaning and microfluidic manipulation." *Journal of Micromechanics and Microengineering 25*(3).

Guan, W.-S., et al. (2013). "Topographic design and application of hierarchical polymer surfaces replicated by microinjection compression molding." *Journal of Micromechanics and Microengineering 23*(10).

Gudde, J., et al. (1998). “Damage threshold dependence on electron-phonon coupling in Au and Ni films.” *Appl. Surf. Sci., 127,* 40–45.

Guo, Y., et al. (2006). “Study of the demolding process – implications for thermal stress, adhesion and friction control.” *J. Micromech. Microeng. 17*, 9-19.

Heckele, M., et al. (1998). “Hot embossing - The molding technique for plastic microstructures.” *Microsystem Technologies 4***,** 122–124.

Hensel, R., et al. (2013). "Wetting resistance at its topographical limit: the benefit of mushroom and serif T structures." *Langmuir 29*(4), 1100-1112.

Herminghaus, S. (2000). “Roughness-induced non-wetting”. *Europhysics Letters 52*, 165-170.

Hobæk, T. C. et al. (2015). “Hydrogen silsesquioxane mold coating for improved replication of nanopatterns by injection molding.” *Journal of Micromechanics and Microengineering 25*, 035018.

Höflinger, G. (2013). “Brief Introduction to Coating Technology for Electron Microscopy”. Leica Microsystems, 28 Aug 2013, https://www.leica-microsystems.com/science-lab/brief-introduction-to-coating-technology-for-electron-microscopy/#:~:text=Coating%20of%20samples%20is%20required,topographic%20examination%20in%20the%20SEM%20.

Hong, S., et al. (2015). "Correlation between thermal contact resistance and filling behavior of a polymer melt into multiscale cavities in injection molding." *International Journal of Heat and Mass Transfer 87*, 222-236.

Jee, Y., et al. (1988). “Laser-induced damage on single-crystal metal-surfaces.” *J. Opt. Soc. Am. B Opt. Phys., 5*, 648–659.

Johnson, R. E., and Dettre, R. H. (1964). “Contact Angle Hysteresis. Contact Angle, Wettability, and Adhesion.” *American Chemical Society (43)*, 112-135.

Karthikeyan, et al. (2018). “Boiling heat transfer enhancement with stable nanofluids and laser textured copper surfaces”. *International Journal of Heat and Mass Transfer 126B*, 287–296.

Kietzig, A.-M. (2011). Comments on “An Essay on Contact Angle Measurements – An illustration of the respective influence of droplet deposition and measurement parameters”. *Plasma Processes and Polymers 8*, 11, 1003.

Koch, K., et al. (2008). “Diversity of structure, morphology, and wetting of plant surfaces.” *Soft Matter 4*, 1943–1963.

Krishnan, A., et al. (2005). "An evaluation of methods for contact angle measurement." *Colloids Surf B Biointerfaces 43(2)*, 95-98.

Kruger, J., and Kautek, W. (2004). “Ultrashort pulse laser interaction with dielectrics and polymers.” *Adv. Polym. Sci., 168*, 247–289.

Law, K. Y. (2014). "Definitions for Hydrophilicity, Hydrophobicity, and Superhydrophobicity: Getting the Basics Right." *J Phys Chem Lett 5(4)*, 686-688.

Lin Feng, Y. Z., et al. (2008). “Petal Effect: A superhydrophobic State with High Adhesive Force.” *Langmuir, 24*, 4114-4119.

Ling, E., et al. (2016). “Reducing ice adhesion on non-smooth metallic surfaces: wettability and topography effects.” *ACS Applied Materials & Interfaces 8*, 8789−8800.

Liu, X., et al. (1997). “Laser ablation and micromachining with ultrashort laser pulses.” *IEEE J. Quantum Electron. 33*, 1706–1716.

Luna, S. M., et al. (2014). "Dispersing hydrophilic nanoparticles in hydrophobic polymers: HDPE/ZnO nanocomposites by a novel template-based approach." *Express Polymer Letters 8*(5), 362-372.

Lutey, A. H. A., et al. (2021). "Insight into replication effectiveness of laser-textured micro and nanoscale morphology by injection molding." *Journal of Manufacturing Processes 65*, 445-454.

Mannion, P.T., et al. (2004). “The effect of damage accumulation behaviour on ablation thresholds and damage morphology in ultrafast laser micro-machining of common metals in air.” *Appl. Surf. Sci., 233*, 275–287.

Matschuk, M. and Larsen, N. B. (2013). “Injection molding of high aspect ratio sub-100 nm nanostructures.” *J. Micromech. Microeng. 23*, 025003.

Nath, A. K. (2014). “Laser Drilling of Metallic and Nonmetallic Substrates.” *Comprehensive Materials Processing* 9.

Noh, J., et al. (2010). “Fabrication of hierarchically micro- and nano-structured mold surfaces using laser ablation for mass production of superhydrophobic surfaces.” *Jpn. J. Appl. Phys., 49*, 106502.

Nolte, S., et al. (1997). “Ablation of metals by ultrashort laser pulses.” *J. Opt. Soc. Am. B Opt. Phys. 14*, 2716–2722.

Nosonovsky, M. and Bhushan, B. (2009). "Superhydrophobic surfaces and emerging applications: Non-adhesion, energy, green engineering." *Current Opinion in Colloid & Interface Science 14(4)*, 270-280.

Orazi, L., et al. (2020). "Generation and Characterization of Laser Induced Periodic Surface Structures on Plastic Injection Molds." *Lasers in Manufacturing and Materials Processing 7(2)*, 207-221.

Patankar, N. A. (2004). “Transition between Superhydrophobic States on Rough Surfaces.” *Langmuir 20*, 7097-7102.

Piccolo, L., et al. (2020). "Functionalization of Plastic Parts by Replication of Variable Pitch Laser-Induced Periodic Surface Structures." *Micromachines (Basel) 11*(4).

Rasilainen, T., et al. (2010). "Modification of polypropylene surfaces with micropits and hierarchical micropits/nanodepressions." *Surface Science 604(21-22)*, 2036-2042.

Romano, J.-M., et al. (2019). "Mechanical durability of hydrophobic surfaces fabricated by injection moulding of laser-induced textures." *Applied Surface Science 476*, 850-860.

Rosenfeld, A., et al. (1999). “Ultrashort-laser-pulse damage threshold of transparent materials and the role of incubation.” *Appl. Phys. A, 69*, S373–S376.

Saarikoski, I., et al. (2012). "Superhydrophobic elastomer surfaces with nanostructured micronails." *Surface Science 606(1-2)*, 91-98.

Sarkar, A. and Kietzig, A.-M. (2013). "General equation of wettability: A tool to calculate the contact angle for a rough surface." *Chemical Physics Letters 574*, 106-111.

Semaltianos, N.G., et al. (2009). “Femtosecond laser ablation characteristics of nickel-based superalloy C263.” *Appl. Phys. A, 94*, 999–1009.

Semuels, A. (2019). “Is This the End of Recycling?”. *The Atlantic*. Available at: https://www.theatlantic.com/technology/archive/2019/03/china-has-stopped-accepting-our-trash/584131/

Shafrin, E. G. and Zisman, W. A. (1960). "Constitutive Relations in the Wetting of Low Energy Surfaces and the Theory of the Retraction Method of Preparing Monolayers." *Journal of Physical Chemistry 64(5)*: 519-524.

Stormonth-Darling, J. M. et al. (2014). “Injection moulding of ultra high aspect ratio nanostructures using coated polymer tooling.” *J. Micromech. Microeng. 24*, 075019.

Stormonth-Darling, J. M., et al. (2016). “Injection Molding Micro- and Nanostructures in Thermoplastic Elastomers.” *Macromol. Mater. Eng. 301*, 964-971.

Stuart, B.C., et al. (1996). “Optical ablation by high-power short-pulse lasers.” *J. Opt. Soc. Am. B Opt. Phys., 13*, 459–468.

Sugioka, K., and Cheng, Y. (2014). “Femtosecond Laser 3D Micromachining for Microfluidic and Optofluidic Applications.” New York, Springer.

Toosi, S., et al. (2016). “Microfabrication of polymeric surfaces with Extreme Wettability using Hot Embossing.” *Applied Surface Science 378*, 426-434.

Trageser, C. (2019). “Why Are There So Many Broken Trash Bins In San Diego?”. *KBPS*. Available at: https://www.kpbs.org/news/2019/oct/14/why-broken-trash-bins-san-diego/

Vepsäläinen, L., et al. (2012). "Frequency analysis of micropillar structured surfaces: A characterization and design tool for surface texturing." *Applied Surface Science 263*, 523-531.

Von der Linde, D., et al. (1997). “Laser-solid interaction in the femtosecond time regime.” *Appl. Surf. Sci., 109*, 1–10.

Vorobyev, A. Y., and Guo, C. (2013). "Direct femtosecond laser surface nano/microstructuring and its applications". *Laser & Photonics Reviews, 407*(3), 385–407.

Wellershoff, S.S., et al. (1999). “The role of electron-phonon coupling in femtosecond laser damage of metals.” *Appl. Phys. A, 69*, S99–S107.

Weng, C., et al. (2018). "Fabrication of hierarchical polymer surfaces with superhydrophobicity by injection molding from nature and function-oriented design." *Applied Surface Science 436*, 224-233.

Wenzel, R. N. (1936). “Resistance of solid surfaces to wetting by water”. *Industrial & Engineering Chemistry, 28* (8), 988-994.

Will, M., et al. (2002). “Optical properties of waveguides fabricated in fused silica by femtosecond laser pulses.” *Appl. Opt., 41*, 4360–4364.

Wood, M. J., et al. (2021). “The Tuning of LIPSS Wettability during Laser Machining and through Post-Processing.” *Nanomaterials 11(4)*, 973.

Wu, P. H., et al. (2011). "Fabrication of large-area hydrophobic surfaces with femtosecond-laser-structured molds." *Journal of Micromechanics and Microengineering 21*(11).

Wu, S. (1969). “Surface and Interfacial Tensions of Polymer Melts.” *Journal of Colloid and Interface Science 31-2*.

Xie, H., et al. (2019). "Bioinspired preparation of regular dual-level micropillars on polypropylene surfaces with robust hydrophobicity inspired by green bristlegrass leaves." *Polymers for Advanced Technologies 31(3)*, 492-500.

Yao, T.-F., et al. (2011). “Fabrication of anti-reflective structures using hot embossing with a stainless steel template irradiated by femtosecond laser.” *Microelectronic Engineering 88*, 2908-2912.

Young, T. (1805). "An Essay on the Cohesion of Fluids." *Philosophical Transactions of the Royal Society of London 95(1805)*, 65-87.

Zhang, D., et al. (2010). “Wetting characteristics on hierarchical structures patterned by a femtosecond laser.” *J. Micromech. Microeng. 20*, 075029.

Zheng, Q.-S., et al. (2005). “Effect of Hydraulic Pressure on the Stability and Transition of Wetting Modes of Superhydrophobic Surfaces.” *Langmuir 21*, 12207-12212.

Zhou, M., et al. (2018). "Fabrication of high aspect ratio nanopillars and micro/nano combined structures with hydrophobic surface characteristics by injection molding." *Applied Surface Science 427*, 854-860.

13 APPENDIX

Below are the codes programmed on Python version 3.7.9 for the thermodynamic optimization of square holes (H_2O on PE) with square pillars (PE on SS), followed by hexagonal holes (H_2O on PE) with hexagonal pillars (PE on SS). It is important to notice that all equations used for PE on SS have the variables *a* and *b* inverted. That is for the *a* and *b* resulted values follow the same nomenclature as presented in Figure 35 for pillars and holes. In other words, if the resulting *a* = 60 μm for example, that means that for holes (H_2O on PE), *a* is the spacing between features on PE, and for pillars (PE on SS), *a* is the width of the pillar geometries on SS.

Square Holes (H_2O on PE) with Square Pillars (PE on SS) - Thermodynamic Optimization Code

```
# -*- coding: utf-8 -*-
"""
Created on Mon Dec 16 17:55:01 2019

@author: mumic
"""

from __future__ import division
import math

cos = math.cos
acos = math.acos
pi = math.pi
rad = math.radians

# Sq.Holes (H2O on PE) with Sq.Pillars (PE on SS) - Thermodynamic Optimization

#Lists (H2O on PE)
SolutionSet=[]
Solution=[]
SolutionSet1=[]
CurrentSolution=[]
a_list=[]
b_list=[]
theta_c_list=[]
theta_c_list1=[]
G_list=[]
G_list1=[]
```

```
pc_list=[]
pc_list1=[]

#Lists (PE on SS)
theta_c1_list=[]
theta_c1_list1=[]
G1_list=[]
G1_list1=[]
pc1_list=[]
pc1_list1=[]

# (H2O on PE) 0.0728 N/m at 20 ºC for gama_la and 95º (experimental value for HDPE-
      2074) for theta_y are the fixed numbers for water on PE. See Luna et al. (2013) for
      more details on the water contact angle on high density polyethylene (HDPE).
gama_la=0.0728 #N/m
theta_y=95.*pi/180.

#(PE on SS) 0.02373 N/m for gama_la at 230 ºC (yla(PE)= 35.7-0.057(t-20)) and 92º
      (experimental value for HDPE-2074) for theta_y are the fixed numbers for PE on SS.
gama_la1=0.02373 #N/m
theta_y1=92.*pi/180.

for a in range(6,155,5): #a is the spacing between holes (um) - (H2O on PE)
   a_list.append(a)
   for b in range(50,155,5): #b is the width of the holes (um)- (H2O on PE)
      b_list.append(b)
      for c in range(1,275,5): #c is the depth of the holes (um)- (H2O on PE)

         theta_c=acos(((a*(2.*b+a))/((b+a)**2.))*(cos(theta_y)+1.)-1.) #(H2O on PE)
         theta_c_list1.append((theta_c*180.)/pi)

         theta_c1=acos(((b**2.)/((b+a)**2.))*(cos(theta_y1)+1.)-1.)  #(PE on SS)
         theta_c1_list1.append((theta_c1*180.)/pi)

         try:
            # Square Holes (H2O on PE) equations
            wenz=((((4.*b*c)/((b+a)**2.))+1.)*cos(theta_y))
            if wenz>=1.: #these if statements limit the Wenzel contact angle from 0º to 178º.
               wenz=1.
               theta_w=acos(wenz)
            elif wenz<=-1.:
               wenz=-0.999
               theta_w=acos(wenz)
            else:
               theta_w=acos(wenz)

            Gcassie=gama_la*(10**(-6))*(((2.*((b+a)**2.))/(1.+cos(theta_c)))+(b**2.)-
         ((2.*b*a)+(a**2.))*cos(theta_y))
            Gwenzel=gama_la*(10**(-6))*(((2.*((b+a)**2.))/(1.+cos(theta_w)))-
         (((b+a)**2.)+4.*b*c)*cos(theta_y))
```

```
            G=Gwenzel-Gcassie #N.um or uJ
            G_list1.append(G)
            f = (a*(2*b+a))/((b+a)**2)
            lambd = (a*(2*b+a))/((4*a)+(4*b))
            pc = -(gama_la)*f*cos(theta_y)/((1-f)*(lambd*10**(-6))) #Pa
            pc_list1.append(pc)


            # Square Pillars (PE on SS) equations
            wenz1=((((4.*b*c)/((b+a)**2.))+1.)*cos(theta_y1))
            if wenz1>=1.: #these if statements limits the Wenzel contact angle from 0º to 178º.
               wenz1=1.
               theta_w1=acos(wenz1)
            elif wenz1<=-1.:
               wenz1=-0.999
               theta_w1=acos(wenz1)
            else:
               theta_w1=acos(wenz1)

            Gcassie1=gama_la1*(10**(-
        6))*((2.*b*a)+(a**2.)+((2.*((b+a)**2.))/(1.+cos(theta_c1)))-(b**2.)*cos(theta_y1))
            Gwenzel1=gama_la1*(10**(-6))*(((2.*((b+a)**2.))/(1.+cos(theta_w1)))-
        (((b+a)**2.)+4.*b*c)*cos(theta_y1))
            G1=Gwenzel1-Gcassie1 #N.um or uJ
            G1_list1.append(G1)
            f1 = ((b**2)/((b+a)**2))
            lambd1 = (b/4)
            pc1 = -(gama_la1)*f1*cos(theta_y1)/((1-f1)*(lambd1*10**(-6))) #Pa
            pc1_list1.append(pc1)
            CurrentSolution=["(H2O on PE) a:",a," b:",b," c:",c,"
        theta_c:",round((theta_c*180/pi))," delta_Gmax:",round(G, 6)," Pc:",round(pc),"
        (PE on SS) delta_Gmax:",round(G1, 6)," Pc:",round(pc1)]
            SolutionSet.append(CurrentSolution)

            if (G>0 and c/a<=1.8 and theta_c*180/pi>100):
              Solution = ["(H2O on PE) a:",a," b:",b," c:",c,"
        theta_c:",round((theta_c*180/pi))," delta_Gmax:",round(G, 6)," Pc:",round(pc),"
        (PE on SS) delta_Gmax:",round(G1, 6)," Pc:",round(pc1)]
               SolutionSet1.append(Solution)
        except:
               G_list1.append(-9999999999999)

G_list.append(G_list1)
G_list1=[]
theta_c_list.append(theta_c_list1)
theta_c_list1=[]
pc_list.append(pc_list1)
pc_list1=[]
G1_list.append(G_list1)
G1_list1=[]
```

```
    theta_c1_list.append(theta_c1_list1)
    theta_c1_list1=[]
    pc1_list.append(pc1_list1)
    pc1_list1=[]

f=open('Sq.Holes (H2O on PE) with Sq.Pillars (PE on SS).txt','w')
for i in range (0,len(SolutionSet1)):
    f.write("   ".join(map(str, SolutionSet1[i])))
    f.write('\n')
f.close()
```

Hexagonal Holes (H_2O on PE) with Hexagonal Pillars (PE on SS) - Thermodynamic Optimization Code

```
# -*- coding: utf-8 -*-
"""
Created on Mon Dec 16 17:55:01 2019

@author: mumic
"""

from __future__ import division
import math

cos = math.cos
tan = math.tan
acos = math.acos
pi = math.pi
rad = math.radians
sqrt = math.sqrt

# Hex.Holes (H2O on PE) with Hex.Pillars (PE on SS) - Thermodynamic Optimization

#Lists (H2O on PE)
SolutionSet=[]
Solution=[]
SolutionSet1=[]
CurrentSolution=[]
a_list=[]
b_list=[]
theta_c_list=[]
theta_c_list1=[]
G_list=[]
G_list1=[]
pc_list=[]
pc_list1=[]
```

```
#Lists (PE on SS)
theta_c1_list=[]
theta_c1_list1=[]
G1_list=[]
G1_list1=[]
pc1_list=[]
pc1_list1=[]

# (H2O on PE) 0.0728 N/m at 20 ºC for gama_la and 95º (experimental value for HDPE-
      2074) for theta_y are the fixed numbers for water on PE. See Luna et al. (2013) for
      more details on the water contact angle on high density polyethylene (HDPE).
gama_la=0.0728 #N/m
theta_y=95.*pi/180.

#(PE on SS) 0.02373 N/m for gama_la at 230 ºC (yla(PE)= 35.7-0.057(t-20)) and 92º
      (experimental value for HDPE-2074) for theta_y are the fixed numbers for PE on SS.
gama_la1=0.02373 #N/m
theta_y1=92.*pi/180.

for a in range(6,155,5): #a is the spacing between holes (um) - (H2O on PE)
   a_list.append(a)
   for b in range(50,155,5): #b is the width of the holes (um) - (H2O on PE)
      b_list.append(b)
      for c in range(1,275,5): #c is the depth of the holes (um)- (H2O on PE)

         theta_c=acos(((((((sqrt(3))*((b+a)**2))/4)-
         ((3*(sqrt(3))*(b**2))/(4*((tan(rad(60)))**2))))/(((sqrt(3))*((b+a)**2))/4))*(cos(theta_
         y)+1))-1) #(H2O on PE)
         theta_c_list1.append((theta_c*180.)/pi)

         theta_c1=acos((((3*b**2)/(((tan(rad(60)))**2)*((b+a)**2)))*(cos(theta_y1)+1))-1)
         #(PE on SS)
         theta_c1_list1.append((theta_c1*180.)/pi)

         try:
            # Hexagon Holes (H2O on PE) equations

         wenz=((((((sqrt(3))*((b+a)**2))/4)+((3*b*c)/(tan(rad(60)))))/(((sqrt(3))*((b+a)**2))/4
         ))*(cos(theta_y)))
            if wenz>=1.: #these if statements limit the Wenzel contact angle from 0º to 178º.
               wenz=1.
               theta_w=acos(wenz)
            elif wenz<=-1.:
               wenz=-0.999
               theta_w=acos(wenz)
            else:
               theta_w=acos(wenz)

            Gcassie=gama_la*(10**(-
         6))*(((((b+a)**2)*(sqrt(3)))/(2*(1+cos(theta_c))))+((3*(sqrt(3))*(b**2))/(4*((tan(rad(
```

```
60)))**2)))-((((((b+a)**2)*(sqrt(3)))/4)-
((3*(sqrt(3))*(b**2))/(4*((tan(rad(60)))**2))))*(cos(theta_y))))
   Gwenzel=gama_la*(10**(-6))*(((((b+a)**2)*(sqrt(3)))/(2*(1+cos(theta_w))))-
(((((sqrt(3))*((b+a)**2))/4)+((3*b*c)/(tan(rad(60)))))*(cos(theta_y))))
   G=Gwenzel-Gcassie #N.um or uJ
   G_list1.append(G)
   f                    =                    (((((sqrt(3))*((b+a)**2))/4)-
((3*(sqrt(3))*(b**2))/(4*((tan(rad(60)))**2))))/(((sqrt(3))*((b+a)**2))/4))
   lambd                =                    (((((sqrt(3))*((b+a)**2))/4)-
((3*(sqrt(3))*(b**2))/(4*((tan(rad(60)))**2))))/(((3*b)/(tan(rad(60))))+(3*a)))
   pc = -(gama_la)*f*cos(theta_y)/((1-f)*(lambd*10**(-6))) #Pa
   pc_list1.append(pc)


   # Hexagon Pillars (PE on SS) equations

wenz1=((((((sqrt(3))*((b+a)**2))/4)+((3*b*c)/(tan(rad(60)))))/(((sqrt(3))*((b+a)**2))/
4))*(cos(theta_y1)))
   if wenz1>=1.: #these if statements limits the Wenzel contact angle from 0º to 178º.
      wenz1=1.
      theta_w1=acos(wenz1)
   elif wenz1<=-1.:
      wenz1=-0.999
      theta_w1=acos(wenz1)
   else:
      theta_w1=acos(wenz1)

   Gcassie1=gama_la1*(10**(-
6))*(((((b+a)**2)*sqrt(3))/(2*(1+cos(theta_c1))))+((((b+a)**2)*sqrt(3))/4)-
((3*(sqrt(3))*(b**2))/(4*((tan(rad(60)))**2)))-
(((3*(sqrt(3))*(b**2))/(4*((tan(rad(60)))**2)))*(cos(theta_y1))))
   Gwenzel1=gama_la1*(10**(-6))*(((((b+a)**2)*sqrt(3))/(2*(1+cos(theta_w1))))-
(((((sqrt(3))*((b+a)**2))/4)+((3*b*c)/(tan(rad(60)))))*(cos(theta_y1))))
   G1=Gwenzel1-Gcassie1
   G1_list1.append(G1)
   f1 = ((3*b**2)/(((tan(rad(60)))**2)*((b+a)**2)))
   lambd1 = (((sqrt(3))*(b))/(4*(tan(rad(60)))))
   pc1 = -(gama_la1)*f1*cos(theta_y1)/((1-f1)*(lambd1*10**(-6))) #Pa
   pc1_list1.append(pc1)
   CurrentSolution=["(H2O on PE) a:",a," b:",b," c:",c,"
theta_c:",round((theta_c*180/pi))," delta_Gmax:",round(G, 6)," Pc:",round(pc),"
(PE on SS) delta_Gmax:",round(G1, 6)," Pc:",round(pc1)]
   SolutionSet.append(CurrentSolution)

   if (G>0 and c/a<=1.8 and theta_c*180/pi>100):
     Solution = ["(H2O on PE) a:",a," b:",b," c:",c,"
theta_c:",round((theta_c*180/pi))," delta_Gmax:",round(G, 6)," Pc:",round(pc),"
(PE on SS) delta_Gmax:",round(G1, 6)," Pc:",round(pc1)]
     SolutionSet1.append(Solution)
except:
```

```
                G_list1.append(-9999999999999)

    G_list.append(G_list1)
    G_list1=[]
    theta_c_list.append(theta_c_list1)
    theta_c_list1=[]
    pc_list.append(pc_list1)
    pc_list1=[]
    G1_list.append(G_list1)
    G1_list1=[]
    theta_c1_list.append(theta_c1_list1)
    theta_c1_list1=[]
    pc1_list.append(pc1_list1)
    pc1_list1=[]

f=open('Hex.Holes (H2O on PE) with Hex.Pillars (PE on SS).txt','w')
for i in range (0,len(SolutionSet1)):
    f.write("   ".join(map(str, SolutionSet1[i])))
    f.write('\n')
f.close()
```